Cranfield University

School Of Engineering

Ph. D. Thesis

Georgios Sarantavgas, B.Eng. (Hons), M.Sc., MIET

An investigation of a fibre optic Fizeau interferometer configuration and coherent fibre optic imaging bundles for Optical Coherence Tomography

This thesis is submitted in partial fulfilment of the requirements for the degree of Doctor of Philosophy.

Cranfield University

School Of Engineering

Department of Process and Systems Engineering

Centre for Photonics and Optical Engineering

Ph. D. Thesis

Academic year: 2007-2008

Georgios Sarantavgas

An investigation of a fibre optic Fizeau interferometer configuration and coherent fibre optic imaging bundles for Optical Coherence Tomography

Supervisor: Prof. Ralph P. Tatam

This thesis is submitted in partial fulfilment of the requirements for the degree of Doctor of Philosophy.

Abstract

Currently several medical imaging techniques are in operation in clinical environments that help the doctors to diagnose diseases before proceeding to treatment. This research investigated and implemented configurations for a medical imaging technique called Optical Coherence Tomography (OCT).

The Michelson interferometer has been the principal configuration for OCT systems. For endoscopic OCT applications though such a configuration is susceptible to polarisation induced signal fading due to environmental changes within the sample arm, like fibre bending and temperature fluctuations. The development and testing of a Fizeau interferometer based OCT system demonstrate the elimination of this polarisation induced signal fading as the sample and reference arm of the interferometer experience the same environmental changes. The Fizeau interferometer is formed between the end of the fibre and the sample itself. A secondary processing interferometer is used in this configuration, to compensate the path difference inherent to the Fizeau configuration. Longitudinal resolution is about 19 μm in air, and lateral resolution about 23 μm. A signal-to-noise ratio of about 80 dB was achieved with this system and several sets of image data were collected from laboratory and biological samples.

An OCT system based on a Fizeau interferometer incorporating a coherent fibre imaging bundle was also investigated. Fibres in the bundle are accessed sequentially by a beam focused onto the input face of the bundle, allowing 2D information to be acquired using point detection. Incorporating a fibre optic imaging bundle in Fizeau based interferometer OCT allows mechanical scanning parts to be removed from the sample arm, resulting in a passive probe. Such a configuration can form a compact, robust and "downlead insensitive" OCT system and is a strong candidate for in vivo applications. The performance of leached and wound coherent fibre optic bundles was accessed and an analysis is presented. The longitudinal resolution of the system developed was about 10 μm in air, and lateral resolution about 9 μm. This thesis demonstrates several sets of image data that were collected from various samples using a Fizeau interferometer based OCT incorporating coherent imaging bundles. 2D

image data captured by such a configuration are presented and reported for the first time in this thesis.

Acknowledgments

I am grateful to my supervisor, Prof. Ralph Tatam, whose intellectual assistance and guidance was highly appreciated throughout the course of this work.

I would also like to express my gratitude to Dr. Helen Ford for all the support during my Ph.D. years.

I am especially thankful to Dr. Edmond Chehura for sharing all his valuable experiences with me.

I would also like to thank my brother Stratos and my parents Fotios and Maria. Thank you for believing in me.

Last but not least, I am mostly grateful to my wife, Ioanna Armouti, which without her love, tolerance, encouragement and support, I do not really know how any of this would have been possible.

I dedicate this thesis to my child Maria (expected to be born in October 2008)

Σα βγεις στον πηγαιμό για την Ιθάκη,
να εύχεσαι νάναι μακρύς ο δρόμος,
γεμάτος περιπέτειες, γεμάτος γνώσεις.
…
Πολλά τα καλοκαιρινά πρωϊά να είναι
που με τι ευχαρίστησι, με τι χαρά
θα μπαίνεις σε λιμένας πρωτοειδωμένους.
…
Πάντα στον νου σου νάχεις την Ιθάκη.
Το φθάσιμον εκεί είν' ο προορισμός σου.
Αλλά μη βιάζεις το ταξείδι διόλου.
Καλλίτερα χρόνια πολλά να διαρκέσει,
και γέρος πια ν' αράξεις στο νησί,
πλούσιος με όσα κέρδισες στον δρόμο…

Κωνσταντίνος Καβάφης
Ιθάκη [1911]

When you set out on your journey to Ithaca,
pray that the road is long,
full of adventures, full of knowledge.
…
That the summer mornings are many, when,
with such pleasure, with such joy
you will enter ports seen for the first time.
…
Always keep Ithaca in your mind.
To arrive there is your ultimate goal.
But do not hurry the voyage at all.
It is better to let it last for many years,
and to anchor at the island when you are old,
rich with all you have gained on the way…

Constantinos Kavafis
Ithaca [1911]
(unknown translator)

Abbreviations

CT	Computed Tomography
MRI	Magnetic Resonance Imaging
SPECT	Single Photon Emission Tomography
PET	Positron Emission Tomography
OCT	Optical Coherence Tomography
PS-OCT	Polarisation Sensitive Optical Coherence Tomography
SD-OCT	Spectral Domain Optical Coherence Tomography
SS-OCT	Swept Source Optical Coherence Tomography
OTDR	Optical Time Domain Reflectometry
LCI	Low Coherence Interferometry
OLCR	Optical Low Coherence Reflectometry
SNR	Signal to Noise Ratio
MI	Michelson Interferometer
MZI	Mach Zehnder Inteferometer
SLD	Super Luminescent Diode
OPD	Optical Path Difference
OT	Optical Thickness
BS	Beam Splitter
PBS	Polarising Beam Splitter
MO	Microscope objective
CCD	Charged Coupled Device
GI	Gastrointestinal
IR	Infrared

NIR	Near Infrared
NA	Numerical Aperture
PZT	Lead Zirconate Tinanate (Piezoelectric)
RI	Refractive index
QWP	Quarter Wave Plate

Table of contents

Chapter 1

INTRODUCTION

1. Introduction

Medical imaging is vital for the diagnosis of numerous diseases and illnesses, as it provides the means to extract anatomical and functional information about a patient in order to proceed to corrective treatment. Optical Coherence Tomography (OCT) is a relatively new non-invasive medical imaging technique whose foundations rely on low-coherence interferometry. OCT applications extend, but are not limited to, medical and biological purposes [1], material sciences [2] and arts [3]. OCT imaging systems were developed in response to the demand to explore microstructures within turbid biological media using non-ionising radiation which is clinically safe. OCT systems currently researched are regarded as the 6^{th} generation medical imaging tools with respect to the other five medical imaging modalities of PET (Positron Emission Tomography), MRI (Magnetic Resonance Imaging), CT (Computed Tomography), Ultrasound and X-ray. OCT can generate ultra high resolution tomographic images in the range of 1 to 30μm [4, 5], with a limited imaging depth of 1-2mm [6]. Presently most of the techniques shown in figure 1.1 are deployed in clinical environments.

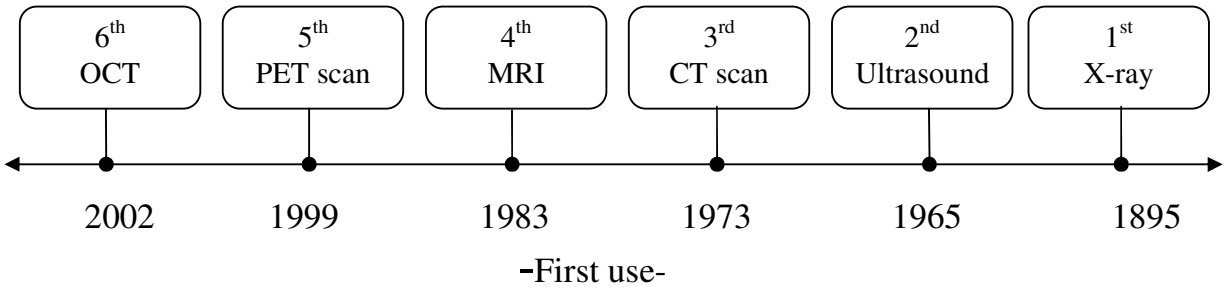

Figure 1.1: Six generations of medical imaging tools

However techniques 1 to 5 have a limited imaging resolution from 100μm to 1mm that is not sufficient to distinguish microstructures like cells of biological samples [7]. The ability to get high resolution images down to the scale of cells will assist in spotting any abnormalities such as early signs of numerous carcinomas. Currently to obtain such high resolution images giving the capability to the doctor to detect such abnormalities, a biopsy is performed involving the surgical excision of the tissue for a microscopic histological examination [8]. This is an expensive and a time consuming process. Through this method, a considerable number of cases are often misdiagnosed and left untreated.

Therefore, a more consistent method with higher resolution, capable of identifying tissue abnormalities in their early stages of development without surgical removal of tissue would be beneficial.

1.1 Optical Coherence Tomography (OCT)

Tomography usually refers to medical imaging techniques that produce images of organs or structures within the human body aiming to uncover and locate malformation of the tissue. Optical Coherence Tomography (OCT) is a technique for obtaining subsurface images of translucent or opaque samples at 1-2mm depth with micrometer scale axial and lateral resolution. It's a non-invasive interferometric

technique and it has attracted a great deal of interest in the medical community due to its capability of providing images of tissue morphology at far higher resolution (near microscopic resolution) when compared to the other imaging modalities. Imaging with OCT can be performed ex-vivo although another great advantage is its in-vivo deployment capability [9].

It can be said that OCT is somewhat analogous to ultrasound and it is also referred to as 'optical ultrasound' [10] except that it uses light instead of sound. OCT constructs cross-sectional images of internal microstructures in materials and biological systems by measuring the echo time delay and intensity of a backscattered/back reflected light from the sample. However, optical time delays are extremely short and thus direct electronic detection is not possible. Hence OCT measurements of echo time delay are based on correlation techniques that compare the backscattered/backreflected light signal to the reference light travelling a known path-length. OCT uses an optical interferometer to process the signal and ultrasound uses an electronic circuit. Figure 1.2 depicts an image of a coronary artery where the high superiority in resolution of OCT is evident by the sharp delineation of arterial layers [11] when compared to an ultrasound image.

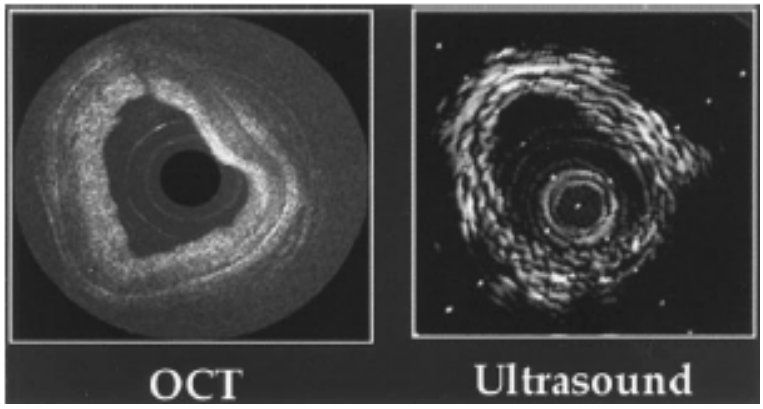

Figure 1.2 : Comparison of OCT and high frequency Ultrasonic (30 MHz)[11].

In an OCT instrument an optical beam illuminates the sample and light is reflected from the sub-surface layers as the beam penetrates, due to refractive index differences between them. Although most of the light is scattered on its way back to the surface a small portion is not and that portion is detected and used in OCT. The

scattered/reflected light has the property of being coherent with the reference beam so it can be detected in the interferometer based OCT instrument.

The detector is used to separate the usable coherent light from the useless incoherent scattered light. It also supplies the depth and intensity variations information from a sub-surface feature enabling an image to be built up. An OCT image is a 2D or a 3D data set that represents differences in optical backscattering/backreflection in a cross-sectional plane or volume. The limited imaging depth with this technique is due to the fact that at greater depths the proportion of light that escapes without scattering is relatively small, due to reasons that will be addressed in a later chapter. Although the penetration depth is relatively low the information that OCT can generate is invaluable as the majority of cancer cases begin in the surface or epithelial tissues of the body [12, 13]. The majority of optical sources that are deployed in an OCT system operate in infra-red region (800nm-1550nm) with eye safe output power and a bandwidth ranging from several of tens of nanometres to hundreds of nanometres.

Most techniques used at present for the implementation of an OCT system are based upon the Michelson interferometer configuration with the sample located in one arm and a reference mirror [14] in the other as shown in figure 1.3.

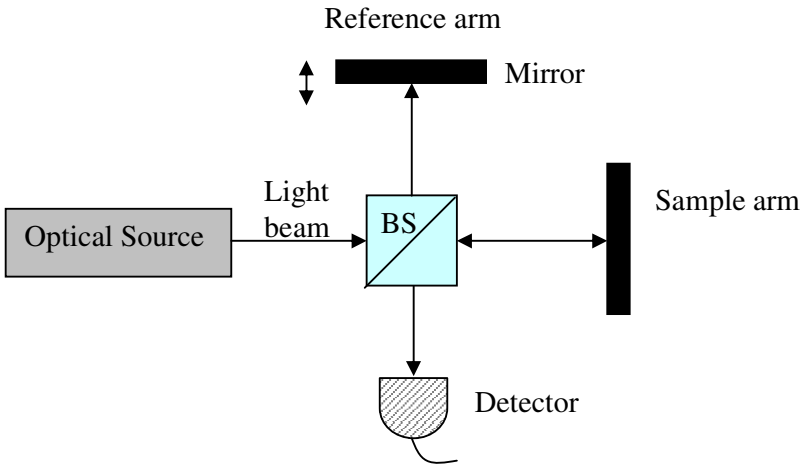

Figure 1.3 : Bulk-optic Michelson interferometer, BS: beamsplitter

At the sample arm a system of lenses focuses the light to a few microns (transverse resolution) onto the sample and the backscattered/backreflected light from the sample couples back to the same arm and mixes at the detector with the reference signal beam. If the path lengths travelled by the two beams are matched within the coherence length of the source (Δ z =1-30μm), interference fringes are formed as shown in figure 1.4 if a mirror is used as a sample.

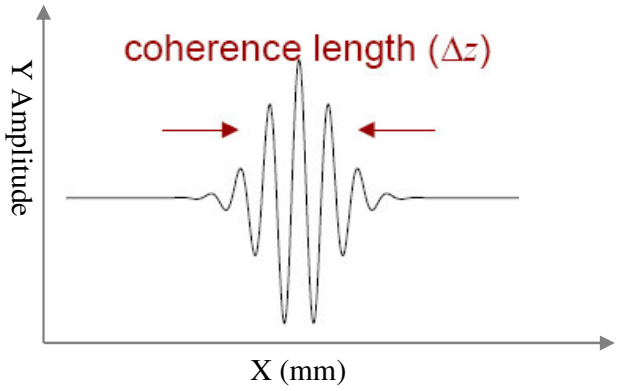

Figure 1.4: Interference fringe pattern

If a multilayer sample is to be used the boundaries inside the sample are detected as burst of fringes corresponding to various depths. The bandwidth of the source has to be as large as possible since the depth resolution is determined by the coherence length, which is inversely related to the source spectral width.

However the limitation of a bulk-optic OCT system based on Michelson configuration is that it is incapable of deployment in an endoscopic operation. Thus replacement of the bulk optic components with their fibre equivalents leads to a more compact and robust instrument capable of in-vivo imaging.

1.2 Motivation

The drawback of a fibre Michelson based OCT system as shown in figure 1.5 is that it is susceptible to signal fading. Signal fading or, at times, complete signal loss, arises due to the fact that the states of polarisation of light propagating in standard optical fibre is not maintained [15].

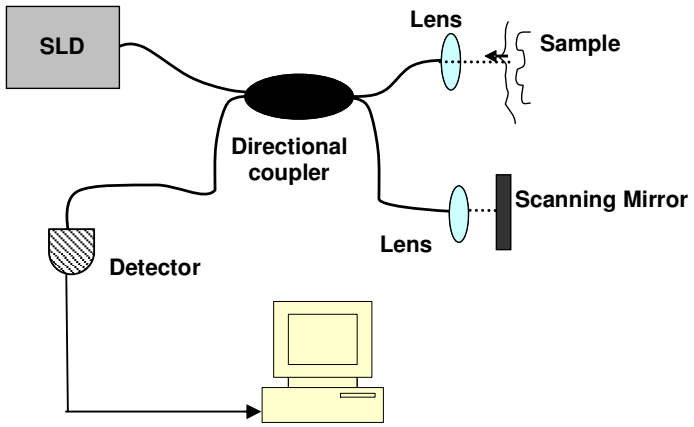

Figure 1.5: Fibre based Michelson interferometer.

Since the sample and reference beams are transmitted in separate fibres, their states of polarisation will, in general, be completely uncorrelated, resulting in a lower-than-optimum signal visibility. This phenomenon will be particularly noticeable in in-vivo applications since bending of fibres induce birefringence hence the polarisation state will change and temperature fluctuations causing phase drifting are unavoidable. This research will propose an alternative configuration providing a solution to this issue,

Furthermore current OCT systems have the capability of constructing 2D images by delivering a focused beam of light a few microns in diameter to the sample and acquiring multiple sets of data as this beam is scanned across the area of interest [16]. This is frequently achieved by using a small moving mirror to scan the beam rapidly across the sample. However for in-vivo deployment it's understood that the

physical dimension of the probe is the limiting factor thus everything must be miniaturised and fitted into an endoscope.

Although such configurations have been demonstrated with success they are quite complex and challenging to implement (particularly the precise alignment of components). One more issue with such configurations is that they can also limit the transverse resolution of an OCT system because the size and the NA of the lenses and mirrors are restricted by the endoscope size.

Therefore the motive for this research is to address these two existing problems by considering a common path Fizeau based OCT for environmental stability and the use of coherent fibre optic imaging bundles for 2D or 3D imaging forming a compact and robust endoscope (i.e probe) without any moving parts at its tip.

Figure 1.6 below depicts a Fizeau interferometer configuration with a balancing processing Michelson interferometer. The Fizeau interferometer is formed between the end tip of the fibre and the backreflected/backscattered light from the sample itself. A Fresnel reflection occurs at the fibre tip and the light is backreflected into the fibre to form the reference channel. The sample channel is formed by the light that backreflected/ backscattered from the sample itself. Both signals from the reference channel and the sample channel will travel down the same fibre. Since there is an apparent path length mismatch an additional processing interferometer is to be used.

A coherent fibre optic imaging bundle consists of many individual fibres. The incorporation of an imaging bundle in such a configuration will allow 2D images to be formed by scanning a focussed beam at the input end of the bundle. Each fibre or areas of fibres are to be addressed sequentially effectively treating the bundle as a multiplexing element. Such a system will remove any scanning mechanisms from the probe tip as scanning is achieved at the input end of the bundle. For illustration purposes a schematic of such a bundle is shown in figure 1.7.

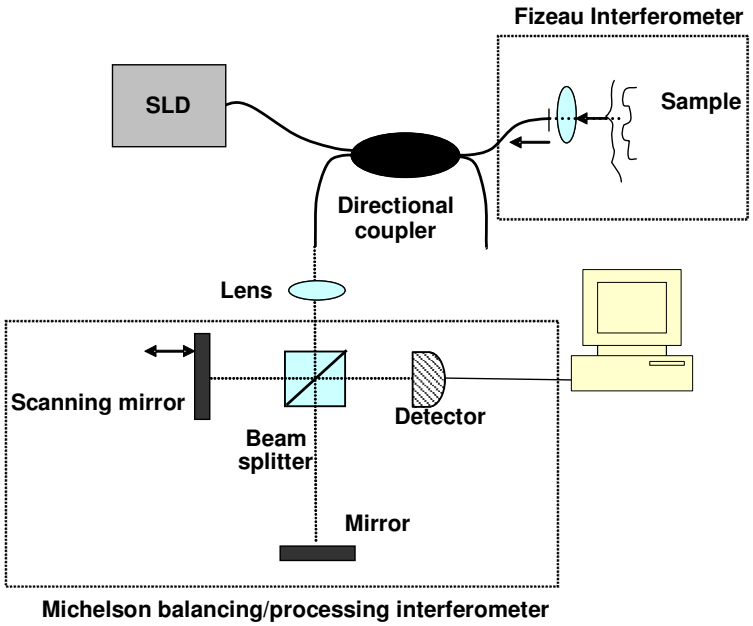

Figure 1.6: Fizeau interferometer with Michelson balancing/processing interferometer, SLD:Superluminescent diode

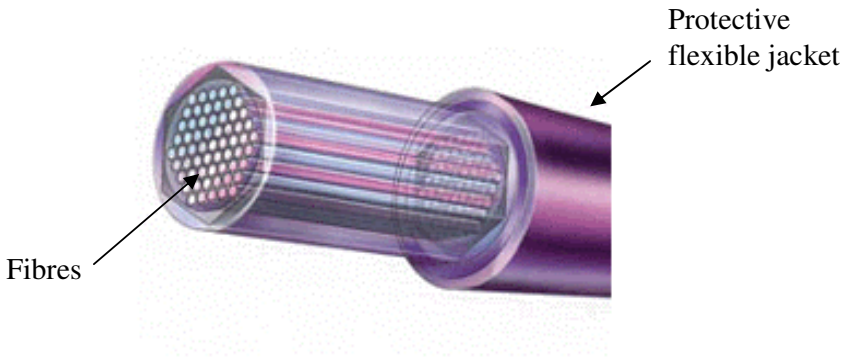

Figure 1.7: Coherent fibre optic imaging bundle [17]

The aims of this research include:

1) the investigation, detailed analysis and development of hardware and software to construct a time domain Fizeau based OCT system. Experimental analysis and verification of the Signal to Noise Ratio for the system constructed. Reporting measured refractive index profile data of laboratory and biological samples.

2) theoretical and experimental review of coherent fibre optic imaging bundles. Procedures and considerations for the incorporation of such bundles in a Fizeau interferometer based OCT system. Reporting refractive index profiles for laboratory samples and obtain 2D images.

1.3 Organisation of thesis

This thesis is to be organised as follows:

- **Chapter 1:** Introduces OCT as a medical imaging technique and presents the aims of this research.
- **Chapter 2:** Presents other medical imaging techniques and provides a comparison with OCT.
- **Chapter 3:** OCT Theory
- **Chapter 4:** Historical review of OCT applications.
- **Chapter 5:** Review of OCT instrumentation
- **Chapter 6:** Describes the implementation procedures and the apparatus used to construct a Fizeau based OCT system. It also demonstrates several experimental data and provides an in depth analysis of the system.

- **Chapter7:** Outlines the characteristics of fibre optic coherent imaging bundles as measured experimentally. States the implementation procedures for incorporating such bundles in an OCT system. The first ever reported results using such configuration are documented in this chapter followed by an analysis.

- **Chapter 8:** Presents conclusions and an outline of potential future improvements.

References

1. W. Drexler, H. Sattman, B. Hermann, T. Ko, M.Stur, A. Unterhuber, C. Scholda, O. Findl, M. Wirititisch, J.G Fujimoto, A.F. Frecher, *Enhanced visualisation of macular pathology with the use of ultrahigh-resolution OCT,* Arch. Opthalmology, 121, 2003, pp695-706

2. M. Bashkansky, M. Duncan, J. D.Reintjes, *Rapid, high-resolution optical coherence tomography (OCT) for defect detection in materials* Lasers and Electro-Optics, Volume 11, Issue , 18-23,1997,pp328 – 329

3. P. Targowski, Rouba, B. Góra, M. Tymińska-Widmer, L. Marczak, J Kowalczyk, *Optical coherence tomography in art diagnostics and restoration,* Applied Physics A, Vol. 92, Issue 1, 2008 , pp1-9

4. W. Drexler, U. Morgner, F. X. Kärtner, C. Pitris, S. A. Boppart, X. D. Li, E. P. Ippen, and J. G. Fujimoto. *In vivo ultrahigh-resolution optical coherence tomography*, Optics Letters, Vol. 24, Issue 17, pp1221-1223

5. X. Clivaz, F.Marquis-Weible, R.P. Salathe, *Optical low coherence reflectometry with 1.9μm spatial resolution*, Electronics Letters1992, Vol. 28, Issue16, pp1553-1555

6. B. W. Colston Jr., M. J. Everett, L. B. Da Silva, *Imaging of hard- and soft-tissue structure in the oral cavity by optical coherence tomography*, Applied Optics, Vol 37, 1998,pp3582-3585

7. P. J. Douglas, Picturing people: non-intrusive imaging, *Foresight Exploiting the Electromagnetic Spectrum State of the Science Review*, Cavendish Laboratory, Cambridge University, 2004.

8. B.J. Reid, D. S. Levine, G. Longton, P. L. Blount, P. S. Rabinovitch, *Predictors of progression to cancer in Barrett's esophagus: baseline histology and flow cytometry identify low- and high-risk patient subsets*, The American Journal of Gastroenterology,Vol.95 Issue 7, 2004,pp 1669 – 1676

9. T. Ko, C. Pitris, I Hartl, R. Ghanta, C. Chudoba, X.D. Li, W. Drexler, J.G. Fujimoto, M. Weinstein, *Ultrahigh resolution in vivo versus ex vivo OCT imaging and tissue preservation,* Lasers and Electro-Optics, 2001,pp252 – 253

10. J.G. Fujimoto. *Optical and acoustical imaging of biological media.* Compte Rendu De L'Académie Des Sciences, Vol. 2, 2001, pp1099-111.

11. M. E. Brezinski, G. J. Tearney, N. J.Weissman, S. A. Boppart, B. E. Bouma, M. R.Hee, A. E. Weyman, , E. A. Swanson, J. F.Southern, J. G Fujimoto, *Assessing atherosclerotic plaque morphology: Comparison of optical coherence tomography and high frequency intravascular ultrasound.* British Heart Journal,Vol.77, 1997,pp 397–404

12. J.A. Izatt, M.D. Kulkarni, Hsing-Wen Wang, K. Kobayashi, M.V. Sivak, *Optical coherence tomography and microscopy in gastrointestinal tissues* IEEE Journal of Selected Topics in Quantum Electronics, Vol.2, Issue 4,1996, pp1017-1028

13. R. Lazar, H. Brunner, and R. Steiner, *Optical coherence tomography (OCT) of human skin with a slow-scan CCD-camera,* Proc. SPIE 2925, 1996, pp143-151

14. M Hee, J. Izatt, E. Swanson, *Optical coherence tomography for ophthalmic imaging: new technique delivers micron-scale resolution*. IEEE in Medicine and Biology Vol.113, 1995, pp67-76.

15. A. D. Kersey, M. J. Marrone, M.A. Davis, *Polarisation-insensitive fibre optic Michelson interferometer*, Electronics Letters,Vol. 27, Issue 6, 1991, pp 518-520.

16. C. Salvini, D. Massi , A. Cappetti, M. Stante , P. Cappugi, P. Fabbri, P. Carli, *Application of optical coherence tomography in non-invasive characterization of skin vascular lesions,* Skin Research and Technology, Vol. 14, Issue 1, 2007,pp 89 – 92

17. http://www.schott.com [05/04/2005]

Chapter 2

MEDICAL IMAGING TECHNIQUES

2. Medical Imaging Techniques

Medical imaging can be defined as the acquisition and display, in a 2D or 3D format, of information obtained through the interaction of some form of radiation with a part of the human body. The term "imaging" is used, when the measurement resolution is high compared with the dimensions of the object(s) under investigation. Imaging systems can be categorised into two distinct areas [1]:

1. **Active** imaging systems, where some sort of radiation is used to interact with the sample under investigation and a detection mechanism is used.

2. **Passive** imaging systems, which depend on the emissions from the sample under investigation or of reflection or interaction with background sources of radiation.

In turn these two categories when photon emitting sources are used can be further subdivided into three more subcategories:

1. **Direct detection**-where the photon is directly guided to and absorbed by the detector.

2. **Time gated**- measures the time of flight of a photon either by adding a delay or by measuring different distances.

3. **Heterodyne**- where a source close to the frequency of the detected signal is mixed with the signal to provide amplification through interference and rejection of noise at frequencies outside signal bandwidth.

2.1 Medical imaging systems

Medical systems that use different techniques of imaging the body or parts of it are nowadays in use in clinical environments. Some of them are:

1. **X-rays**
2. **PET**-Positron Emission Tomography
3. **SPECT-** Single Photon Emission Computed Tomography
4. **MRI**-Magnetic Resonance Imaging
5. **CT**-Computed Tomography
6. **Ultrasound**
7. **OCT**-Optical Coherence Tomography

2.1.1 X-ray imaging

The X-ray technique that most people are familiar with, uses X-ray radiation field with a wavelength 10 to 0.01nm corresponding to frequencies 30-30.000 PHz[2].

X-rays (or Röntgen rays) were first discovered and published in 1895 by the German scientist *Wilhelm Conrad Röntgen* [3]. The first X-ray photograph that was taken of a hand is depicted in figure 2.1 which clearly reveals the bone structure and a wedding ring.

The working principle of X-rays relies on the acceleration of electrons to collide with a metal target which for medical application this is tungsten target. Upon collision the electrons decelerate and if the electron has sufficient energy has the ability to knock out an electron from the inner shell of the metal atom. Consequently electrons from higher levels of energy fill up the gap and X-ray photons are emitted.

Figure 2.1 : First X-ray image [3]

The detection of the emitted X-rays and reconstruction of the image from the internal organs and bones is done by a using a photographic plate or film. The photographic plates though are not sensitive to X-rays thus phosphorescent screens are placed in contact with the emulsion of the plate. When the phosphor screen is struck by the X-rays, it emits a visible light that exposes the plate or film. Eventually,

when part of the patient's body is to be X-rayed, it is placed between the X-ray emitting source and the detection plate.

The X-rays are blocked-absorbed by the dense tissues like bone structures and pass through soft tissues like muscle. The amount of absorption depends on the density of electrons in the tissue (bone-high density). Ultimately since less photons will reach the photographic detection plate when interacting with a bone structure the image will look brighter on that region and darker at softer tissue regions. Today's X-ray instruments have a limited spatial resolution in the range of 1mm [2].

X-ray imaging was primarily used to image the skeletal system of organisms but nevertheless is useful for detecting soft tissue diseases like pneumonia and lung cancer. On the other hand though, X-ray uses ionising radiation which is discovered to be a carcinogen factor. In January 2004 it was believed that 700 people in Britain develop cancer each year as a result from X-ray radiation in dentist surgeries and hospitals [4]. In March 2005 the US government added X-rays in their carcinogen list [5].

2.1.2 Positron Emission Tomography (P.E.T.)

PET is another medical imaging tool that produces three dimensional images by mapping functional processes of the human body. Before proceeding with the scan, an isotope (short lived radioactive tracer) is injected into the subject usually via blood circulation. Additionally the isotope is chemically integrated into a metabolically active molecule and a waiting period follows for the molecule to be concentrated in the area of interest. The isotopes that commonly used for this technique [6] include: 1) Fluorine-18 (half-life ~110min.), 2) Carbon-11 (~20 min.), 3) Oxygen-15 (~12min), 4) Nitrogen-23 (~9.9 min.). In turn the molecule that is typically used is the fluorodeoxyglucose ('a sugar') that has a waiting time of about 1 hour.

While scanning the subject, the isotope undergoes positron emission and it emits a positron (anti-particle of an electron). The positron then interacts and annihilates with an electron after a few millimetres of travel and this turns their mass

into energy and two photons are produced (gamma photons). The pair of gamma photons (511keV energy each) that are produced are emitted at ~180^{o} degrees to each other, thus someone can pinpoint their source along a straight line of coincidence.

To detect this pair of photons a scintillation material is used in the scanning device that creates a burst of light that is detected by a silicon avalanche photodiodes (Si PD) or a photomultiplier tubes. The spatial resolution of PET scanner is rather limited to 5mm. An example of such image being produced by a PET scanner is in figure 2.2. This image illustrates patterns in the brain that could aid in the diagnosis and treatment of Parkinson's disease. Additionally PET imaging is widely used in imaging of tumors and search for any metastases.

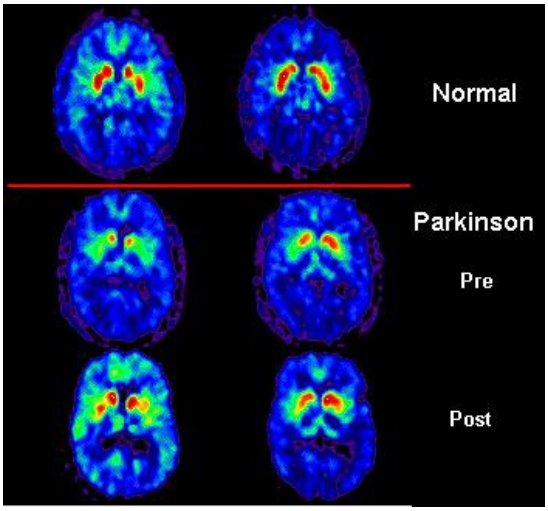

Figure 2.2: PET scan image [7]

2.1.3 Single Photon Emission Computed Tomography (S.P.E.C.T.)

SPECT is another nuclear medical tomographic imaging technique using gamma rays. In SPECT gamma cameras are used and a 2D image is produced by acquiring multiple images at different angles to the area of interest in the subject. An algorithm is applied to the multiple images to yield a 3D dataset. Before

scanning, a radioactive labelled pharmaceutical is injected into the subject. These usually are Technetium 99m (Tc^{99}) or Indium111.

After this procedure the labelled pharmaceutical starts to join to the organ or part of the body. This in turn is targeted for and emits gamma rays that are then detected by the gamma camera [6]. The multiple images are acquired by rotating the gamma camera(s) around the subject (360 degrees) usually in steps of 3-6 degrees. The time required to acquire one of the multiple images varies typically in the range of 15-20sec. Hence depending on the area of interest to be scanned total time varies accordingly. For a whole body the scan time required is usually about 1h. SPECT resolution is usually low due to complications of collecting unscattered gamma rays emitted from the source.

The resolution of such instrument depends on the time required for the scan, longer scans emit more radiation thus the detection could predict more accurately the position of the radioactive pharmaceutical. Typical spatial resolution for this technique is in the range of 5mm. Figure 2.3 shows a SPECT image of a brain where the coloured circles point out where seizures (in epilepsy) begin.

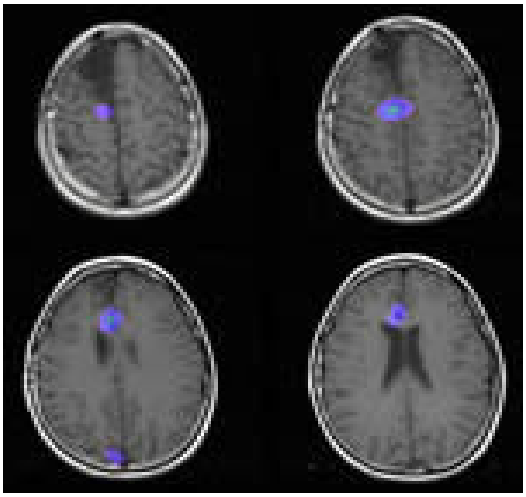

Figure 2.3: SPECT scan of a brain [8]

2.1.4 Magnetic Resonance Imaging (MRI)

Magnetic Resonance Imaging (MRI) or Nuclear Magnetic Resonance Imaging (NMRI) is a non-invasive technique and is primarily used in medicine to image physiological or other pathological living tissue alternations.

The working principle of MRI is based on monitoring the distribution of hydrogen atoms within the patient's organs [9]. The human body consists of billions of atoms. The nucleus of an atom spins, or precesses, on an axis [10]. The nucleus of an atom can be visualised as a top spinning somewhere off its vertical axis as shown in figure 2.4.

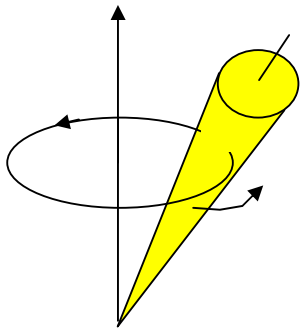

Figure 2.4: Nucleus of an atom as a top spinning somewhere off its vertical axis.

There are many different types of atoms inside the human body, but for purposes of MRI, we only consider the hydrogen atom. This atom is ideal for MRI because its nucleus has a single proton and a large magnetic moment, which means that when the hydrogen atom is placed inside a magnetic field it has the strong tendency to line up with the direction of the magnetic field (1.5T generated by electromagnets) as shown in figure 2.5 [11].

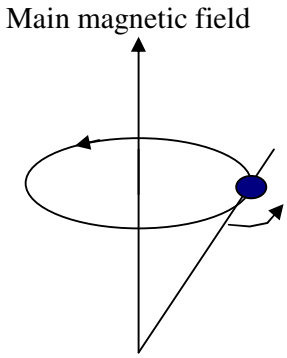

Figure 2.5: A hydrogen atom precesses about a magnetic field.

Inside the bore of the scanner, the magnetic field runs straight down the centre of the tube where the patient is located. If the patient is lying on his or her back in the scanner, the hydrogen protons will line up in the direction of either the feet or the head. The majority of these protons will in turn cancel out each other and only a couple out of every million are not cancelled out [11]. Although this is a low number, the sheer number of hydrogen atoms in the body will give the image. One essential advantage of MRI is that images can be weighted according to spin relation mechanisms, chemical shifts and spectroscopic functional information [10].

The depth of imaging is governed by the dimensions of the uniform magnetic field that is established within the bore of the magnet. Bores are large enough to pass a prone patient, permitting whole body or organ imaging. Image acquisition time is in the range of 50ms and imaging resolution of 0.5-1mm is achieved. An MRI image of a brain is presented in figure 2.6.

Figure 2.6: MRI image of a brain [12]

Newly developed MRI systems have been researched for microscopy that can generate an imaging resolution in the range 12μm using 7T field strength across 1cm magnet bores. (African frog) [13]

Unlike Computed Tomography (CT) which will be explained at the next section, MRI has greater soft tissue contrast making it more attractive for musculoskeletal, cardiovascular, neurological and oncological diseases. Furthermore open magnet MRI machines are now available to surgeons for image guided surgery application [11].

2.1.5 Computed Tomography (CT)

Computed tomography (CT) or computed axial tomography (CAT) is primarily used in medical imaging to plan surgical procedures and guide placement of needle biopsies. CT scans generate a three dimensional internal image of a patient from a large series of two dimensional X-ray images taken around a single axis of

rotation. CT uses X-rays that are emitted in a fan like pattern from the source and the detectors are placed in same pattern on the opposite side. When the patient is placed inside this doughnut shaped machine (figure 2.7) the X-ray source is rotated around him (360^{o}) and data are collected by the detection elements. Many X-ray slice data are taken when the patient is gradually passed through the gantry.

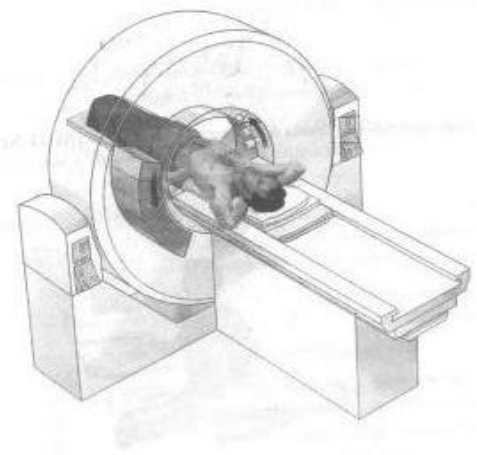

Figure 2.7: CT scan illustration [14]

In a single plane the resolution of a CT image is in the range of 0.5-1mm and when the patient is passed though in increments of 5-10mm multiple planes are acquired [15]. In turn all the data are acquired and combined and images are reconstructed using specific mathematical procedures. Image reconstruction times have been improved with the helical scanning method and acquisition of 3D volume data is achievable [16]. A typical axial scans usually takes 15sec. and 30-40 slices are obtained. The image contrast depends on the X-ray attenuation property of each human part thus highly attenuating parts like bone appear white and low attenuating parts dark [6]. Images reconstructed with this method are displayed in grey scale as shown in figure 2.8 where the bones appear to be whiter than the surrounding area.

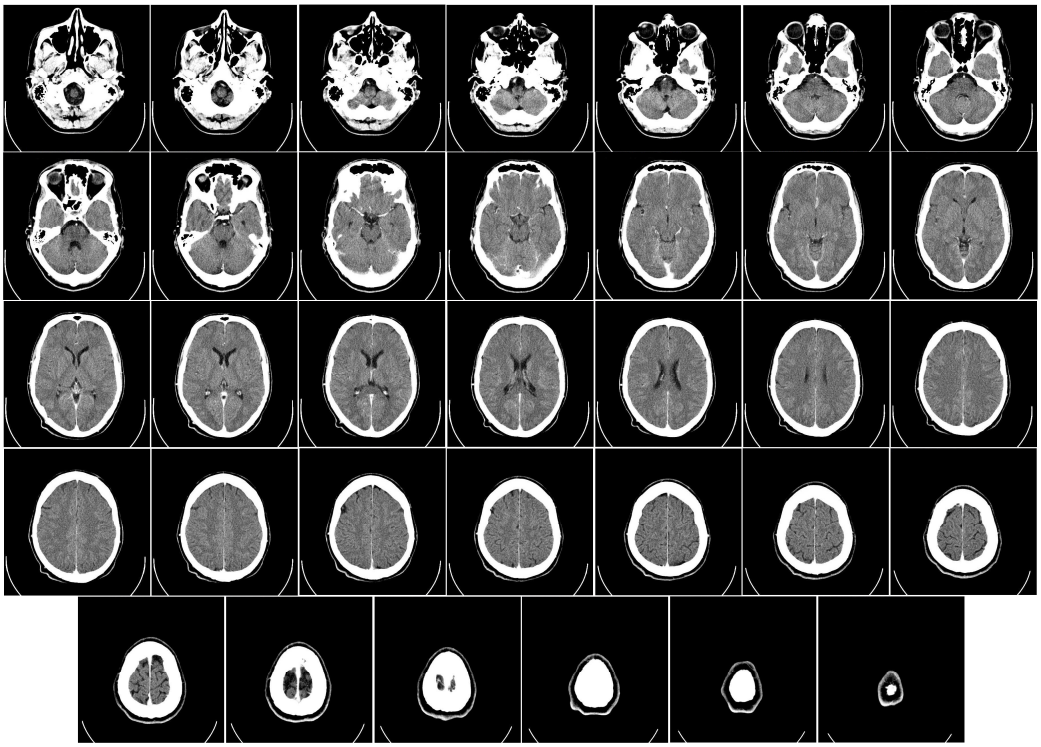

Figure 2.8: CT scan images of human brain from the base of the skull to top.[17]

Recent advancements in CT scanner permit the imaging of individual live bacteria with 200nm resolution [18]. The size of these machines though is quite large and often require a separate room to be placed and the cost of it also high in the range of £350,000 -£500,000 [19].

2.1.6 Ultrasound

Ultrasound or ultrasonography is a medical imaging technique primarily used to visualise muscles, tendons and other internal organs. Ultrasound is one of the most widely used diagnostic tools in modern medicine. The technology is relatively inexpensive (£20,000-£100,000) and portable [19], especially when compared with modalities such as MRI and CT. Ultrasound is a clinically safer imaging instrument as it does not use ionizing radiation, which imposes the hazard of cancer development [20]. The most famous application area of ultrasound is in obstetrics. Routine

ultrasound in early pregnancy (less than 24 weeks) appears to enable better gestational age assessment, earlier detection of multiple pregnancies and earlier detection of clinically unsuspected fetal malformation at a time when termination of pregnancy is possible [21].

The ultrasound system transmits high frequency (1- 20 MHz) sound pulses into the patients' body using a probe. This is a transducer made from piezoelectric materials that acts both as a pulse emitter and receiver. The probe then is scanned across the area of interest and some of the sound waves get reflected back to it, while some travel on further until they reach another boundary and get reflected. Contrast within ultrasound images is generated by differences in acoustical impedance within tissue. The reflected waves are then picked up by the probe. The machine calculates the distance from the probe to the tissue or organ boundaries using the speed of sound in tissue (1.540m/s) and the time of each echo return [21]. In ultrasound millions of pulses and echoes are sent and received each second. The machine then displays the distances and intensities of the echoes on the screen forming a 2D image as shown in figure 2.9 depicting a 2D image from a developing baby in the 13^{th} week.

In order to image an area with ultrasound the area should be covered with an impedance matching medium or gel. This gel or medium is used to match the acoustic impedances and increase conductivity [22]. The imaging resolution of ultrasound is in the range of 100-200μm at depths of tens of centimetres with the field of view depending on the distance scanned by the probe [21]. Clinical ultrasound machines acquire images at video rates of 30frames/sec. Furthermore 3D imaging is achievable by translating the probe along a third axis and collecting a series of 2D slices to form a 3D image [23].

Figure 2.9: Ultrasound 2D image of my developing baby Maria (23 weeks)

Ultrasound imaging has also been used in cardiology to visualise any abnormal structures or functions inside the heart and measure the blood flow [24, 25, 26]. Recently ultrasound probes have been incorporated onto the tips of endoscopes to image subsurface tissue structures [27] and onto rotating catheters for intravascular imaging of atherosclerosis and stenosis in the coronary artery [27].

2.2 Comparison of medical imaging techniques

Table 2.1 below provides a comparison of OCT with the other medical imaging modalities currently used in a clinical environment.

Because cell dimensions are of the order of a few μm it can be seen from table that the other techniques have a limited imaging resolution from 100μm to 1mm thus the resolution offered by them is not sufficient to spot any abnormalities like early types of numerous carcinomas. Furthermore from table 2.1 it can also be observed

that some of the techniques use ionising radiation which could be harmful for the patient. Moreover an OCT instrument is more cost effective with comparison to the other current clinical imaging instruments.

Table 2.1 : Comparison table of imaging techniques

	X-RAY	***CT***	***ULTRASOUND***	***SPECT***	***PET***	***OCT***
Ionising Radiation	YES	YES	NO	YES	YES	NO
Anatomy or Functional	A	A	A+F	F	F	A(+F)
Data Acquisition Time	1sec	5 min	1sec	20 min	20 min	10sec
Data Reconstruction Process Time	2min	2min	<1sec	10 min	10 min	<1sec
Patient Handling time	5min	30min	10min	30 min	30 min	10 min
Spatial resolution	<1mm	>1mm	>30μm	>5mm	>5mm	>1-15 μm
Depth	>body	>body	>body	>body	>body	3mm
Sensitivity (1 poor to 5 great)	2	4	3	3	4	3
Capital cost of equipment	£70k	£350-£500k	£10k	£200k	£0.5-2M	<55k

Therefore there are a number of compelling reasons that can be listed verifying the need of a medical imaging modality like OCT. From figure 2.10 it could also be realised that OCT could fill a gap in the medical imaging modalities as it

could actually assist in minimising the number of biopsies being performed thus leading in an early prognosis and diagnosis of diseases.

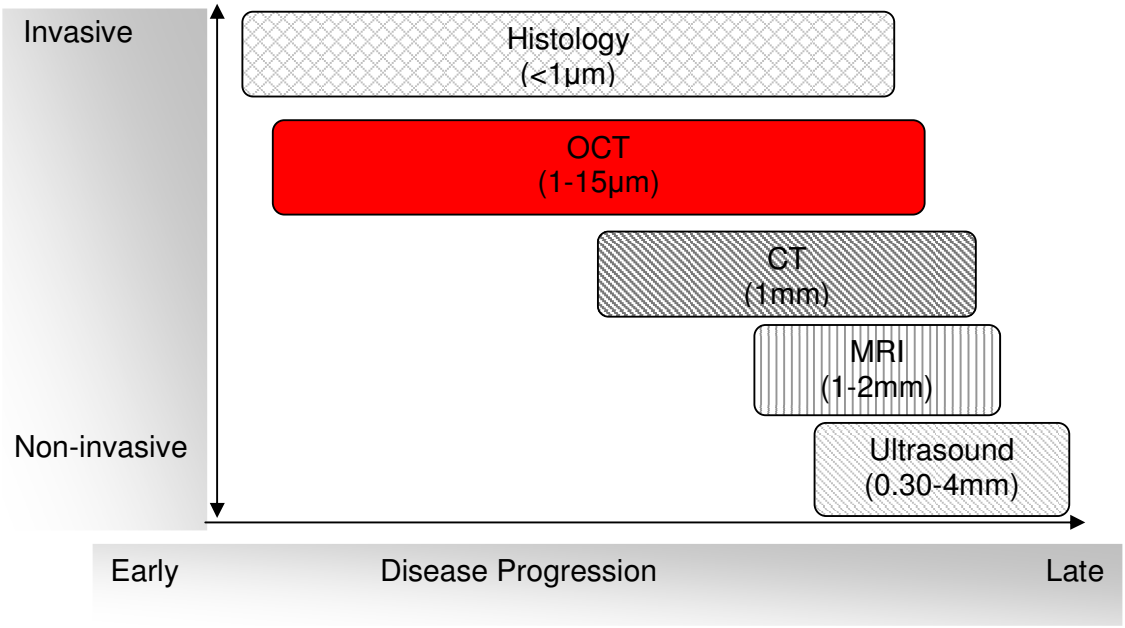

Figure 2.10: Comparison of medical imaging techniques

References

1. P. J. Douglas, Picturing people: non-intrusive imaging, *Foresight Exploiting the Electromagnetic Spectrum State of the Science Review*, Cavendish Laboratory, Cambridge University, 2004

2. D. Chapman, W. Thomlinson, R. E. Johnston, D. Washburn, E. Pisano, N. Gmür, Z. Zhong, R. Menk, F. Arfelli, D. Sayers, *Diffraction enhanced x-ray imaging*. Physics in medicine and biology, Vol. 42, 1997, pp2015-2025.

3. W.K. Roentgen, *On a new kind of rays*, Nature, Vol. 53, 1896, pp274-276

4. D. Manning, *The risk of cancer from radiography*, Radiography, Vol.10, Issue 3, 2004, pp171-172

5. American Cancer Society (ACS), weblink: http://www.cancer.org/docroot/NWS/content/NWS_1_1x_Viruses_Added_to_List_of_Cancer-Causing_Substances.asp [04/05/2007]

6. S. Webb, *The physics of medical imaging*. Institute of physics publishing, Bristol and Philadelphia, 1998

7. National Aeronautics and Space Administration (NASA), *Remote sensing tutorial,* weblink: http://rst.gsfc.nasa.gov/ [27/07/2005]

8. Children's hospital and regional medical centre of Seattle, Washington, website: http://neurosurgery.seattlechildrens.org/ [23/02/2005]

9. J. A. Markisz, M. G. Aquillia, *Technical magnetic resonance imaging,* Appleton & Lange: Stamford CT, 1996

10. R. E Jacobs, S. E. Fraser, *Imaging neural development with magnetic resonance imaging microscopy*, Journal of Neuroscience mehodology, Vol. 54, 1994, pp189-196

11. M. P. Black, T. Moriarty, E. Alexander, P. Stieg, E. J. Woodard, P.L. Gleason, C. H. Martin, R. Kikinis, R. B. Schwartz, F.A. Jolesz, *Development and implementation of magnetic resonance imaging and its neurological applications,* Neurosurgery, Vol. 41, 1997, pp831-843

12. Harvard medical school: http://www.med.harvard.edu/AANLIB/home.html [02/02/2008]

13. R. E Jacobs, S. E. Fraser, *Magnetic resonance microscope of embryonic cell lineages and movements*, Science, Vol. 263, 1994, pp681-684.

14. http://www.wikipedia.org [05/10/2006]

15. R. Allemond, *Basic technical aspects and optimisation problem in computed tomography,* In physics and engineering of medical imaging, Ed Guzzardi R, Pub., Martinus Nijhoff, Boston MA, 1987, pp207-217

16. J. A. Brink, *Technical aspects of helical(spiral) CT,* Radiologic clinics of north America, Vol. 33, 1995, pp825-841.

17. http://www.gehealthcare.com/usen/ct/case_studies/index.html [07/11/2006]

18. J. M. Rajyaguru, M. Kado, K. Nekula, M.C. Richardson, M. J. Muszynki, *High resolution x-ray micrography of live Candida albicans using laser plasma pulsed point x-ray sources,* Microbiology, Vol. 143, 1997, pp733-738

19. Medical device register-Official directory of medical suppliers*, Medical economics CO*, 1996, Monvale, NJ

20. F. S. Foster, C. J. Pavlin, G.R. Lockwood, L. K. Ryan, K. A. Harasiewicz, L. R. Berube, A. M. Rauth, *Principles and applications of ultrasound backscatter microscopy,* IEE Trans. Ultrason. Ferroelec. Freq. Contr., Vol. 40, 1993, pp608-617

21. L. Massoti, *Basic principles and advanced technical aspects of ultrasound imaging,* In physics and engineering of medical imaging, Martinus Nijhoff, Boston MA, 1987, pp263-317

22. F. S. Foster, C. J. Pavlin, K. A. Harasiewicz, *Advances in ultrasound* Ultrasound in Medicine and biology, Vol. 26, 2000, pp1-27

23. D. H. Sauder, F.S. Foster, *A 40-100MHz B-scan Ultrasound for skin imaging,* Ultrasound in Medicine and Biology, Vol. 21, 1995, pp79-88.

24. J. W. Winkelman, M. D. Kenner, R. Dave, R. H. Chandwayney, S. B. Feinstein, *Contrast echocardiography*, Ultrasound in Medicine and Biology, Vol. 20, 19994, pp3530-3533.

25. L. Hoff, *Acoustic properties of ultrasonic contrast agents,* Ultrasonics, Vol. 34, 1996, pp591-593.

26. N. De Jong, L. Hoff, T. Scotland, N. Born, *Absorption and scatter of encapsulated filled microspheres*: *Theoretical considerations and some measuments*, Ultrasonics, Vol. 30, 1992, pp95-103.

27. M. G. Hibberd, C. Vuille, A. E. Weyman, *Intravascular ultrasound: Basic principles and role in assessing arterial morphology and function,* Americal journal of cardiology and imaging, Vol. 6, 1992, pp302-324.

28. P. Chandratana, M. I Awaad, P. Chadrasoma, M. Khan, *High frequency ultrasound: Determination of the lowest frequency for cellular imaging and detection of myocardial diseases,* American heart journal, Vol. 129, pp 79-88.

29. D. H Turnbull, J.A Ramsay, G. S. Shivji, T. S. Bloomfield, L. From, D. N. Sauder, F. S. Foster, *Ultrasound backscatter microscope analysis of mouse melanoma progression,* Ultrasound in medicine and biology, Vol. 22, 1996, pp845-853.

Chapter 3

OCT THEORY

3. Theory

A mathematical framework for designing and analysing time domain OCT systems is developed in this chapter. OCT is based on low coherence or "white light" interferometry. The mathematics of low coherence interferometry is developed and the relationship between longitudinal resolution and coherence length in a Michelson interferometer is analysed.

For the purpose of examining the coherence properties of light we consider light as an electromagnetic radiation which can be as described in [1]:

$$E = E_0 e^{i(k\cdot r - \omega t + \varphi)} \tag{3.1}$$

k: is the wavenumber

φ: Optical phase

r: position vector

The radiation has wave trains with different lifetimes, and the average lifetime τ_0 is called the coherence time. The wave trains differ in phase because of the random processes producing the light, e.g. thermal excitation. Depending on what kind of source used, the produced light will have frequencies ω within a certain frequency spectrum. Using Fourier analysis, one has that [1]

$$\Delta\omega = 2\pi/\tau_0 \tag{3.2}$$

where $\Delta\omega$ is a measure of the spectral line width. From this it is seen that a broadband source with a large $\Delta\omega$ has a short coherence time τ_0. The coherence length L_c of a wave train is [1]:

$$L_c = c\tau_0, \tag{3.3}$$

where c is the speed of the wave. Using equation (3.2) one gets

$$L_c = c2\pi/\Delta\omega = c/\Delta\nu. \tag{3.4}$$

Using the relation

$$\nu_0 = c/\lambda_0 \tag{3.5}$$

where ν is the optical frequency, and approximating $\Delta\nu$ by the magnitude of its differential,

$$\frac{\Delta\nu}{\Delta\lambda} \approx \left|\frac{d\nu}{d\lambda}\right| = \frac{c}{\lambda^2} \tag{3.6}$$

we get

$$L_c \approx \lambda_0^2/\Delta\lambda \tag{3.7}$$

where $\Delta\lambda$ is a measure of the linewidth and λ_0 is the centre wavelength. This is only a somewhat intuitive derivation of the coherence length, and a precise definition is given in the next section.

3.1 Interferometry

Considering now the propagation of two collimated beams $E_1(r, t)$ and $E_2(r, t)$ emanating from the same source and travelling different paths as in the case of a Michelson interferometer depicted in figure 3.1.

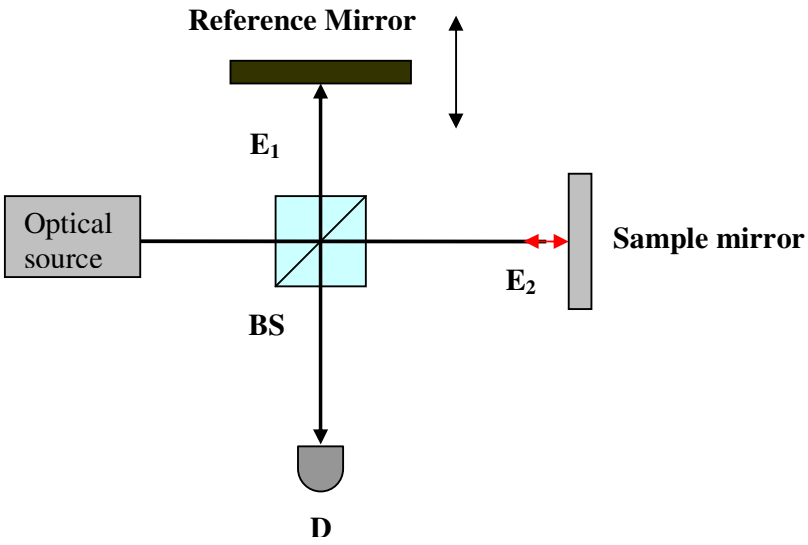

Figure 3.1: Michelson interferometer, BS:beamsplitter, D: Detector

If the beams meet at a point D and one beam has travelled the extra time τ, the resultant field at P is:

$$E_D(t) = E_1(t) + E_2(t + \tau) \tag{3.8}$$

using the principle of superposition. Inserting equation (3.1) and setting r and φ to be zero for convenience:

$$E_D(t) = E_{01}e^{-i\omega t} + E_{02}e^{-i\omega(t+\tau)}. \quad (3.9)$$

The power per unit area at D is given by the Poynting vector [2]:

$$S = \varepsilon_0 c^2 E_D \times B_D \quad (3.10)$$

Since E_D and B_D are rapidly varying fields (~10^{14} Hz for 1550nm light), the power per unit area (irradiance) I_P measured by a detector at D would be a time average of

$$S{:}I_P = \langle|S|\rangle = \varepsilon_0 c^2 \langle|E_D \times B_D|\rangle. \quad (3.11)$$

From electromagnetic theory it is known that E and B are orthogonal and that [2]

$|E|=c\,|B|$

This gives

$$I_P = \varepsilon_0 c \langle|E_D|^2\rangle = \varepsilon_0 c \langle E_D \cdot E^*_D\rangle. \quad (3.12)$$

Inserting equation (3.8) we get

$$I_P = \varepsilon_0 c\langle (E_1 + E_2) \cdot (E^*_1 + E^*_2)\rangle$$
$$I_p = \varepsilon_0 c \langle|E_1|^2 + |E_2|^2 + (E_1 \cdot E^*_2 + E_2 \cdot E^*_1)\rangle \quad (3.13)$$

Omitting the constant multiplicative factor $\varepsilon_0 c$ and writing the irradiances of the individual beams as I_1 and I_2:

$$I_P = I_1 + I_2 + 2\mathrm{Re}\langle E_1(t) \cdot E^*_2(t+\tau)\rangle \quad (3.14)$$

using now

$$A + A^* = 2\mathrm{Re}(A) \quad (3.15)$$

From this it is seen that if the two beams have the same polarization, the dot product is maximum:

$$\langle E_1(t) \cdot E^*_2(t+\tau)\rangle = \langle E_1(t)\, E^*_2(t+\tau)\rangle \quad (3.16)$$

Defining a correlation function

$$\Gamma_{12}(\tau) \equiv \langle E_1(t)\, E^*_2(t+\tau)\rangle \quad (3.17)$$

and a normalized correlation function

$$\gamma_{12}(\tau) \equiv \Gamma_{12}(\tau) / \sqrt{I_1 I_2} \text{ [2]} \tag{3.18}$$

The complex degree of coherence $\gamma_{12}(\tau)$ can thus be viewed as a Fourier transform of the power spectrum, as defined in [4].

Eq. 3.18 leads to:

$$I_P = I_1 + I_2 + 2\sqrt{I_1 I_2}\, \mathrm{Re}\,[\gamma_{12}(\tau)] \tag{3.19}$$

A known result from statistical optics is that $\gamma_{12}(\tau)$ can be expressed as [3]

$$\gamma_{12}(\tau) = \int_0^\infty S(\nu) e^{-i2\pi\nu\tau}\, d\nu \tag{3.20}$$

where $S(\nu)$ is a normalized power spectral density of the light source in the sense that [3]

$$\int_0^\infty S(\nu)\, d\nu = 1 \tag{3.21}$$

When the power spectral density is an even function of $(\nu - \nu_0)$, the complex coherence can be written as a product of a real-valued factor and $e^{-i2\pi\nu_0\tau}$ [3]. It is observed that the intensity will vary sinusoidally with τ, modulated with an envelope function γ_{12} determined by the Fourier transform of the spectrum.

$$\gamma_{12}(\tau) = \gamma_{12}(\tau) e^{-i2\pi\nu_0\tau}. \tag{3.22}$$

This gives

$$I_P = I_1 + I_2 + 2\sqrt{I_1 I_2}\gamma_{12}(\tau) \cos(2\pi\nu_0\tau) \tag{3.23}$$

Assuming that τ_0 is a constant coherence time and not an average, one can show that for harmonic waves with frequency ω_0 [2]:

$$\mathrm{Re}\,[\gamma_{12}(\tau)] = (1 - \tau/\tau_0)\cos(\omega_0\tau) \tag{3.24}$$

(for $\tau \leq \tau_0$) giving:

$$\begin{aligned} I_P &= I_1 + I_2 + 2\sqrt{I_1 I_2}(1 - \tau/\tau_0)\cos(\omega_0\tau) \\ &= I_1 + I_2 + 2\sqrt{I_1 I_2}\,(1 - \Delta l/L_c)\cos(k_0 \Delta l) \end{aligned} \tag{3.25}$$

using

$$\tau = \Delta l / c \tag{3.26}$$

where Δl is the difference in optical path length for the two beams, and

$$k_0 = 2\pi/\lambda_0 \tag{3.27}$$

where λ_0 is the wavelength of the waves. For $\tau > \tau_0$ the interference term vanishes because the random phase variations cancel out:

$$I_P = I_1 + I_2. \tag{3.28}$$

From this it is seen that the optical path difference Δl must be smaller than the coherence length in order to observe interference fringes or equal for maximisation. The factor

$$\gamma_{12}(\tau) = (1 - \Delta l/L_c) \tag{3.29}$$

comes from the assumption of constant coherence time τ_0. If instead the spectrum of the source is Gaussian, one obtains for the coherence function [3]

$$\gamma_{12}(\tau) = \exp[-(\pi \Delta\nu \tau / 2\sqrt{\ln(2)})^2] \tag{3.30}$$

which as expected is Gaussian, since the Fourier transform of a Gaussian function is itself a Gaussian function. $\Delta\nu$ is the FWHM of the normalized spectrum. It is seen that the maximum of $\gamma_{12}(\tau)$ is 1 and occurs when $\tau = 0$. Defining the coherence length

$$L_c = \tau_0 c$$

with the condition $\gamma_{12}(\tau_0) = 1/2$ gives

$$L_c = \frac{2\ln(2)}{\pi}\frac{c}{\Delta v} = \frac{2\ln(2)}{\pi}\frac{\lambda^2}{\Delta\lambda} \approx 0.44\frac{\lambda^2}{\Delta\lambda} \tag{3.31}$$

which is sometimes used in the OCT literature [5]. Δλ is the FWHM of the spectrum measured in wavelength units. If the coherence time is instead defined as the power-equivalent width (as defined in [6]) of the coherence function, the result is [3]

$$L_c = \sqrt{\frac{2\ln(2)}{\pi}}\frac{\lambda^2}{\Delta\lambda} \approx 0.66\frac{\lambda^2}{\Delta\lambda} \tag{3.32}$$

This definition is most widely used in the OCT literature and it can be seen that the coherence length is inversely proportional to the FWHM (Δλ) of the source used.

Since the coherence length is a measure of the width of the signal envelope, it is a reasonable estimate for the depth (axial) resolution in OCT: if the distance between two reflecting planes in the medium is smaller than the coherence length, the interference signals arising from each of the two planes will overlap, resulting in a smearing of the image contrast. In figure 3.2 below typical long and short coherence function from a Gaussian spectrum source are shown. In the case that the light source has a non Gaussian spectrum several abnormalities may occur. For example modulation or ripples in the source spectrum can cause echoes to appear in the axial point spread function [3]. Another example is the phenomenon of blindness. Blindness can occur if the tails of the point spread function are broad enough to prevent observations of a weak backreflected signal next to a strong reflected signal [3].

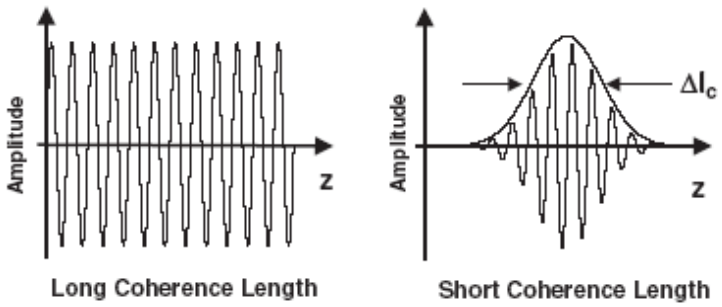

Figure 3.2: Long and short coherence length [2]

In the case of a Gaussian spectrum the axial point spread function that is also Gaussian has its tails decaying exponentially with the squared path mismatch between the reference and the sample arm.

3.2 Transverse Resolution

The axial resolution of the OCT system is inversely proportional to the width of the power spectrum of a Gaussian source. The transverse resolution of an OCT system though is the same as for conventional microscopy and is determined by the focusing properties of an optical beam. The minimum spot size to which an optical beam can be focused is inversely proportional to the Numerical Aperture (NA) of the beam.

$$\Delta x = \frac{4\lambda}{\pi}\left(\frac{f}{d}\right) \tag{3.33}$$

Where d is the spot size of the objective lens and f is the focal length. High transverse resolution can be obtained by using a large NA and focusing the beam to a small spot size. In addition the transverse resolution is also related to the depth of focus or the confocal parameter b, which is $2z_R$, two times the Rayleigh range.

$$2z_R = \pi \Delta x^2 / 2\lambda \tag{3.34}$$

Thus increasing the transverse resolution produces a decrease in the depth of focus. Figure 3.3 shows the relationship between the focused spot size and depth of focus for high and low NA.

Although high transverse resolution can be achieved, the depth of focus would be limited. To perform imaging over a range of depths it is necessary to track the focal depth along the axial range (reference delay) that is being detected. Alternatively it is possible to use a technique analogous to ultrasound called C-Mode scanning and acquire multiple images with different zones of focus and fuse them together to create a single image with extended depth of field [7].

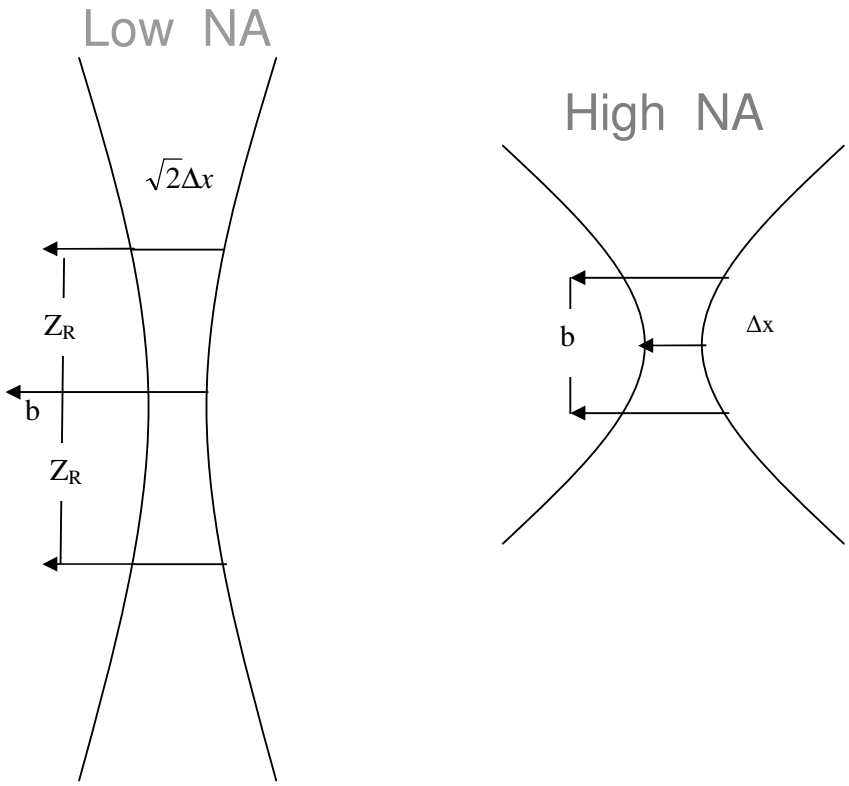

Figure 3.3: Low and High NA focusing limits of OCT.

.

3.3 Methods of Illumination

Cross sectional imaging of OCT is performed by successive axial measurements of the backreflected light at different transverse positions [8]. Figure 3.4 shows a two dimensional cross-sectional image that is acquired by scanning the incident optical beam, and performing successive rapid axial measurements. For visualisation purposes the OCT data are displayed as a 2D grey-scale or false colour image. The pixel density of an OCT image is determined by the image acquisition conditions and the analogue to digital conversion parameters. So if each axial scan covers a given depth with a given axial resolution the axial scan data must be sampled at a density two times the resolution or higher [9]. In the transverse direction for optimum resolution the number of transverse pixels should be chosen according to the transverse resolution.

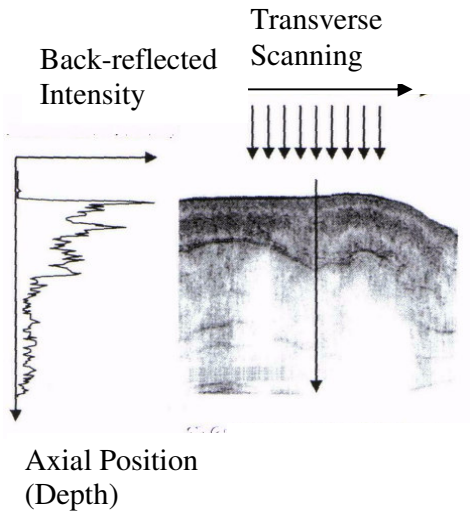

Figure 3.4: Cross sectional image 200pixels (horizontal) by 500pixels (vertical) of the retina and refractive index profile (A-scan) [8].

However since this generates a high number of transverse pixels, OCT images are usually under sampled in the transverse direction [10]. In addition there is a wide range of OCT scan patterns that are possible as depicted in figure 3.5.

The most frequently used method of OCT to acquire data is with depth priority [11, 12]. On the other hand it's also possible to acquire data with transverse priority by detecting the back-reflection at a given depth or range while transversely scanning the beam [13]. An OCT cross-sectional image can be produced by detecting the back-reflections along successive x-scans for different depths. Finally it is also possible to create cross-sectional OCT images in an en-face plane by detecting the back-reflected signals at a fixed depth when scanning along x and y directions [14, 15]. This method is somewhat analogous to the method used in confocal microscopy but can create error when the sample under test is moving [14].

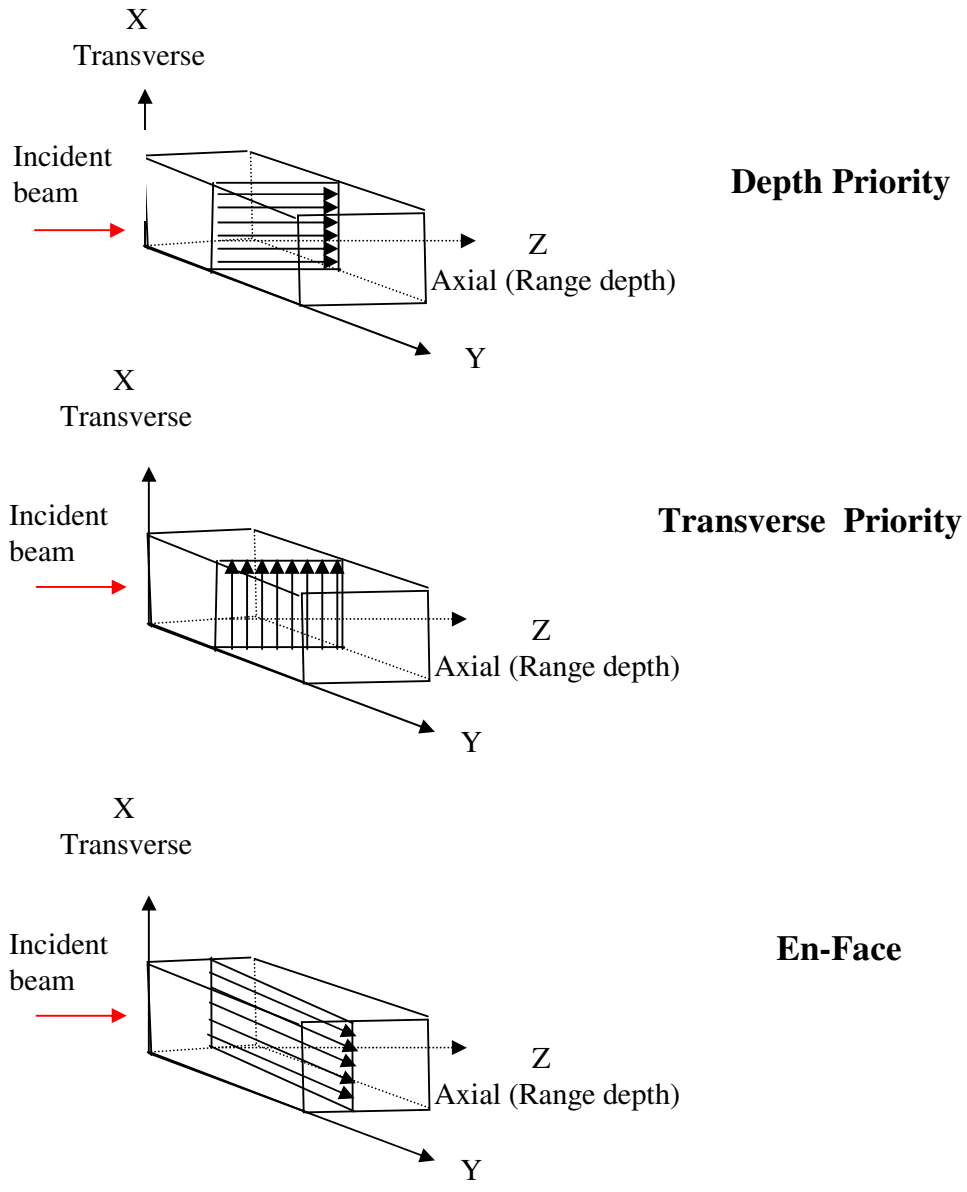

Figure 3.5: Different scanning methods for OCT

3.4 Detection-Filtering

As section 3.1 showed the interferometric signal consists of an axial point spread function envelope superimposed on a carrier frequency. Thus an electronic circuit is required to extract the envelope of the detected signal. In an OCT system as the reference mirror travels at a velocity V_r the axial point spread function which is a

function of the path length mismatch Δl is mapped into a function of time. The carrier frequency caused by the oscillating reference mirror creates a beat frequency at the photodetector after mixing with the unshifted light returning from the sample mirror. The detection circuits used to extract this interferometric signal can be categorised into three main areas. After the photodetector

1) a transimpedance amplifier will follow with a gain of R to convert the photocurrent I to voltage V

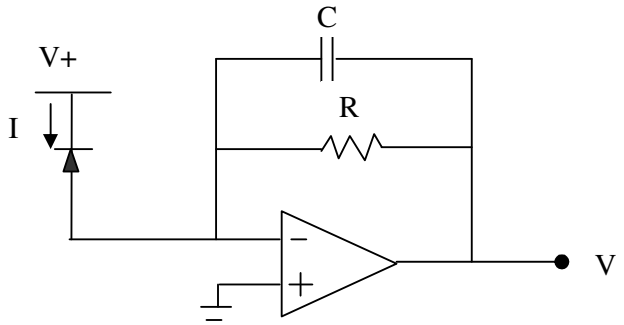

Figure 3.6: Transimpedance amplifier

2) possibly a bandpass filter with a transfer function centred at the carrier frequency to separate the actual signal from the DC current and noise

3) and an amplitude demodulation mechanism that will extract the envelope from the interferometric signal.

Finally the envelope extracted is to be digitised and stored on a hard drive of a computer. The amplitude demodulation can either be done by multiplication of the interferometric signal by a sinusoidal reference at the carrier frequency followed by a low-pass filter or by envelope detection that entails rectification (square law detection) followed by a low pass filter again. Envelope detection though is more advantageous when the phase or the frequency of the carrier has nonlinear variations for example nonlinearities of the translated reference mirror.

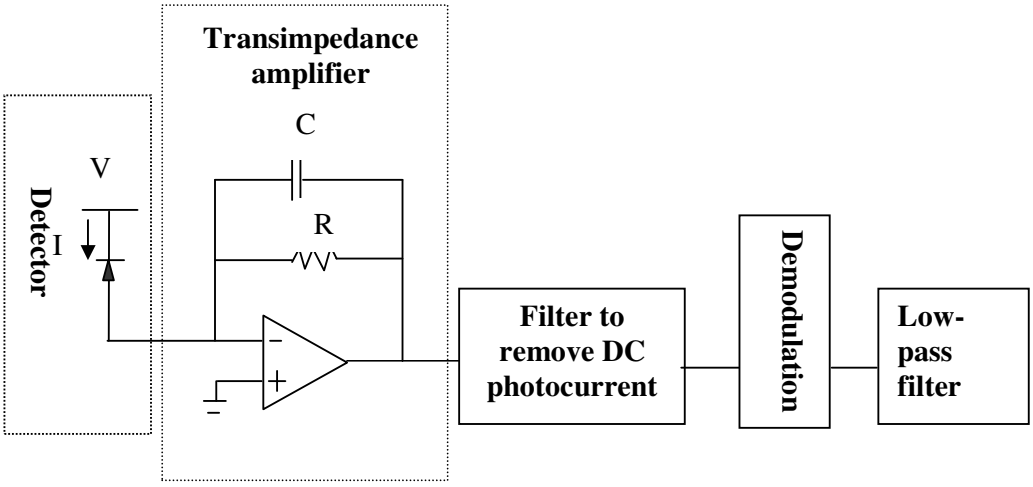

Figure 3.7: Block diagram for OCT electronic

3.5 Fizeau interferometer based OCT

One of the objectives of this work is to investigate the use of Fizeau interferometer for an OCT system. By analogy to the Michelson interferometer a mathematical framework is presented for a Fizeau interferometer based OCT accompanied by a balancing processing Michelson interferometer as shown in figure 3.8 [16]. For the presented Fizeau-type OCT in figure 3.8 the reference reflection is derived from the reflection at the end of the delivery fibre. Thus the reference beam and the sample beam traverse a common path within the optical fibre section of the interferometer. Due to the inherent optical path difference between the two beams an additional balancing/processing interferometer is required.

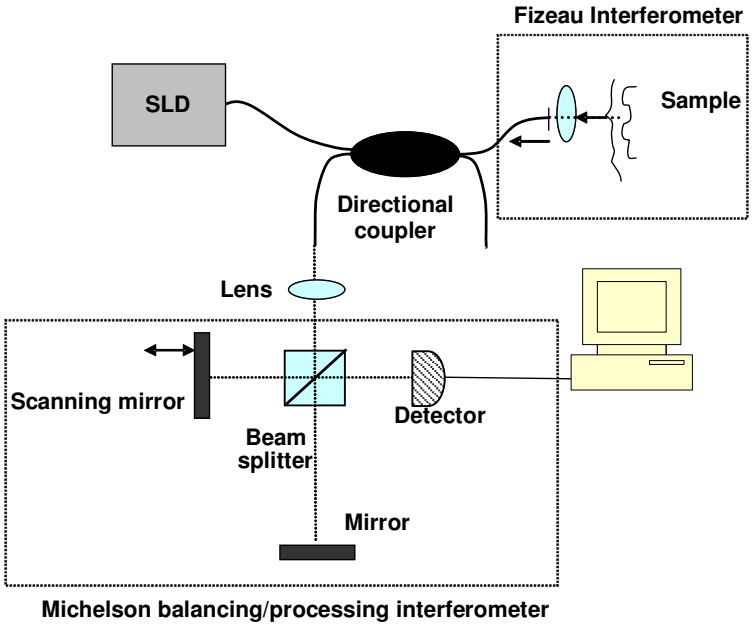

Figure 3.8: Fizeau interferometer based OCT with a Michelson balancing/processing interferometer.

The transfer function of the described configuration is detailed below. The electric fields at the output of the processing Michelson interferometer are expressed:

$$E = E_{11} + E_{12} + E_{21} + E_{22} \tag{3.35}$$

where E_{ij} is the component of the electric field arising from propagation of the beam via the jth arm of the Fizeau interferometer and the ith arm of the Michelson interferometer.

Thus it could be written that:

$$E_{11} = A_{11} e^{i\Phi} \tag{3.36}$$

$$E_{12} = A_{12} e^{i(\Phi + kX_1)} \tag{3.37}$$

$$E_{21} = A_{21} e^{i(\Phi + kX_2)} \tag{3.38}$$

$$E_{22} = A_{22} e^{i(\Phi + k(X_1 + X_2))} \tag{3.39}$$

A_{ij}: is wave amplitude of each electric field Eij,

k: is the wavenumber

φ: Optical phase

X_1, X_2: is the optical path difference between the Fizeau interferometer and the Michelson

The optical intensity I is defined taking the time average of the equation 3.35 which is the product of the overall output electric field E and its complex conjugate:

$$
\begin{aligned}
I &= \langle EE^{*} \rangle \\
&= \left\langle \left(E_{11} + E_{12} + E_{21} + E_{22}\right)\left(E_{11}^{*} + E_{12}^{*} + E_{21}^{*} + E_{22}^{*}\right) \right\rangle \\
&= \left\langle E_{11} E_{11}^{*} \right\rangle + \left\langle E_{12} E_{12}^{*} \right\rangle + \left\langle E_{21} E_{21}^{*} \right\rangle + \left\langle E_{22} E_{22}^{*} \right\rangle \\
&+ \left\langle E_{11} E_{12}^{*} \right\rangle + \left\langle E_{12} E_{11}^{*} \right\rangle + \left\langle E_{11} E_{21}^{*} \right\rangle + \left\langle E_{21} E_{11}^{*} \right\rangle \\
&+ \left\langle E_{11} E_{22}^{*} \right\rangle + \left\langle E_{22} E_{11}^{*} \right\rangle + \left\langle E_{12} E_{21}^{*} \right\rangle + \left\langle E_{21} E_{12}^{*} \right\rangle \\
&+ \left\langle E_{21} E_{22}^{*} \right\rangle + \left\langle E_{22} E_{21}^{*} \right\rangle + \left\langle E_{12} E_{22}^{*} \right\rangle + \left\langle E_{22} E_{12}^{*} \right\rangle
\end{aligned}
\tag{3.40}
$$

By analogy to the Michelson based OCT [24] it can be shown that:

$$\frac{\left\langle E_{11}E_{12}^{*}\right\rangle + \left\langle E_{12}E_{11}^{*}\right\rangle}{\sqrt{I_1 I_2}} = 2\left|\gamma\left(X_1\right)\right|\cos\left(kX_1\right) \tag{3.41}$$

$$\frac{\left\langle E_{11}E_{21}^{*}\right\rangle + \left\langle E_{21}E_{11}^{*}\right\rangle}{\sqrt{I_1 I_3}} = 2\left|\gamma\left(X_2\right)\right|\cos\left(kX_2\right) \tag{3.42}$$

$$\frac{\left\langle E_{11}E_{22}^{*}\right\rangle + \left\langle E_{22}E_{11}^{*}\right\rangle}{\sqrt{I_4 I_1}} = 2\left|\gamma\left(X_1 - X_2\right)\right|\cos\left(kX_1 - X_2\right) \tag{3.43}$$

$$\frac{\left\langle E_{12}E_{21}^{*}\right\rangle + \left\langle E_{21}E_{12}^{*}\right\rangle}{\sqrt{I_2 I_3}} = 2\left|\gamma\left(X_1 + X_2\right)\right|\cos\left(k\left(X_1 + X_2\right)\right) \tag{3.44}$$

$$\frac{\left\langle E_{12}E_{22}^{*}\right\rangle+\left\langle E_{22}E_{12}^{*}\right\rangle}{\sqrt{I_2 I_4}}=2\left|\gamma(X_2)\right|\cos(kX_2) \tag{3.45}$$

$$\frac{\left\langle E_{21}E_{22}^{*}\right\rangle+\left\langle E_{22}E_{21}^{*}\right\rangle}{\sqrt{I_3 I_4}}=2\left|\gamma(X_1)\right|\cos(kX_1) \tag{3.46}$$

$$\begin{aligned} I = I_0 &+ 2\left(\sqrt{I_1 I_3}+\sqrt{I_2 I_4}\right)\left|\gamma(X_2)\right|\cos(kX_2)+2\left(\sqrt{I_1 I_2}+\sqrt{I_3 I_4}\right)\left|\gamma(X_1)\right|\cos(kX_1) \\ &+2\sqrt{I_2 I_3}\left|\gamma(X_1+X_2)\right|\cos(k(X_1+X_2))+2\sqrt{I_1 I_4}\left|\gamma(X_1-X_2)\right|\cos(k(X_1-X_2)) \end{aligned} \tag{3.47}$$

I_1, I_2, I_3, I_4: intensities of E_1 and E_2.

3.6 Signal-to-Noise Ratio (SNR)

The value of the SNR for an OCT system must exceed that required to resolve the small refractive index variations (around 0.01-0.1) typical of biological tissue [17]. The combination of low power and high bandwidth implies that the SNR could be relatively low for standard detection techniques and careful considerations have to be made when designing the OCT system.

For the SNR calculation the optical power in the reference beam P_r corresponding to power reflectivity R_r, the optical power from the sample beam P_s corresponding to reflectivity R_s and the optical power P_x from stray incoherent light at the detector corresponding to power reflectivity R_x is taken into account.

The maximum SNR of an OCT system [18] is defined as the ratio of the mean square signal photocurrent $\left\langle I_s^2\right\rangle$ from the detector, under path-matched conditions, to the total photocurrent variance σ_i^2.
It is given by:

$$SNR = 10\log_{10}\left(\frac{\left\langle I_S^2 \right\rangle}{\sigma_i^2}\right) \tag{3.48}$$

$\left\langle I_s^2 \right\rangle$ is a function of the optical power in the reference and sample beams.
Three sources of noise are to be considered in calculating the SNR for OCT systems:

1. **Receiver noise**, which arises due to the random thermal motion of electrons within the photodetector. For commercial photodetectors, the receiver noise is usually specified in terms of NEP (Noise Equivalent Power (W/√Hz)), and it is given by :

$$\sigma_{re}^2 = \rho\,(NEP)^2\,B \tag{3.49}$$

B: detection bandwidth [19].
ρ: photodetector responsivity

2. **Shot noise**, depends upon the average photocurrent I_{dc} at the detector and arises from the random distribution in the arrival times of photons at the detector from the source. The shot noise photocurrent variance σ_{sk}^2 that is from the Poisson process is:

$$\sigma_{sh}^{\ 2} = 2qI_{dc}B \tag{3.50}$$

q: is the electronic charge.

3. **excess photon noise**, which is formed from the random arrival of photons from a broad band light source. This is a Bose-Einstein process, with different statistics from shot noise, the photocurrent variance is given by [20]:

$$\sigma_{ex}^{\ 2} = I_{dc}^{\ 2}\frac{B}{\Delta\nu} \tag{3.51}$$

Δν :is the frequency linewidth of the source.

However, in some OCT configurations where dual detectors are used [21] a phase difference between the beams arriving at the two detectors can be observed for stray, incoherent beams arising from unwanted reflections [22]. For such a case the beating that occurs between non-coherent spectral components of the broadband source gives rise to a form of noise called beat noise that is given by:

$$\sigma_{be}{}^{2} = \rho^{2} P_x P_r B / \Delta\nu \tag{3.52}$$

For the Michelson interferometer based OCT the beat noise could be present due to scattering at the end of the fibre. This could be minimised by polishing the fibre end or using some index matching gel.

3.6.1SNR mathematical expressions for various configurations

A Michelson optical-fibre configuration for OCT system using a single detector, is shown in figure 3.9 the splitting element is a directional coupler with a split ratio of a/(1-a). Ignoring other losses in this configuration, the optical powers P_x, P_s, P_r, received at the detector are :

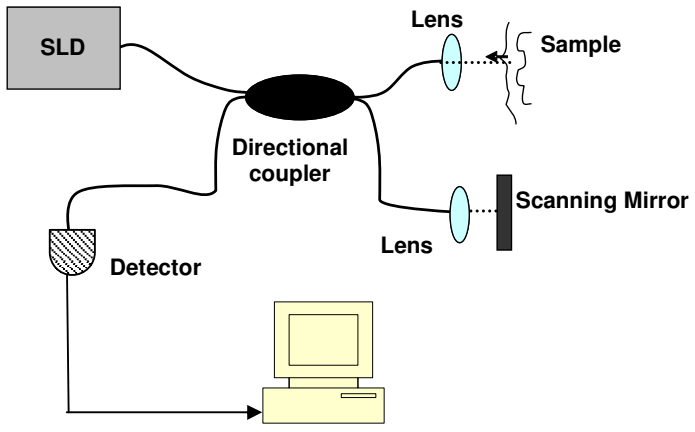

Figure 3.9 : Fibre Michelson interferometer based OCT

$P_s = P_0 a R_s (1-a)(1-R_x)^2$ (3.53)

$P_r = P_0 (1-a) R_r a$ (3.54)

$P_x = P_0 a R_x (1-a)$ (3.55)

P_0: initial power

The interference term produces a periodic signal photocurrent Is, which varies cosinusoidally as the interferometer phase θ is scaned linearly,

$$I_s = 2\rho \left[P_0^2 a^2 (1-a)^2 R_r R_s (1-R_x)^2 \right]^{1/2} \cos\theta \quad (3.56)$$

and the average photocurrent is given by I_{dc}

$$I_{dc} = \rho (P_r + P_s + P_x)$$

$$= \rho P_0 a (1-a)[R_s(1-R_x)^2 + R_r + R_x] \quad (3.57)$$

Calculating the shot noise and excess noise from these expressions, a value of the SNR for that configuration will be obtained. Previous theoretical studies [23] for such a configuration revealed that SNR turns out to be almost independent of the split ratio -a- over a very wide range of values from 0.05 to 0.95. Although maximum SNR was shown at a=0.5. Furthermore this research revealed that for R_s=1 the expected SNR should be in the range of 62dB and for R_s=0.001 the SNR is reduced to 52dB. Maximum SNR of 67dB was observed when Rs=0.1 since the reference and signal intensities are matched at this value, and all signal light contributes to the generation of interference fringes.

The basic form of the Fizeau interferometer based OCT system as shown shown in figure 3.8 makes poor use of the available light as 75% of the power is lost in the system. This configuration also suffers from drawbacks such as that the maximum theoretical SNR for a given source and detector is much lower than that for the Michelson-based system and this could be one of the causes that this configuration hasn't been investigated in detail [24]. However, as it will be discussed in chapter 6 the use of optical circulators and interferometer processing configurations can restore the SNR value to be comparable with that for the Michelson configuration.

For the simplest form of a Fizeau based OCT system as depicted in figure 3.8 there is no advantage in the variable splitting ration thus 50:50 splitting ration is assumed. If a lossless 50:50 beam splitter is in the Michelson interferometer, the longer beam path in the Michelson is denoted by the subscript a, and the shorter path by the subscript b. The powers arriving at the detector are given by:

$$P_{sa}=P_{sb}=\frac{P_0(1-R_r)R_s}{16} \tag{3.58}$$

$$P_{ra}=P_{rb}= P_0R_r/16 \tag{3.59}$$

In this configuration only two of these four components, P_{sb} and P_{ra}, are path matched at the detector and the interference term is given by:

$$I_s=2_\rho\ (P_{sb}\ P_{ra})1/2\ \cos\theta$$

$$I_s=\frac{2\rho}{16}\left[P_0^2R_sR_r(1-R_r)\right]^{1/2}\cos\theta \tag{3.60}$$

Previous theoretical research on Fizeau configurations for OCT systems [23] showed that for various reflectivities the SNR was ranging approximately from 60 to 94dB which is a more than a sufficient value for medical imaging applications. This research will aim to explore the SNR value of a time domain Fizeau based OCT experimentally.

References

1. Keigo Lizuka*, Elements of photonics*, Vol. 1, Wiley & Sons Inc., New York, 2002.

2. F. L. Pedrotti , L. S. Pedrotti, *Introduction to optics*, Prentice-Hall International, Inc., 2nd edition, 1996.

3. J. W. Goodman, *Statistical optics*, John Wiley & Sons, ISBN 0-471- 01502-4, 1985.

4. E. Saff, A. Snider, *Fundamentals of complex analysis for mathematics*, s*cience and engineering,* Prentice Hall, 2nd edition, ISBN 0-13-327461-6 , 1993

5. J.M. Schmitt, *Optical Coherence Tomography (OCT): A Review*, IEEE Journal of selected topics in quantum electronics Vol.5, Issue 4, 1999, pp1205-1215.

6. B. Saleh and M. Teich, *Fundamentals of photonics*, JohnWiley & Sons, ISBN 0-471-839-65-5, 1991.

7. W. Drexler, U. Morgner, F. X. Kaertner, C. Pitris, S. A. Boppart, X. D. Li, E. P. Ippen, J. G. Fijimoto, *In-vivo ultrahigh optical coherence tomography,* Optics Letters, Vol. 24, 1999, pp1221-1223.

8. V.V. Tuchin, *Handbook of coherent domain optical Methods: Biomedical diagnostics, Environment and material science*. Kluwer Academic Publishing, NY, 2005.

9. D. Huang, E. A. Swanson, C. P. Lin, J. S. Schuman, W. G. Stinson, W. Chang, M. R. Hee, T. Flotte, K.Gregory, C. A. Pualifito, J. G. Fujimoto, *Optical coherence tomography,* Science, Vol. 254, 1991, pp1178-1181

10. A. G. Podoleanu, J. A. Rogers, D. A. Jackson, S. Dunne, *Three dimensional OCT images from retina and skin*. Optics Express, Vol. 7, 2000, pp292–298.

11. C.A. Puliafito, M.R. Hee, J.S. Schuman, J. G. Fujimoto, *Optical coherence tomography for ocular disease*. Thorofare, NJ:Slack Inc.,1995

12. J. S. Schuman, M.R. Hee, C. A. Pualifito, C. Wong, T. Pedut-Kloizman C. P. Lin CP, E. Hertzmark, J.A Izaat, E. A. Swanson, J. G. Fujimoto, *Quantification of nerve fibre layer thickness in normal and glaucomatous eyes using optical coherence tomography*, Arch. Opthalmology, Vol.113, 1995, pp586-596.

13. G. J. Tearney, M. E. Brezinski, J.F. Southern, B. E. Bouma, S. A. Boppart, J. G. Fujimoto, *Optical biopsy in human gastrointestinal tissue using optical coherence tomography*. American Journal of Gastroenterology, Vol. 92, 1997,pp 1800–1804.

14. A. G. Podoleanu, G. M. Dobre, D. J. Webb, D. A. Jackson, *Simultaneous en-face imaging of two layers in human retina by low coherence reflectrometry,* Optics Letters, Vol. 32, 1997, pp1039-1041.

15. A. G. Podoleanu, G. M. Dobre, D. J. Webb, D. A. Jackson, *En-face coherence imaging using galvanometer scanner modulation,* Optics Letters, Vol. 23, 1998, pp147-149.

16. R. Beddows, S.W. James and R.P. Tatam, Proceedings of the 15th International Conference on Optical Fibre Sensors, Portland, Oregon, USA, 6–10 May, 2002 (IEEE, New York, 2002), pp. 527–530.

17. J. Qu, C. MacAulay, S. Lam, B. Palcic, *Laser-induced fluorescence spectroscopy at endoscopy: tissue optics, Monte Carlo modelling and in vivo measurements*. Optical Engineering, Vol. 34, 1995, pp3334–3343

18. A.M. Rollins, J.A. Izatt, *Optimal interferometer designs for optical coherence tomography*, Optics Letters, Vol. 24, 1999,pp 1484–1486

19. B.M Oliver, *Signal-to-noise ratios in photoelectric mixing*, Proceedings IRE, Vol**.** 49, 1961

20. H. Hodara, *Statistics of thermal and laser radiation*, Proceeding IEEE, Vol. 53, 1965, pp696-704.

21. A. C. Akcay, K. S. Lee, L. R. Furenlid, M. A. Costa, J. P. Rolland, *Compact low-cost detection electronics for optical coherence imaging***,** Optical engineering, Vol. 45, Issue 7 2006, p 070504.

22. K. Takada, *Noise in optical low-coherence reflectometry*, IEEE Journal of Quantum Electronics, Vol. 34, Issue 7, 1998, pp1098-1108.

23. H. D. Ford, R. Beddows, P. Casaubieilh, R. P. Tatam, Comparative signal-to-noise analysis of fibre-optic based optical coherence tomography systems, Journal of Modern Optics, Vol. 52, No. 14, 2005, 1965–1979.

24. K. Bamford, K., H. Barr, R. P. Tatam, *Optical low coherence tomography of bronchial tissue,* Advanced materials and optical systems for chemical and biological detection, SPIE symposium, 1999, pp172-179.

Chapter 4

OCT APPLICATIONS REVIEW

4. Historical Review

OCT as stated before is a recently developed medical imaging technology. The idea of using high speed optical gating to perform imaging in scattering systems such as biological tissue was proposed by *M. Duguay* in the late seventies [1,2,3]. *Duguay* proposed an ultra fast optical Kerr shutter to photograph light in flight. He used a Kerr shutter that could achieve picosecond resolution and operate by using an intense ultra short light pulse to induce birefringence -Kerr effect- in an optical medium placed between crossed polarisers. The observations that he made were that the optical scattering limits imaging resolution in biological tissues and that a high speed shutter could be used in a way to gate out unwanted scattered light and detect light reflections from internal structures.

The disadvantage of that approach was that the Kerr shutter required high intensity laser pulses to induce the Kerr effect and operate the shutter. Moreover an

alternative approach for high speed gating is to use second harmonic generation. In this technique the sample that is being imaged is illuminated with short pulses and the backreflected light is parametrically converted with a reference beam in a nonlinear optical crystal. Nonlinear optical gating measures the time delay and intensity of high speed optical signals. The time resolution is determined by the pulse duration and the sensitivity is determined by the conversion efficiency of the nonlinear process.

Optical time-of-flight ranging measurements were first demonstrated in biological tissues to measure corneal thickness and the depth of the stratum corneum and epidermis [3]. Dynamic ranges of 10^6 or higher could be achieved. Finally it's worth noting again that this technique detects the intensity rather than the electric field of the backscattered light.

Interferometric detection overcomes many of the limitations of the nonlinear gating technique and can measure the back reflected light with high dynamic range and high sensitivity. This technique is analogous to coherent optical detection in optical communications for locating faults or defects in optical fibres that comprise an optical communications network (*Takada, Yokohama, Chida, Noda et. al*, 1987) [4]. Faults in fibre produce a partial or complete reflection of incident optical pulses. Launching optical pulses through the optical fibres, faults can be detected by measuring the time delay between the original and reflected pulse. This technique is called optical time domain reflectometry (OTDR) and the instrumentation has been reviewed by *Healy et. al.* in 1986) [5]. The resolution of this technique is 0.5m over 125 km. Analogous to optical ranging in fibres, optical ranging can be performed in biological tissue because every interface will reflect a portion of the incident optical beam.

OCT is based on Low Coherence Interferometry (LCI) first described by *Sir Isaac Newton.* LCI was used to characterise optical echoes and backscattering in optical fibres and waveguide devices [6, 7]. The first medical applications of LCI were in ophthalmology [8]. The sections to follow will outline some of the current OCT applications.

4.1 Applications in ophthalmology

One of the reasons that the study of the eye has been considered as a possible OCT application is that the eye is a transparent medium where light can pass through with minimal scattering. The first biological application of OCT was presented by Huang *et al.*[9], in 1991 when OCT was used to perform 2D imaging of the human retina.

For this study a fibre Michelson OCT system was used with a light source at 800nm with axial resolution of 10μm. Figure 4.1 below depicts the human eye structure.

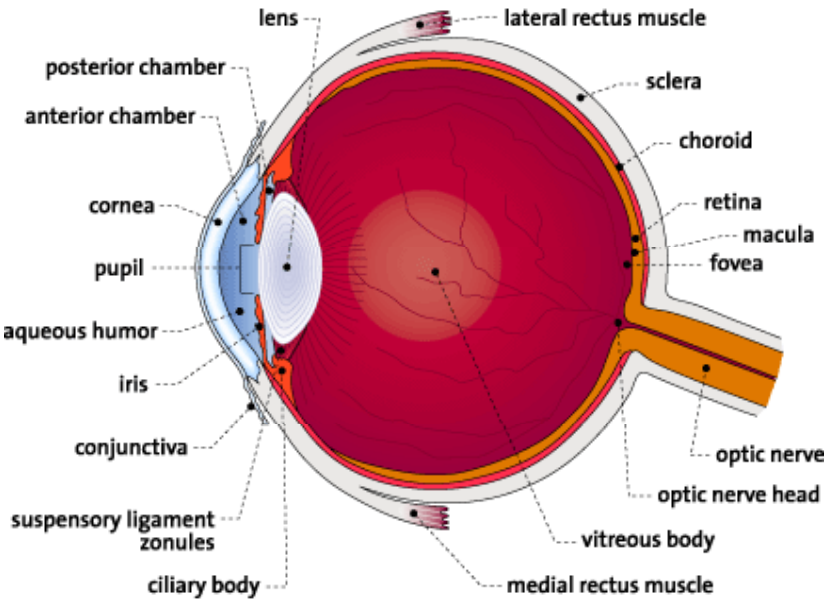

Figure 4.1: Structure of human eye [10].

The first in vivo tomograms of the human optic disc and macula were demonstrated in 1993 [11, 12]. The use of OCT in ophthalmology is nowadays the most mature application for this technique as it enables non contact non invasive imaging of the anterior eye and retina [13, 14, 15]. Figure 4.2 shows an example of an

early OCT retinal image. This image has 10µm axial resolution and demonstrates the ability to visualize retinal morphology including foveal contour, optic nerve head contour, and the retinal nerve fibre layer (see fig. 4.1). The highly backscattering retinal nerve fiber layer (NFL) and choriocapillaris appear in red.

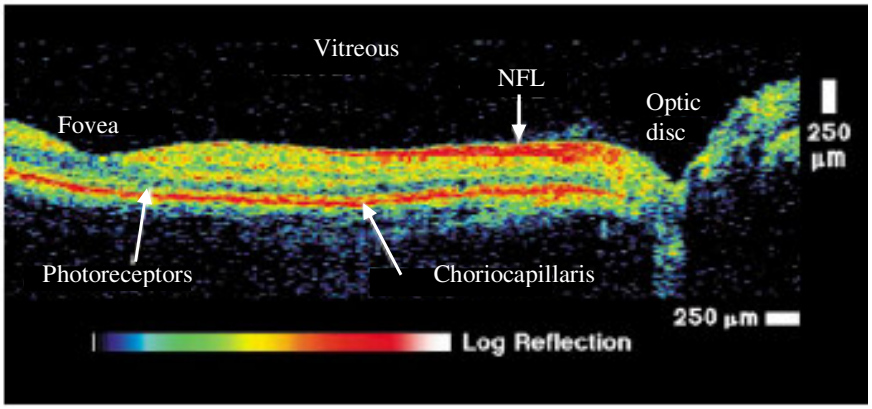

Figure 4.2: Example of an early OCT image of the normal retina in vivo. The retinal nerve fibre layer which emanates from the optic disc and decreases in thickness toward the macula can be clearly visualized [16].

Later in 1995 OCT was used to detect and monitor several macular diseases by *Hee et al*., 1995; like macular holes [17] by *Puliafito, Hee, et al*., [18]. A macular hole is a small hole in the macula which is in the centre of the retina. The macula is the part of the retina which is responsible for our sharp, detailed, central vision [10]. People with a macular hole will probably have changes in the central part of their vision [10]. These changes can range from straight lines looking wavy in the early stages to a small blank patch in the centre of vision in the late stages [10]. People could first notice that they have trouble reading small print or that there is distortion when they look at a printed page. Figure 4.3 illustrates the macular hole progression from an early stage to a late stage for a human eye.

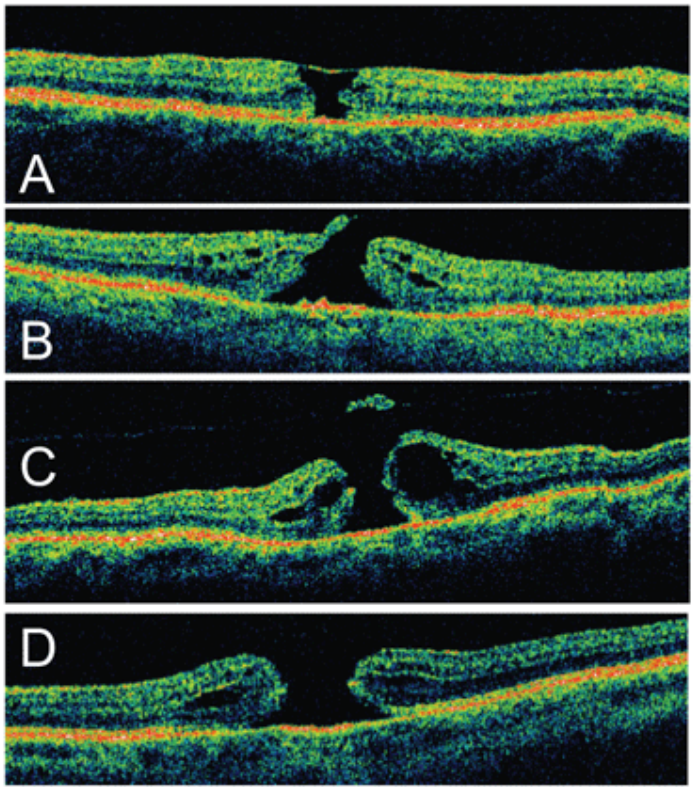

Figure 4.3: Series of OCT images of a macular hole generation for a human eye [19].

OCT has also been used in ophthalmology to image macular edema [20] this research was carried by *Puliafito, Hee, Schuman, Fujimoto* in 1995. Often macular edema occurs when fluid and protein deposits collect on or under the macula of the eye [10]. Thus it causes the central area of the retina to thicken and swell. The swelling could distort a person's central vision, as the macula is near the centre of the retina at the back of the eyeball [10]. An OCT image of macular edema is shown in figure 4.4. Note that the normal foveal pit is absent and is replaced by intraretinal fluid and retinal thickening.

In 1996 OCT has also been used to image age related macular degeneration [21]. Age related macular degeneration is a progressive disease of the retina wherein the light-sensing cells in the macula stop working and eventually die [10].

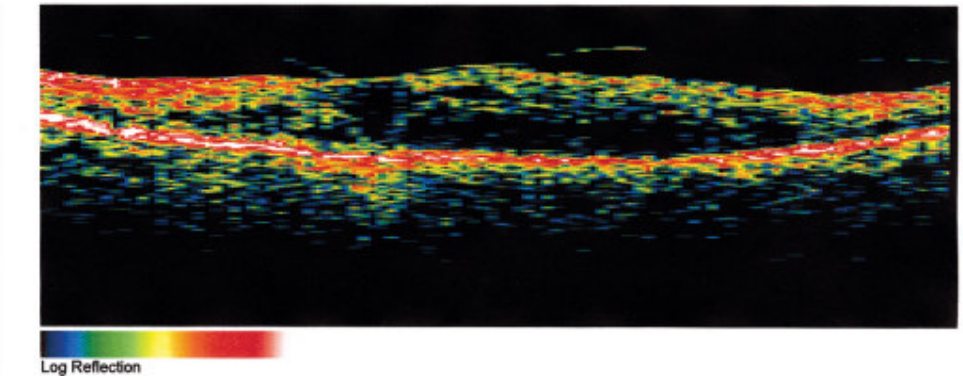

Figure 4.4: OCT image of the diabetic macular edema [22].

Furthermore the retinal fibre layer thickness that is a predictor for early glaucoma can also be quantified in normal and glaucomatous eyes and correlated with conventional measurements of the optic nerve structure and function [23, 24, 25, 26]. In addition OCT systems have also been used for the evaluation of choroidal tumors [27]. Choroidal melanoma (tumor) is a primary cancer of the eye and it arises from the pigmented cells of the choroid of the eye. Figure 4.5 below illustrates some segments of the eye that have been imaged by *Rollins et.al.* in 2002.

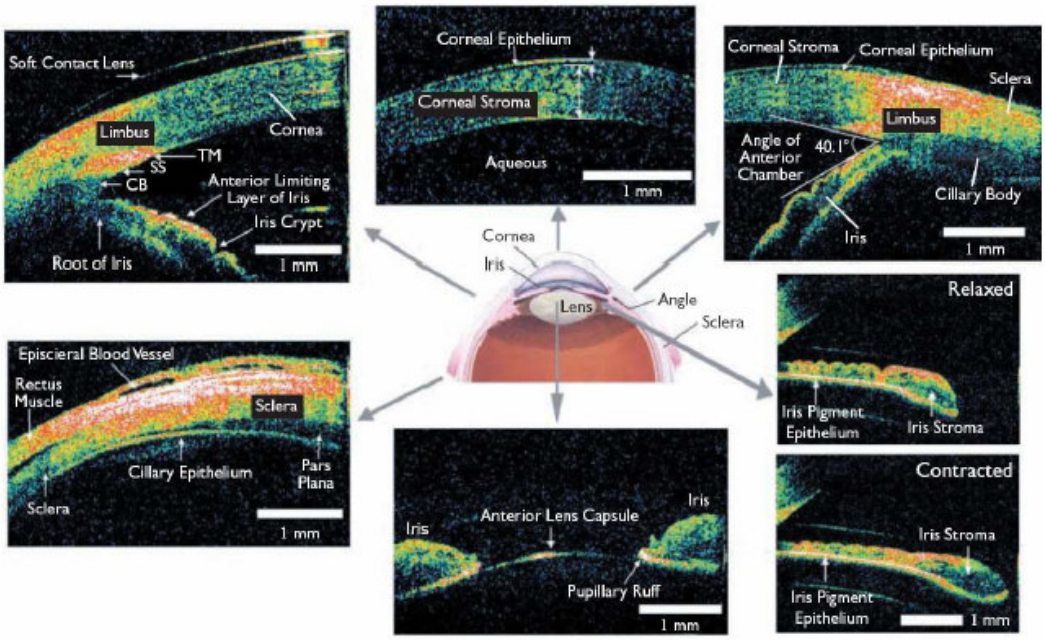

Figure 4.5: Segments of a normal eye being imaged with an OCT system [28].

Moreover retinal OCT images have also been correlated with histology by *Toth, Narayan, Boppart, Hee et al* in 1997 [29]. Developments in this area have demonstrated retinal imaging at 3μm resolution, permitting the differentiation of individual retinal layers [30]. Commercially available OCT instruments are nowadays and used to assess retinal diseases associated with diabetic retinopathy including macular edema and thinning of the retinal nerve (Bowd *et a*l., 2001;[31] Williams *et al*., 2002[32]).

Concluding OCT can provide diagnostic value information for several eye diseases. OCT images can then be analysed and processed using intelligent algorithms to extract thickness information of various part of the eye [33].

4.2 Applications in dermatology

In dermatology the main diagnostic methods that are currently used are visual inspection, histology and high frequency ultrasound (> 15MHz). Visual inspection is performed by experienced doctors allowing the investigation of the uppermost layers of the human skin and is a non expensive method. Ultrasound as explained in previous chapter can perform non-invasive depth resolved imaging at a depth of 6mm at low resolution (100μm) and the histology in conjunction with microscopy can provide a high resolution of 1μm but surgical excision of the area of interest is required. Obviously it would be advantageous to use OCT for such an imaging application as it can offer resolution close to that of histology non-invasively [34]. The structure of human skin is depicted in figure 4.6. In general the human skin is composed out of three layers: the epidermis, the dermis and the hypodermis that have different functionalities. The thicknesses of these layers are presented in table 4.1 [35].

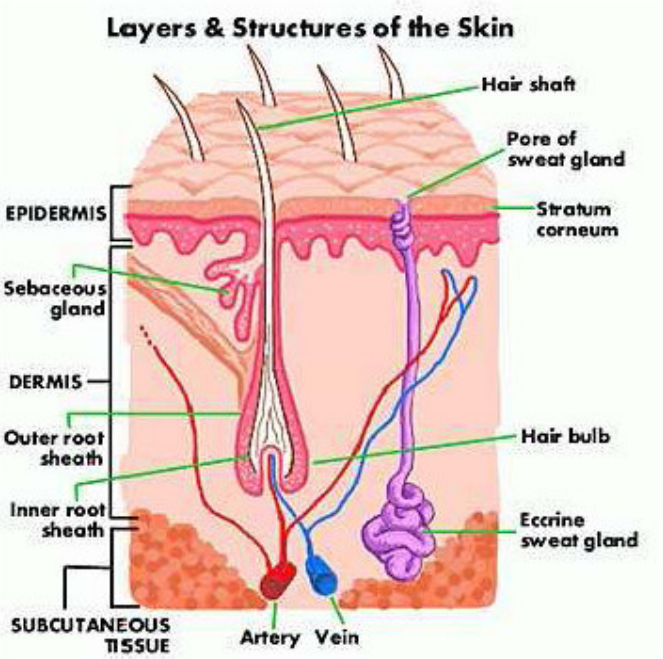

Figure 4.6: Structure of human skin [36]

Table 4. 1: thicknesses of skin layers

Layer	Thickness
Stratum corneum	0.01 - 0.02 mm
Epidermis	0.027-0.15mm
Dermis	0.6-3 mm
Hypodermis	Up to 3 cm

Stratum corneum is the outermost layer of the epidermis. Although most of the OCT images in dermatology are used to get a qualitative impression of a lesion they can also be used to gain a quantitative data about pathology. The most obvious measurements are thickness measurements as they can provide additional information to judge the healing of wounds or the effect of a cosmetic surgery [37]. An OCT image of of a fingertip is shown in figure 4.7 depicting stratum corneum (~500µm thick) on top and at the bottom superficial parts of the dermis. Sweatducts are clearly visible.

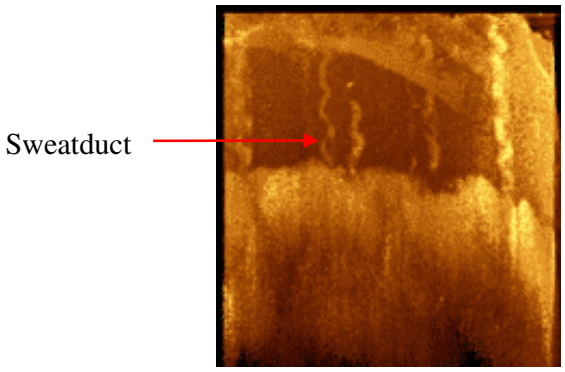

Figure 4.7: OCT image of a fingertip [38]

Another valuable imaging application in dermatology for OCT would be the investigation of melanocytic tumours. A malignant melanoma is a malignant tumour developing at first in the epidermis and then infiltrating the dermis. In 1998, *Boppart et al.* [37] investigated the potential use of OCT for such application. In OCT images of malignant melanoma the light scattering is more intense and more homogeneous than in healthy skin. OCT images produced from this research were compared with the corresponding histological examination and are presented in figure 4.8 below.

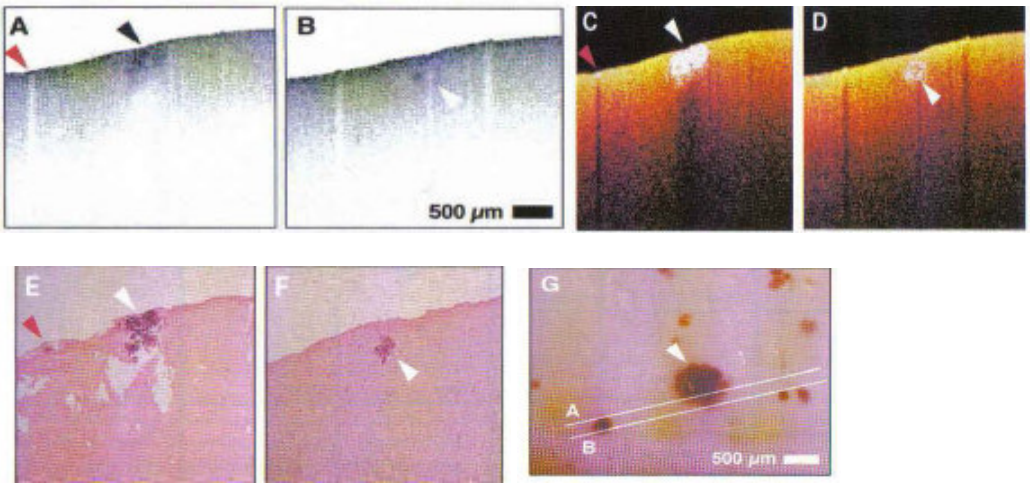

Figure 4.8: A,B,C,D are the OCT image from a malignant tumor, EF is the corresponding histology and G is an image taken with a digital camera from the top of the sample [37]

Moreover OCT has also been used for tumor diagnostics and detection of early neoplasia in a range of other organ systems, including the brain (*Boppart, Brezinski, Pitris, Fujimoto*, 1998 [39]; *Fujimoto, Pitris, Boppart, Brezinski*, 2000 [40]).

4.3 Applications in dentistry

OCT in dental imaging is offering a safe method of imaging dental microstructure for dental health evaluation. Dental applications of OCT include the diagnosis of periodontal diseases [41], detection of caries [42] and evaluation of dental restoration integrity [43]. OCT can detect oral problems before a conventional X-ray image can and this is due to the high spatial resolution offered by OCT. The result of this early diagnossis could lead to an earlier and less-damaging treatment of diseased teeth. Dental OCT imaging was first reported in 1998 by *Colston et. al.* [42] where 2D image data where captured for the hard and soft tissue structure of the oral cavity. For illustrative purposes an OCT image showing a molar crown is depicted in figure 4.9.

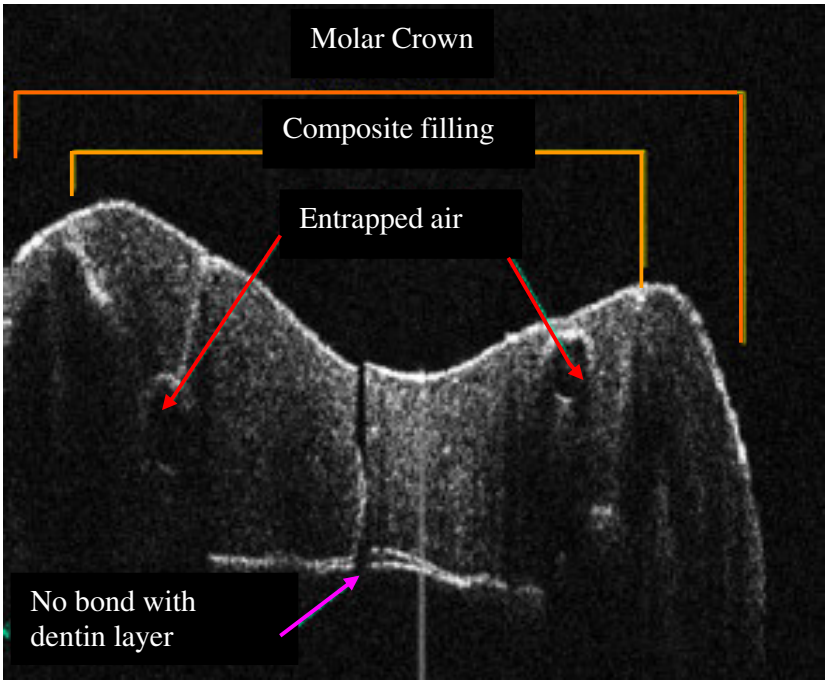

Figure 4.9: 3D OCT image of a molar crown [44]

4.4 Applications in cardiology

The capability of OCT to perform in vivo real time imaging can be important for a variety of clinical scenarios like imaging tissue pathology where a classic excisional biopsy would be hazardous or impossible. In ophthalmology for example biopsy of the retina is impossible and OCT could provide the means of imaging this sector of the eye where other techniques are not capable. Another scenario where biopsy is impossible is the imaging of atherosclerotic plaque morphology in coronary arteries [45, 46].

In the United States approximately 1.5 million patients every year suffer an acute myocardial infarction (AMI) [47]. Despite the effort to improve early diagnosis and prognosis of the patients, the mortality from AMI remains high, approaching 30% of all cases, 60% of which occur prior to hospitalization [47]. Myocardial infarctions as recent research showed result from the rupture of small to moderately sized cholesterol-laden coronary artery plaques followed by thrombosis and vessel occlusion [48, 49]. It was also discovered that the plaques with the highest risk of rupture are those that have a structurally weak fibrous cap [49]. The fibrous cap is a layer of fibrous connective tissue, which is thicker and less cellular than the normal intima. The intima is the innermost layer of an artery or vein [48]. It is generally accepted that plaques with a fibrous cap thickness of less that 30-65μm are prone to rupture [50]. Figure 4.10 depicts the anatomy of a human artery and its different layers.

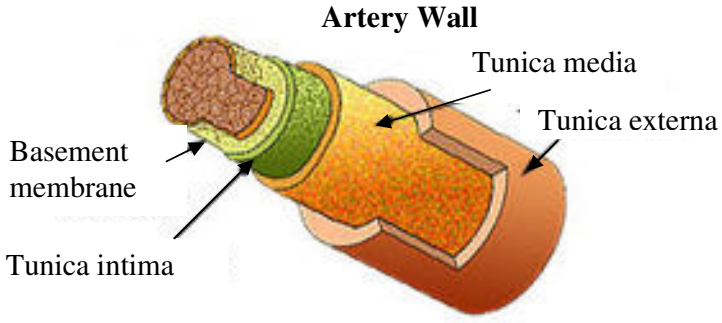

Figure 4.10: Anatomy of an artery [51]

Using conventional radiological techniques these plaque morphologies are difficult to detect. Thus identifying the high risk unstable plaques and delivering an early diagnosis for patients at risk of myocardial infractions could lower the high percentage of occlusions resulting in sudden death [49]. The high resolution of OCT makes it a promising imaging technology for the diagnosis of vulnerable plaques in arteries. Early work for this OCT application was carried out by *Brezinski, Tearney, Weissman, et al*., in 1997 [52] demonstrating the feasibility of OCT to diagnose arterial pathology. Figure 4.11 depicts cross sections of an artery with different imaging modalities.

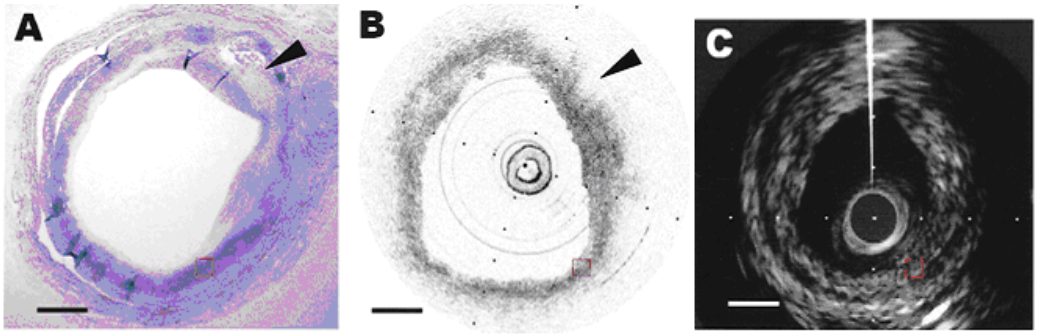

Figure 4.11: a) Histological image b) Optical coherence tomography image c) Conventional intravascular ultrasound image [53].

Histology detected the lipid pool was (arrowhead in A). Optical coherence tomography detected the same lipid pool as a homogenous, diffusely bordered, signal-poor region (arrowhead in B). The lipid pool could not be clearly discriminated by conventional intravascular ultrasound.

4.5 Applications in gastrointestinal

Epithelial cancers of the gastrointestinal tract, reproductive tract, and the respiratory tract comprise the majority of cancers encountered in internal medicine. Many epithelial cancers are preceded by pre-malignant changes, such as dysplasia

[54]. The term dysplasia refers to the abnormality in maturation of cells within a tissue and is often indicative of an early tumor process [54]. This consists of an expansion of immature cells, with a corresponding decrease in the location and number of mature cells [55]. Endoscopic instruments have been used extensively in such application as they can provide access to the mucosal surface of the esophagus, stomach etc [56]. These endoscopes though can provide a magnification in the order of x10 to x100 just for the surface of the submucosa with a limited resolution of 100μm to 50μm [57]. Essential depth information can not be provided with such endoscopes thus generating a number of compelling reasons to use OCT for gastrointestinal operation. In 1996 *Izaat et. al* [58] described the use of a mechanically scanned fibre based OCT endoscope and obtained images of esophagus in vivo. This system though was still in the experimental phase and was designed for clinical use as it required 100 s. to obtain a single image. In 1997 *Tearney et. al.* [59] reported another in-vivo experiment using autopsy specimens. In this configuration the sample arm of the OCT was mechanically scanned across the tissue in an acquisition period of 45s. but this system was again unsuitable for clinical use.

The following year *Kobayashi et al*. [60] used again such a system to obtain high resolution cross-sectional images of the GI tract. Results showed clear definition of the mucosa and submucosa layers within the tissue. An SLD of 1270 nm wavelength was used to obtain images of 19.2 μm resolution to a depth of 1.2 mm. OCT images were compared with images produced after histological examination a paradigm of such comparison is shown in figure 4.12. Figure 4.12 depicts the different layers and structures of the tissue that were identified with this OCT system. In this experiment the blood vessels were identified and their diameter was measured to be in the order of 0.5 mm.

The endoscopic capability of OCT is one of its great advantages thus several improvements are continuing to be made to increase the resolution and speed [61]. Image quality comparison for images taken from an esophagus between early endoscopic OCT systems and a modern ultra high resolution OCT system was performed in 2008 by *Fujimoto et. al*. [62]. Figure 4.13 successfully illustrates that the image produced by the modern OCT system has reduced speckle size and resolves finer morphological features as indicated by the arrows.

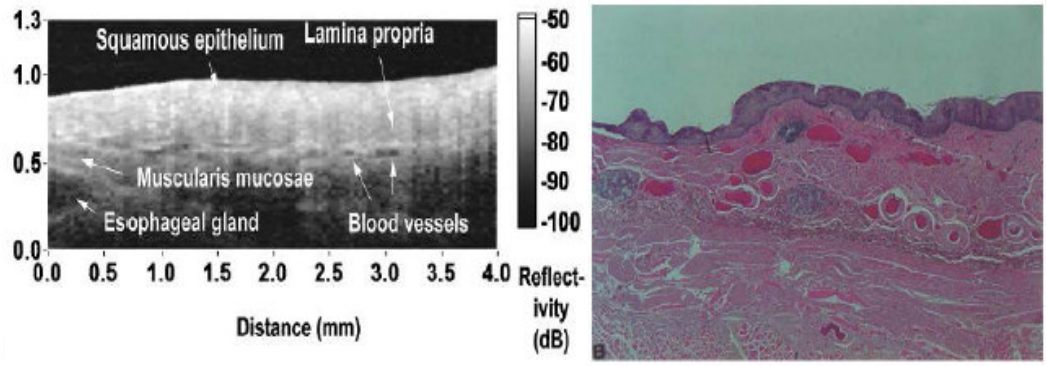

Figure 4.12: Left OCT image from esophagus and right the corresponding image produced by histology [60].

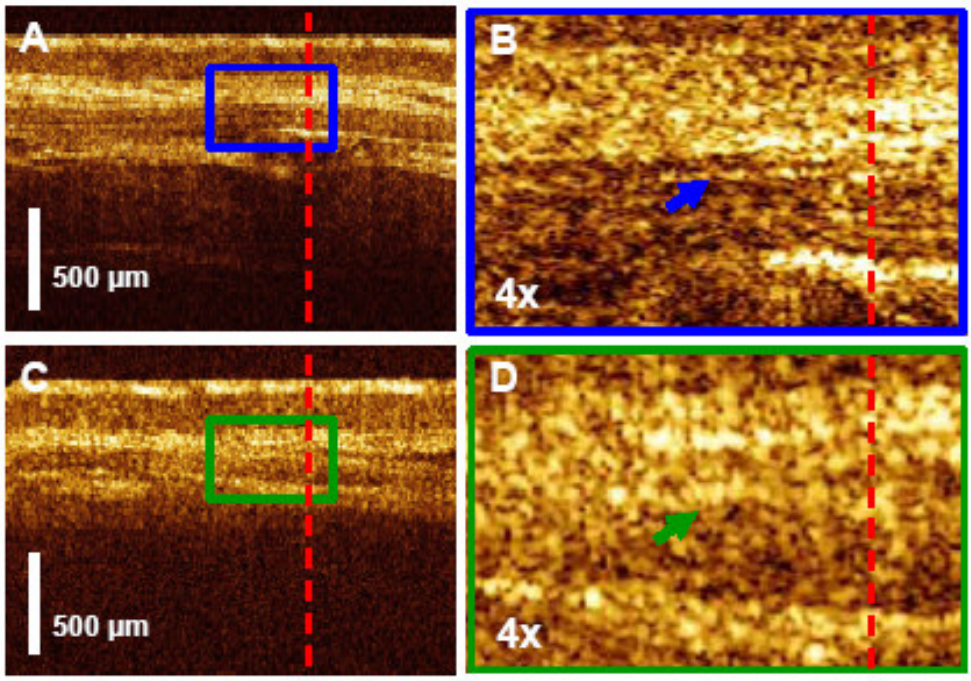

Figure 4.13: In vivo OCT imaging of normal esophagus with a modern high resolution OCT system in (A) and x4 magnification in (B) (C) Standard resolution OCT image with 4x magnification in (D) [62].

Figure 4.14 below illustrates the different sectors of the GI tract that have been imaged by *Rollins et. al* [63] in 2002 using a catheter based OCT system.

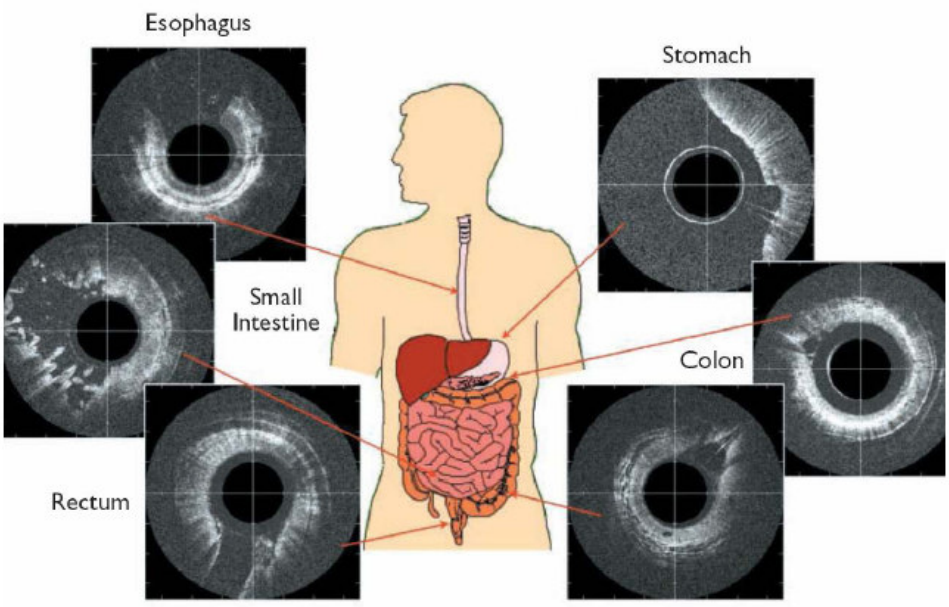

Figure 4.14: In-vivo OCT images of different sectors of the GI tract. [63]

4.6 Applications in other biological sciences

OCT has also found applications in developmental biology [64, 65, 66]. This field seeks to answer fundamental questions like how a fertilised egg can develop into a multi-cellular complex organism. For the answer towards these question researchers use several animal such as Brachydanio rerio (zebra fish) [64], and Xenopus laevis (African frog) [65] that have rapidly developing morphology on a size scale. Recent advances permitted researchers to site specifically modify genomes of these animal models. Modifying the genome and observing the mutations taking place and how they are expressed in the developing organism, functions of these genes can be determined. The capabilities of OCT as discussed previously will assist to observe the expressions of genes in vivo.

OCT was first demonstrated in developmental biology in 1996 [67] and was used to examine the morphology of developing tadpoles. In this study an SLD was

used with a coherence length of 16μm and with a transverse resolution of 30μm. Figure 4.15 (a) illustrates an African frog during its tadpole stage and (b) 3D cross sectional OCT image containing 640 x 640 x 512 pixels acquired in about 30 seconds with a commercial OCT system from *Thorlabs Inc*.[68]. As it can be seen internal organs are clearly visible.

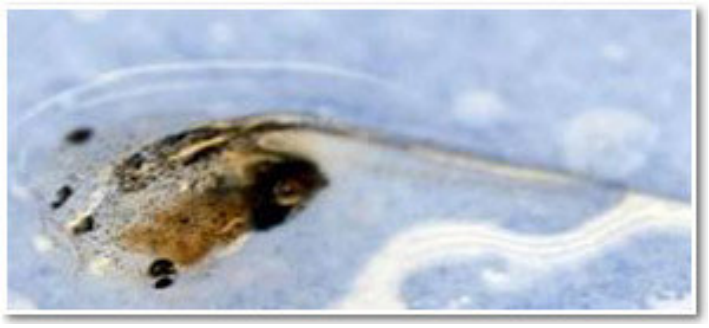

(a)

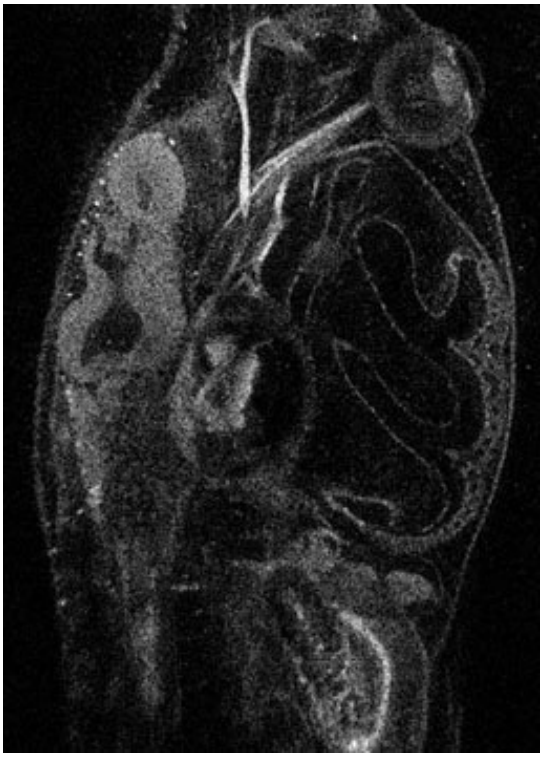

(b)

Figure 4.15: a) Image African frog during its tadpole stage (b) corresponding 3D cross sectional OCT image [68]

Several improvements are continuing to be made for imaging resolution that permit the visualization of individual cells and cellular processes such as mitosis and cell migration (Boppart, Bouma, Pitris, Southern, *et al*., 1998) [66].

4.7 Applications in engineering

Nevertheless OCT has uncovered also many non-biological applications that have included the nondestructive evaluation of materials including polymers, ceramics, and coatings (*Duncan, Bashkansky, Reintjes*, 1998) [69]. *Duncan et al.* used an OCT system, with a 1.3μm source, to image defects in materials like ceramics, paints and coatings. In 2001 *Dunkers et al* [70], produced images of cracks in matrix composites and compared it with, X-rays, CT and laser scanning confocal microscopy images. OCT resolved the depth of the cracks that both other techniques failed to identify.

References

1. M. A. Duguay, J. W. Hansen, *Optical sampling of subnanosecond light pulses*. Applied Physics Letters, Vol. 13, 1968, pp178-180,

2. M. A. Duguay, A. T. Mattick, *Ultrahigh speed photography of picosecond light pulses and echoe,* Applied Optics, Vol.10, 1971, pp2162-2170.

3. M. A Duguay , *Light photographed in flight*, American Science, Vol. 59, 1971, pp551-556.

4. K. Takada, I. Yokohama, K. Chida, J. Noda, *New measurement system for fault location in optical waveguide devices based in an interferometric technique*. Applied Optics, Vol. 26, 1987, pp1603-1606.

5. P.Healey, *Instrumentation principles for optical time domain reflectometry*. Journal of physics engineering and science instrumentation, Vol. 19, 1986, pp334-341.

6. R. C. Youngquist, S. Carr, D. E. N. Davies, *Optical coherence domain reflectometry: A new evaluation technique,* Optics Letters, Vol.12, 1987, pp158-160.

7. H. H. Gilgen, R. P. Novak, R. P. Salathe, W. Hodel, P. Beaud, *Sublimiter optical reflectometry*, IEE Journal of light wave technology, Vol. 7, 1989, pp1225-1233.

8. A. F. Fercher, K. Mengedoht, W. Werner, *Eye-length measurement by interferometry with partially coherent light*, Optics Letters, Vol. 13, 1988, pp1867-1869.

9. D. Huang, J. Wang, C. P. Lin, J. G. Pualiafito, *Micro-resolution ranging of cornea and anterior chanber by optical reflectometry*. Laser in surgery and medicine, Vol. 11, 1991, pp419-425.

10. http://www.myeyeworld.com [23/10/2007]

11. E. A. Swanson, J.A. Izatt, M. R. Hee, *In-Vivo Retinal Imaging Using Optical Coherence Tomography*, Optics letters, Vol. 18, 1993, pp1864-1866.

12. A. F. Fercher, C. K. Hitzenberger, W. Drexler, G. Kamp, H. Sattmann. *In vivo optical coherence tomography,* American Journal of ophthalmology, Vol. 116, 1993, pp113-114.

13. M. R. Hee, J.A. Izatt, E. A. Swanson, D. Huang, C. P. Lin, J. S. Schuman, C. A. Puliafito, J. G. Fujimoto, *Optical coherence tomography of the human retina*, Arch. Ophthalmology, Vol. 113, 1995, pp 325–332.

14. Schuman JS, Hee MR, Pualifito CA, Wong C, Pedut-Kloizman T, Lin CP, Hertzmark E, Izaat JA, Swanson EA, Fujimoto JG. *Quantification of nerve fibre layer thickness in normal and glaucomatous eyes using optical coherence tomography*, Arch Ophthalmology, Vol.113, 1995, pp586-596.

15. Puliafito, C.A. Hee MR, Lin CP, Reichel A, Schuman JS, Duker JS, Izaat JA, Swanson EA, Fujimoto JG, *Imaging of macular disease with optical coherence tomography (OCT)*, Journal of ophthalmology, 1995, pp217-229.

16. Williams ZY, Schuman JS, Camell L, Nemi A, Hertzmark E, Fujimoto JG, Matox C, Simpson J, Wollstein G., *Optical coherence tomography measurement of nerve fibre layer thickness and the likelihood of visual field defect*, American journal of ophthalmology, Vol. 134, 2002, pp538-546.

17. Hee MR, Puliafito, C.A. Lin CP, Reichel A, Schuman JS, Duker JS, Swanson EA, Fujimoto JG, *Optical coherence tomography for macular holes,* Ophthalmology, Vol. 102, 1995, pp748-756

18. Hee M, Izatt J, Swanson E. *Optical coherence tomography for ophthalmic imaging: New technique delivers micron-scale resolution*. IEEE in medicine and biology, Vol. 113, 1995, pp67-76

19. Ko TH, Witkin AJ, Fujimoto JG, *Ultrahigh-resolution optical coherence tomography of surgically closed macular holes*. Arch Ophthalmology, Vol.124, 2006, pp827-836.

20. Hee MR, Puliafito, C.A. Lin CP, Reichel A, Schuman JS, Duker JS, Swanson EA, Fujimoto JG, *Quantitive assessment of macular edema with optical coherence tomography (OCT)*, Arch Ophthalmology, Vol. 113, 1995, pp1019-1029.

21. Hee MR, Baumal C. R., Puliafito, C.A., Reichel A, Schuman JS, Duker JS, Swanson EA, Fujimoto JG, *Optical coherence tomography of age related macular degeneration and choroidal neovascularisation,* Ophthalmology, Vol. 103, 1996, pp1260-1270

22. Polito A, Shah SM, Haller JA, Zimmer-Galler I, Zeimer R, Campochiaro PA, Vitale S. *Comparison between retinal thickness analyzer and optical coherence tomography for assessment of foveal thickness in eyes with macular disease.* American journal of ophthalmology, Vol. 134, Issue 2, 2002, pp 240-251.

23. Schuman JS, Hee MR, Pualifito CA, Wong C, Pedut-Kloizman T, Lin CP, Hertzmark E, Izaat JA, Swanson EA, Fujimoto JG. *Quantification of nerve fibre layer thickness in normal and glaucomatous eyes using optical coherence tomography*, Arch Ophthalmology, Vol. 113, 1995, pp586-596.

24. Scuman JS, Hee MR, Arya AV, Pedut-Kloizman T, Pualifito CA, Fujimoto JG, Swanson EA. *Optical coherence tomography: A new tool for glaucoma diagnosis*. Curr. Opin. Ophthalmology, Vol. 6, 1995, pp89-95.

25. Schuman JS, Noecker RJ. *Imaging of the optic nerve head and nerve fibre layer in glaucoma*, Clinical ophthalmology of North America, Vol. 8, 1995, pp259-279.

26. Schuman JS, Pedut-Kloizman T, Hertzmark E, Hee MR, Wilkins JR, Coker JG, Pualifito CA, Fujimoto JG, Swanson EA. *Reproducibility of nerve fibre layer thickness measurements using optical coherence tomography*, Ophthalmology, Vol. 103, 1996, pp1889-1898.

27. Schaudig U, Hassenstein A, Bernd A, Walter A, Richard G., *Limitations of imaging choroidal tumors in vivo by optical coherence tomography*. Graefe's Arch. Clin. Exp. Ophthalmology, Vol. 236, 1998, pp588-592.

28. Rollins, A.M., Sivak, M.V., Radhakrishnan, S., Lass, J.H., Huang, D., Cooper, K.D. Izatt, J.A., *Emerging clinical applications of optical coherence tomography*. Optics and Photonics News, Optical Society of America, 2002

29. Toth CA, Narayan DG, Boppart SA, Hee MR, Fujimoto JG, Bringruber R, Cain CP, DiCarlo CD, Roach WP. *Argon laser retina lesions evaluated in vivo by optical coherence tomography.* American journal of ophthalmology, Vol. 123, 1997, pp188-198.

30. Drexler W, Morgner U, Kartner FX. *In-Vivo Ultra-Hiigh Resolution Optical Coherence Tomography*. Optics letters, Vol. 24, 2001, pp1221-1223.

31. Bowd C, Zangwill LM, Berry CC, Blumenthal EZ, Vasile C, Sanchez-Galeana C, Bosworth CF, Sample PA, Weinreb RN., *Detecting early glaucoma by assessment of retinal nerve fibre layer thickness and visual function*, Investigative ophthalmology & visual science, Vol. 42, 2001,pp1993-2003.

32. Williams ZY, Schuman JS, Camell L, Nemi A, Hertzmark E, Fujimoto JG, Matox C, Simpson J, Wollstein G. *Optical coherence tomography measurement of nerve fibre layer thickness and the likelihood of visual field defect.* American journal of ophthalmology, Vol. 134, 2002, pp538-546.

33. Krivoy D, Gentile R, Liebman JM, Stegman Z, Walsch JB,Ritch R. *Imaging congenital optic disc pits and associated maculopathy using optical coherence tomography*, Arch. Ophthalmology, Vol. 114, 1996, pp165-170.

34. Schmitt, J. M., Yadlowsky, M. J., & Bonner, R. F. *Subsurface imaging of living skin with optical coherence microscopy*. Dermatology, Vol. 191, 1995, pp 93–98.

35. Krishnaswamy A. Baranoski, *A study on the skin optics,* G.V.G. 2004.

36. http://www.infovisual.info [19/06/2006]

37. Boppart S.A., Bouma B.E., Pitris C., Brezinski J.F., Fujimoto J.G., *Intraoperative assessment of microsurgery with 3D OCT,* Radilogy, Vol. 208, 1998, pp81-86

38. University of Vienna, OCT group website: http://www.univie.ac.at/?L=2 [02/04/2007]

39. Boppart, S. A., Brezinski, M. E., Pitris, C., & Fujimoto, J. G. *Optical coherence tomography for neurosurgical imaging of intracortical melanoma*. Neurosurgery, Vol. 43, 1998, pp 834–841.

40. Boppart, S. A., Brezinski,M. E., Bouma, B. E., Tearney,G. J.,&Fujimoto, J. G. *Investigation of developing embryonic morphology using optical coherence tomography*. Developmental Biology, Vol.177, 1996, pp 54–63.

41. Machtei E. E., Christersson L. A., *Alternative methods for screening periodontal disease in adults,* Journal of clinical periodontology, Vol. 20, 1993, pp81-87

42. Everett M. J., Colston B. W. Jr, Sathyam U. S., Da Silva L. B., Fried D., Featherstone J. D., *Non-inasive diagnosis of early carries with polarisation sensitive optical coherence tomography,* SPIE proceedings lasers in dentistry V, 1999:3593.

43. Cvar J. F., Ryge G., *Criteria for the clinical evaluation of dental restoration materials,* San Fransisco: US- Department HEW PHS, dental health centre, 1971.

44. http://www.lantislaser.com [10/07/2007]

45. Brezinski, M. E., Tearney, G. J., Weissman, N. J., Boppart, S. A., Bouma, B. E., Hee, M. R., Weyman, A. E., Swanson, E. A., Southern, J. F., & Fujimoto, J. G., *Assessing atherosclerotic plaque morphology: Comparison of optical coherence tomography and high frequency intravascular ultrasound.* British Heart Journal, Vol.77, 1997, pp 397–404.

46. Brezinski M. E, Tearney G. J, Weissman N. J., Boppart S. A., Bouma B. E., Hee M. R., Weyman A. E., Swanson E. A, Southern JF, Fujimoto JG. *Optical coherence tomography for optical biopsy: Properties and demonstration of vascular pathology*. Circulation. 93:1206-1213,1996.

47. American Heart Association (AHA), *Heart and stroke facts, statistical supplement*, 1996, Dallas.

48. Falk. E., *Plaques rupture with severe pre existing stenosis precipitating coronary thrombosis, characteristics of coronary atherosclerotic plaques underlying fatal occlusive thrombi,* British heart journal, Vol. 50, 1983, pp127-134.

49. Fuster V. L. Badimon L., Badimon J. J., *The pathogenesis of coronary artery disease and acute coronary syndromes,* New England journal of medicine, Vol. 326, 1992, pp242-249.

50. Davies M. J., Thomas A.C., *Plaque fissuring: The cause of acute myocardial infraction, sudden ischemic death, and crescendo angina,* British heart journal, Vol. 53, 1983, pp363-373

51. http://www.vascularweb.org [27/07/2005]

52. Brezinski M. E., Tearney G. J., Boppart S. A., Bouma B. E., Hee M. R., Weyman A. E., Swanson E. A., Fujimoto J.G., *Imaging of coronary artery microstructure (in-vitro) with optical coherence tomography,* American journal of cardiology, Vol. 77, 1996, 1206-1213.

53. Kawasaki M., Bouma B. E., Bressner J., Houser S. L., Nadkarni S. K.,. MacNeill B. D, Jang I. K., Fujiwara H., Tearney G. J., *Diagnostic Accuracy of Optical Coherence Tomography and Integrated Backscatter Intravascular Ultrasound Images for Tissue Characterization of Human Coronary Plaques,* Journal of American Coll. Cardiology, Vol. 48, 2006, pp81-88.

54. Rallan D., Harland C. C., Blackwell Publishing Ltd, *Clinical and Experimental Dermatology*, Vol. 29, 2004, pp 453–459.

55. Nicholas Aspres, Ian B Egerton, Adrian C Limand, Stephen P Shumack, *Australasian Journal of Dermatology,* Vol. 44, 2003, pp 19–27.

56. Wagner A., Ploder O., Enislidis G., Truppe M., *Image guided surgery,* International journal of oral maxilofac surgery, Vol. 25, 1996, pp147-151.

57. Siesseger M., Mischokowski A., Schneider T., Krug B.,Klesper B., Zoler J. E., *image guided surgical navigation for the removal of foreign bodies,* Journal of craniomaxilofac surgery, Vol. 29, 2001, pp321-325

58. Izatt, J.A.,Kulkarni, M.D.,Wang,H.-W.,Kobayashi,K., Sivak,M. V. *Optical coherence tomography and microscopy in gastrointestinal tissues*. IEEE Journal of Selected Topics in Quantum Electronics, Vol. 2, 1996,pp1017–1028

59. Tearney,G. J., Brezinski,M. E., Southern, J. F., Bouma, B.E., Boppart, S.A.,& Fujimoto, J. G. *Optical biopsy in human gastrointestinal tissue using optical coherence tomography*. American Journal of Gastroenterology, Vol. 92, 1997, pp1800–1804.

60. Kobayashi R. Izaat J. A., Rulkarni M. D., Willis J., Sivak M. V., *High resolution cross sectional imaging of the gastrointestinal using optical coherence tomography,* Gastrointestinal endoscope, Vol. 47, 1998, pp.515-523.

61. Evans J. , Poneros J. , Bouma B. E. , Bressner J. , Halpern E. , . Shishkov M., Lauwers G., Mino–Kenudson M ., Nishioka N ., Tearney G ., *Optical Coherence Tomography to identify intramucosal carcinoma and high-grade dysplasia in Barrett's esophagus* . Clinical Gastroenterology and Hepatology, Vol. 4 , Issue 1 , 2006, pp38 – 43.

62. Chen Y., Aguirre A. D., Hsiung P. L., Huang S. W., Mashimo H., Schmitt J. M., Fujimoto J. G., *Effects of axial resolution improvement on optical coherence tomography (OCT) imaging of gastrointestinal tissues,* Optics Express, Vol. 16, No. 4,2008 pp2469-2485

63. Rollins, A.M., Sivak, M.V., Radhakrishnan, S., Lass, J.H., Huang, D., Cooper, K.D. Izatt, J.A., *Emerging clinical applications of optical coherence tomography.* Optics and photonics news 2002, Optical Society of America.

64. Boppart, S. A., Brezinski, M. E., Tearney, G. J., Bouma, B. E., Fujimoto, J. G. *Imaging developing neuralmorphology using optical coherence tomography.* Journal of Neuroscience Methods*,* Vol. 2112, 1996, pp65–72.

65. Boppart, S. A., Tearney, G. J., Bouma, B. E., Southern, J. F., Brezinski, M. E., Fujimoto, J. G. *Noninvasive assessment of the developing Xenopus cardiovascular system using optical coherence tomography*. Proceedings of the National Academy of Sciences, USA, Vol.94, 1997, pp4256–4261.

66. Rollins, A. M., Kulkarni, M. D., Yazdanfar, S., Ung-arunyawee, R., Izatt, J. A. *In vivo video rate optical coherence tomography*. Optics Express, Vol. 3, 1998, pp219–229.

67. Boppart S. A., Brezinski M. E., Tearney G. J., Bouma B. E., Fujimoto J. G., *Investigation of developing embryonic morphology using optical coherence tomography,* Developmental biology, Vol. 177, 1996, pp54-63.

68. http://www. thorlabs.com [17/04/2008]

69. Duncan, M.D., Bashkansky, M., *Subsurface defect detection in materials using optical coherence tomography.* Optics Express, Vol. 2, 1998, pp540-545.

70. Dunkers, J. P., Phelan, F. R., Sanders, D. P., Everett, M. J., Green, W. H., Hunston, D. L. Parnas, R. S., *The application of optical coherence tomography to problems in polymer matrix composites*. Optics and Lasers in Engineering Vol. 35, 2001, pp135-147.

Chapter 5

OCT INSTRUMENTATION REVIEW

5. Optical Sources

Since the first demonstration of OCT with an SLD (Superluminescent Laser Diode), different sources have been used through out the years that followed, in order to increase the imaging capabilities of OCT. The wavelength of the source to be use in OCT must be carefully chosen for each application. Generally when choosing a source seven primary criteria must be considered:

1. Wavelength
2. Bandwidth
3. Single transverse mode power
4. Stability
5. Portability
6. Compatibility with the application environment
7. Cost

OCT systems that use optical sources at longer wavelengths have enabled deeper tissue (non-transparent tissue) imaging in highly scattering soft tissues. As Brezinski *et al.*, demonstrated in 1996 [1] using 1300nm wavelengths, 2mm penetration depth could be achieved. Figure 5.1 shows the influence of median wavelength on penetration while images were taken from a human epiglottis at two wavelengths (850 and 1300 nm) and compared with histology. At 850 nm, most of the data is obtained at the surface of the sample. At 1300 nm, structural detail is identified deeper within the tissue, with the underlying cartilage clearly identified. The bar in all images represents 500 μm unless indicated.

a)

b)

c)

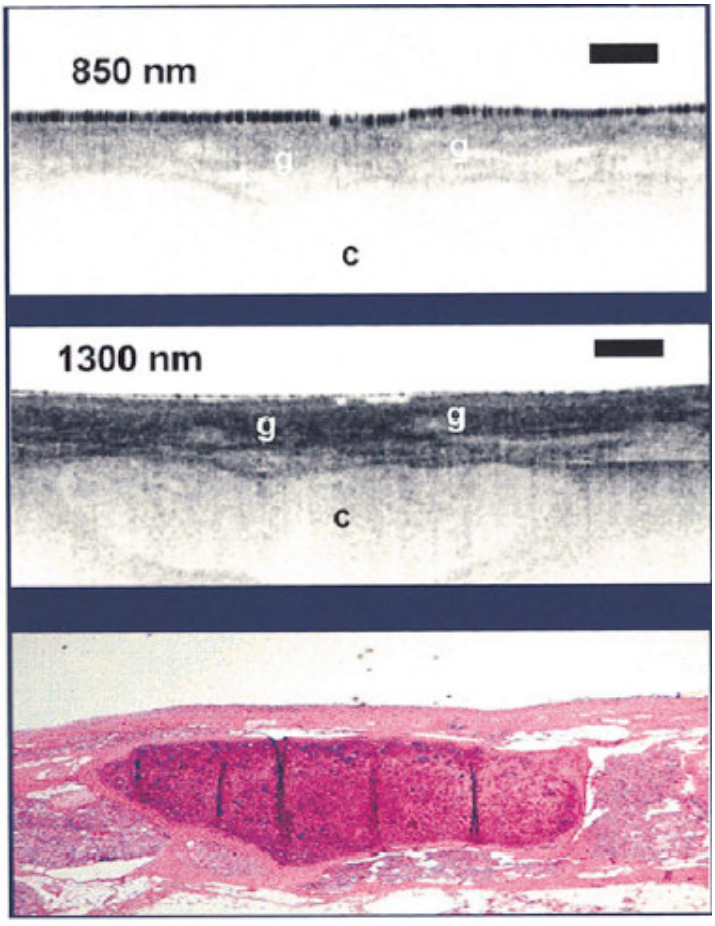

Figure 5.1: Influence of median wavelength on penetration [1].
a)OCT image of human epiglottis performed at 850nm
b)OCT image of human epiglottis performed at 1300nm
c)Histology (c, g parts of human epiglottis)

Tissue is a turbid medium, characterized by many small random fluctuations in refractive index caused by the ultrastructure of the tissue, i.e., by cells and organelles [2]. As a consequence of these refractive index fluctuations, light is incident on tissue is deflected or scattered off these particles. Additionally, tissue also contains chromophores, molecules that can absorb incoming photons [3]. Because these scattering particles and chromophores are complexly distributed in the tissue, describing the interaction between light and tissue can be a rather laborious task. So choosing the right wavelength to achieve acceptable penetration depth and resolution would be a dilemma but according to the early research the best choice would be the red end of the visible spectrum that is also known as the diagnostic or therapeutic window, because it is the location of a relative minimum in the absorption of typical tissue constituents such as water and blood [1]. (See Figure 5.2)

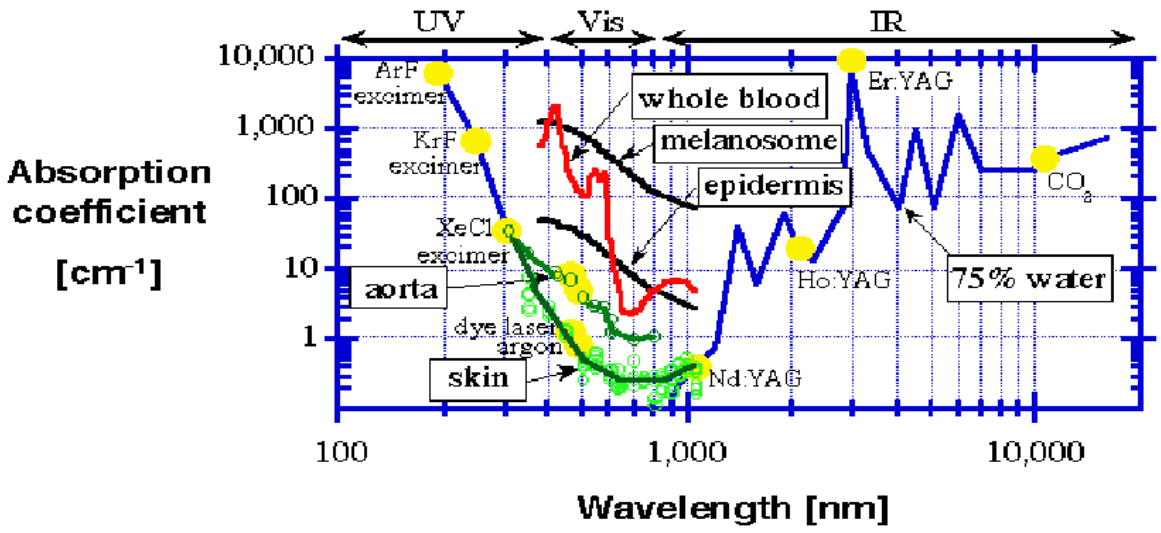

Figure 5.2: Absorption vs. Wavelength [4]

Thus shorter wavelengths are more highly scattered in biological tissue, resulting in less imaging penetration. In the near-infrared, roughly between 800nm and 1500 nm, light attenuation is more dependent on scattering processes than on absorption processes and at wavelengths below 800 nm, absorption by hemoglobin and melanin dominates light attenuation and at wavelengths above 1500 nm, light attenuation is mainly due to absorption by water.

5.1 Kerr-Lens Mode-Locked (KLM) Lasers

Mode locking is the amplitude modulation of a laser beam in the optical cavity at the laser resonator optical frequency. At this state each mode includes symmetrical side bands that interact with neighbouring modes [5, 6]. As there is constant relationship between a mode and its individual side band this effect produces a phase and amplitude locking of the mode producing a series of short pulses. A general schematic of a KLM Ti:Al_2O_3 is shown in figure 5.3.

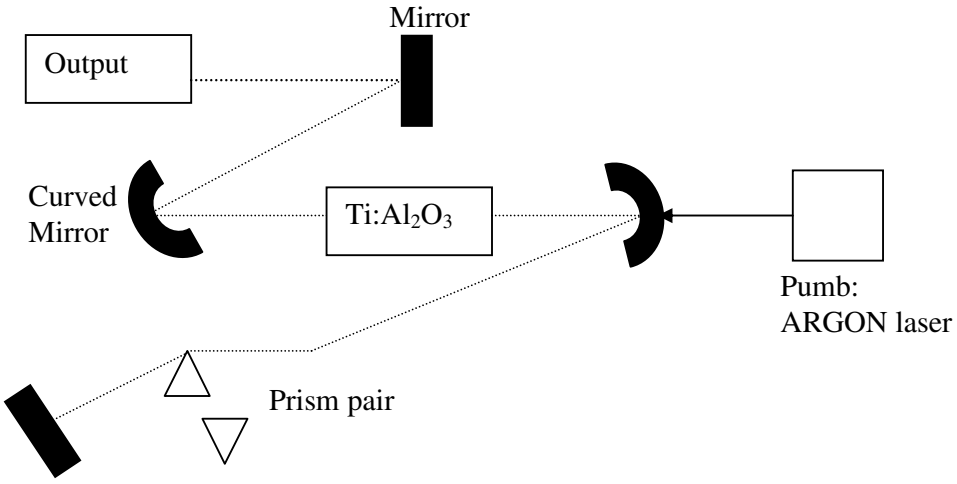

Figure 5.3: KLM Ti:Al_2O_3 laser set-up.

The Ti:Al_2O_3 is pumped by a continuous wave argon laser (514μm) within a reonator. The prism pair controls the dispersion within the laser cavity by allowing shorter or longer path lengths through the dispersive glass.

Kerr lens mode-locked (KLM) Ti:Al_2O_3 lasers can generate extremely short pulse durations with broad bandwidths that are particularly useful in biomedical imaging [7-9]. Recently, OCT imaging with an axial resolution of ~1 μm has been demonstrated using a Ti:Al_2O_3 laser with a bandwidth of ~300 nm.[10] This source produced a pulse durations of ~5 fs, which correspond to approximately two optical

cycles [11]. A standard Kerr lens mode-locked laser operating with a 5W pump can produce output powers of 500 mW and bandwidths in excess of 150 nm [12]. In ophthalmology, ultrahigh resolution OCT imaging with axial resolutions of 2-3 µm has been shown to significantly improve the visualization of retinal morphology [10, 13] and retinal pathologic changes [11, 15-18]. Figure 5.4 shows a comparison between images of a normal human fovea using standard SLD source based OCT (axial resolution ~13µm transverse ~15µm) and an ultrahigh resolution Ti:Al_2O_3 laser (axial resolution ~3µm transverse ~14µm)

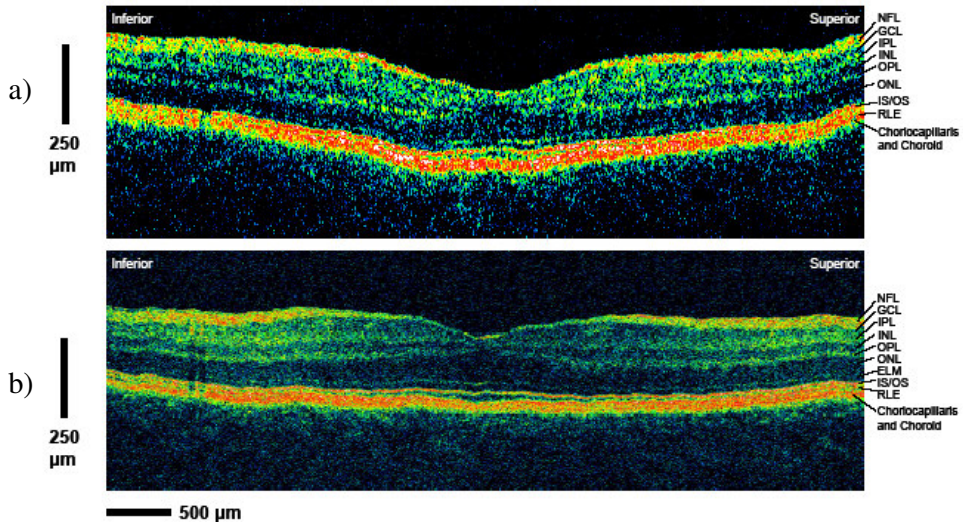

Figure 5.4: OCT images of a normal human fovea a) with SLD source based OCT b) with Ti:Al_2O_3 laser based OCT [10]

However, ultrahigh resolution systems using these type sources are expensive and complex, limiting their widespread use. The cost of a femtosecond Ti:Al_2O_3 lasers is strongly dependent on the pump power requirements. Diode pumped solid-state lasers capable of generating 5W can be prohibitively expensive, while lasers generating several hundred mW are considerably more affordable.

Another crystal that has also been investigated as possible source is the KLM Cr^{4+}:fosterite laser [18, 19]. This type of laser the Cr^{4+}:fosterite oscillator can be pumped with a continuous wave Nd:YAG laser. Reported Cr^{4+}:fosterite lasers

achieved spectral bandwidths greater than 200 nm at a centre wavelength of 1250 nm with an output power of 50 mW [20, 21].

Other sources that were considered for OCT use fibre lasers. Rare-earth doped fibres are diode pumped resulting in fluorescence within the fibre, which in turn is amplified by spontaneous emission along the fibre length. Broad bandwidths are achieved by suppressing lasing by cleaving the fibre ends. Several doped fibres have been reported for these sources like: neodymium [22, 23], praseodymium [24], ytterbium [25] and thulium [26]. These sources reported wavelengths ranging from 1080nm for ytterbium and 1800nm for thulium with high average output powers ranging from 40-150mW.

Presently many high resolution OCT systems are based on a Swept-Source (SS) [27, 28]. Most of the commercial swept sources available operate around 1300nm wavelength with a scan ranges around 110-150nm, average power in range of 10mW with a scan rate around 20 kHz [29]. So instead of using a broadband source and varying the path length another way is to sweep the frequency of a narrow band, continuous wave light source and collect the time dependent interference signal. Figure 5.5 shows a schematic of a reported frequency swept laser [27]. The ring cavity consists of a fibre coupled semiconductor amplifier (SOA), two isolators, a piezoelectric transducer actuated fibre Fabry-Perot tunable filter (FFPTF), and an output coupler.

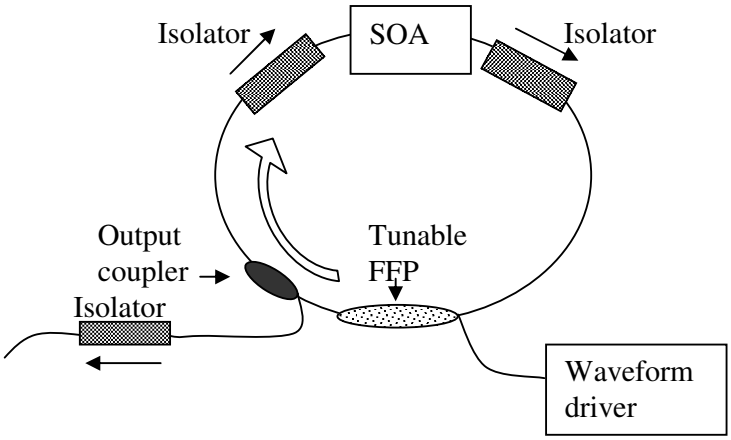

Figure 5.5: Schematic of a reported frequency swept laser source ring cavity.

The FFP-TF is used as a narrow-band transmission filter for active wavelength selection. The isolators in turn eliminate all extraneous intra-cavity reflections and ensure unidirectional lasing of the ring cavity. The high finesse of the FFP-TF provides narrow band spectral filtering suitable for achieving a sufficient dynamic coherence length of the source.

5.2 Scanning speed and Optical Delay Lines (O.D.L.)

In order to reduce the noise and artefacts produced in an OCT image due to the possible movements of the sample under test the OCT images must be acquired as quickly as possible (5 frames per second). It is also important for patient comfort to scan the area of interest as fast as possible.

Increasing axial and lateral scanning speeds are both important. However A-scans are acquired to improved the accuracy of the images and so the speeds of these scans are the limiting factor to the overall acquisition rate. The scanning methods or the optical delay lines (ODL) that have been reviewed in the use of the OCT system can be classified into four main categories:

1. ODLs that are based on linear translation of a mirror.[30]
2. ODLs that vary optical path length by rotational methods [31]
3. ODLs that are optical fibre stretchers.[32]
4. ODLs that are based on group delay generation using Fourier domain optical pulse shaping technology. [33-35]

The simplest method for varying the optical path of a reference arm is to mount a mirror onto a linear mechanical translation stage [30] which can be controlled to move axially.

Other techniques proposed the idea of varying the path length by rotating a glass cube [36]. In that configuration a glass cube is placed between the end of the fibre and a fixed reference mirror. The light beam is then reflected internally within the tube onto an external prism and this directs the beam back to the cube and the reference mirror. In 1998 [34] longitudinal scan speeds up to 176 ms^{-1} were achieved by using a rotating glass cube spinning at 427000 rpm driven by a high speed air turbine. Although high scanning speeds were achieved this set up requires a great deal of precision and the system requires high powers.

Another technique used to vary the path length in a fibre based OCT is the use a piezoelectric fibre stretcher [37]. A PZT actuator with an attached mirror can vary the path length when a voltage is applied to the PZT crystal allowing it to expand. The PZT actuators though have limited travel ranges of few tens of μm.

Another way of producing a scanning optical delay line for OCT is to control the phase of the optical field [33-35, 38-39]. The theory lies in the Fourier Transform property that a phase ramp in the frequency domain corresponds to a group delay in the time domain.

$$x(t-t_o) \overset{FT}{\longleftrightarrow} X(\omega)\, e^{-j\omega t} \tag{5.1}$$

Since the original spectrum X(ω) is shifted in phase by $-j\omega t$ the function in time will be delayed by t_o. In general the RSOD (Rapid Scanning Optical Delay) line consists of three main components:

1. **A Grating lens pair**
2. **A Lens**
3. **Galvanometer**

As shown in figure 5.6 the grating diffracts the light into a number of diffraction orders. The first order contains a large portion of the light but higher orders offer larger group delay. Most demonstrated configurations though are using the first order.

By the means of the lens a Fourier transform occurs at the focal plane where a galvanometer or a tilting mirror is inserted. The lens is placed at the focal plane and it collimates different components of the diffracted light to produce a Fourier transform at the focal plane where a galvanometer is placed that is rotated linearly to produce a group delay which is expressed by:

$$_{g}(\gamma)=2\frac{f\lambda_o\gamma}{d\cos(\theta_o)}$$

f: focal length of the lens

γ: the angle created by the galvanometer

θ_o: output angle of the light

θ_i: input angle of the light

d:is the distance between two groves

λ_o: is the considered wavelength

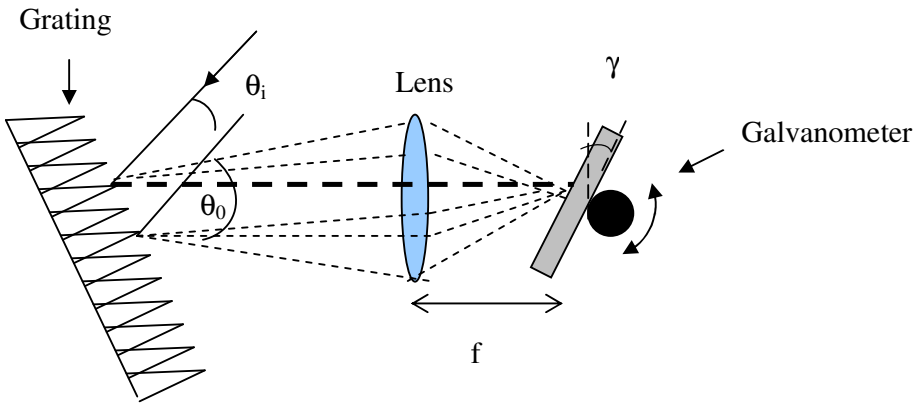

Figure 5.6: General schematic of a Fourier domain optical delay line, f:focal length of the lens, θ_o:output angle of the light, θ_i:input angle of the light,γ:angle created by the galvanometer.

The light is then redirected back through the lens, which re-collimates and re-converges the spectrum onto the grating where an inverse FT occurs. This method has achieved speeds up to 40mm/sec with A-scan repetition rates of 4kHz. [38]

5.3 Time Domain OCT

Generally there are two types of OCT. One is the time domain OCT (TD-OCT) , where is a single longitudinal scattering profile is obtained by translating the reference mirror. Both the depth and transversal directions have to be mechanically scanned to produce a two-dimensional cross-section map of the sample under test [40]. Although the most common configuration for this type of OCT is a standard Michelson interferometer other configurations or other versions of Michelson suitable for OCT have also been researched [40]. As the DC signal and intensity noise in a Michelson interferometer from the reference arm adds to the interference signal a balanced detection scheme has also been researched. The balanced detection is believed to cancel the background noise components by subtracting the photocurrents generated by the two detectors. A possible implementation is shown in figure 5.7.

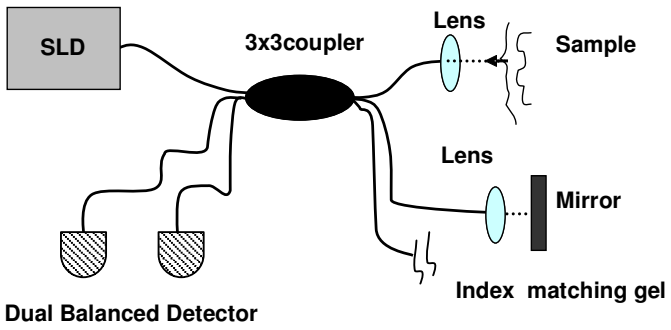

Figure 5.7: Michelson time domain OCT with balanced detection [40]

The other type of OCT is a Fourier Domain OCT (FD OCT) which is an alternative to TD OCT and provides high speed and high sensitivity [41].

5.4 Frequency (Fourier) domain OCT

Recently, new techniques for OCT, known as frequency or Fourier domain optical coherence tomography (FD-OCT) have been investigated [42, 43]. Fourier domain OCT has been demonstrated to provide higher acquisition speed and better signal to noise ratio than OCT with time domain detection [44]. In such a system the depth information in the signal is extracted by measuring the interference spectrum of the signal from the sample, and calculating a Fourier-transform from the acquired spectrum, without movement of the reference arm [45]. As mechanical scanning is no longer required for depth scans the imaging speed is increased dramatically, while reducing the losses during a single scan and improving the signal to noise proportional to the number of detection elements. Fourier domain OCT detection can be performed in two ways:

1. One way is to use a broad spectrum light source where the output of the interferometer is measured with a spectrometer and a high speed CCD array or linescan camera. This method is called Spectral Domain OCT (SD-OCT).

2. Another way is to sweep the frequency of a narrow band, continuous wave light source and collect the time dependent interference signal [46-48]. This method is called Swept Source OCT (SS-OCT).

Spectral OCT and swept source OCT have been used for ophthalmic imaging in the anterior eye and retina and have demonstrated ultrahigh-resolution imaging and high speeds when compared to TD-OCT [49]. However, the 1.3 wavelength swept source used for these investigations is not the most suitable for retinal imaging as the water absorption of 1.3 μm light is 38 times greater than that of 830-nm light [50]. Since water absorption has a local minimum at 1.06 μm, a source centred on 1μm would be the most appropriate for high penetration retinal OCT.

5.4.1 Spectral Domain OCT (SD-OCT)

A spectral-domain OCT (SD-OCT) was proposed by *Fercher et al.* in 1995 [51], and *Häusler et al.* in 1998 [7]. In the years that followed several groups demonstrated such a system for different applications [52-55].

The principle of this technique rests in optically dispersing the interferometric signal with a spectrometer. The spectral components are sampled with a linear detector array (line-array CCD or CMOS) and the spectral information are extracted by distributing different optical frequencies onto these detector arrays via a dispersive element like a grating as seen in figure 5.8. As there are no time-varying parameters, the optical output is constant and is integrated over the exposure time. The CCD array samples a series of spectral bins, which are equally spaced in wavenumber and the axial image is recovered by performing a digital Fourier transform of the spectrometer output. Thereby the information of the full depth scan can be acquired within a single exposure.

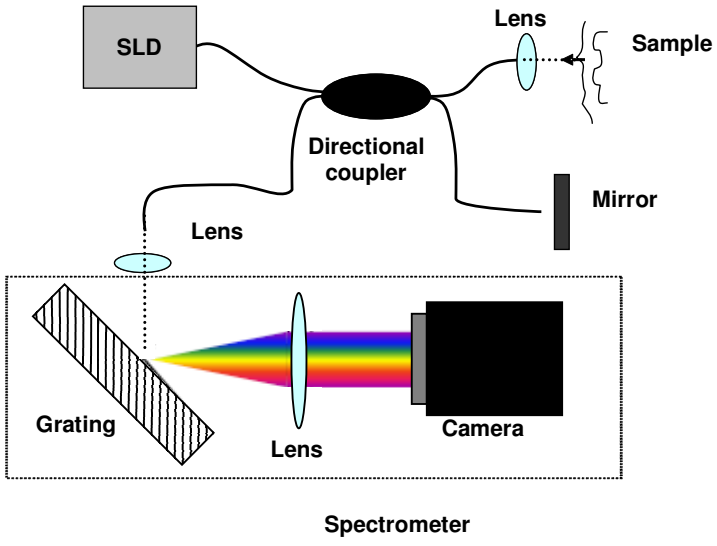

Figure 5.8: Michelson type SD-OCT

The key advantage of SD-OCT is that the N detector signals are added coherently, while the noise components are summed incoherently. This generates an improvement of SNR which is proportional to number of detectors and depends on the relative bandwidth of an individual detector. However, the large signal to noise advantage of SD-OCT is reduced due the lower dynamic range of the array detectors (CCD, CMOS) resulting in an SNR advantage of ~10 dB at much higher speeds [56].

5.4.2 Swept Source OCT (SS-OCT)

With this technique the spectral components are not encoded by spatial separation, but they are encoded in time. The frequency of a narrow band, continuous wave light source is swept and the spectrum is either filtered or generated in single successive frequency steps and reconstructed before Fourier-transformation. The advantage of this technique is the proven high SNR, while swept laser source achieve very small instantaneous bandwidths at very high frequencies ranging from 10-20 kHz. Comparison of the SNR for SS-OCT, SD-OCT and TD-OCT was reported by *Choma et al.* [53]. A possible implementation of SS-OCT is shown in figure 5.9.

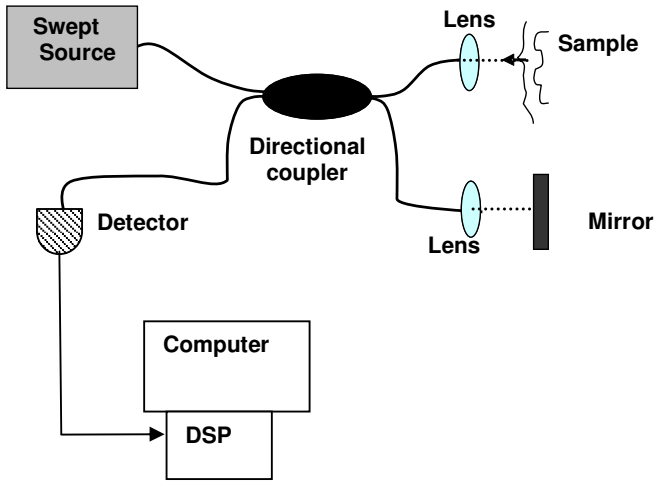

Figure 5.9: Single detector Michelson type SS-OCT, DSP:digital signal processing

The detection scheme of an SS-OCT system is more attractive when compared with SD-OCT as it is simpler, lower cost and high performance spectrometer and CCD camera are not required. One more advantage is that dual detection can be used in an SS-OCT system that could potentially enable superior performance (cancellation of excess noise) when compared to SD-OCT. Both these methods still have an increased cost when compared to a TD-OCT. Drawbacks are the nonlinearities in the wavelength, especially at high scanning frequencies. A common path swept-source OCT system has recently been presented by *S. Vergnole et. al* in 2008 [57].

5.5 Polarisation Sensitive OCT (PS-OCT)

The alteration of the polarisation properties of light was first explored as an alternative contrast mechanism in OCT in 1992 [58]. Since 1997 though [59], there has been a rapid escalation in researching this activity. Recent reviews have comprehensively discussed both the technology and its application [60, 61].

Because of the incredibly rich phenomenology associated with polarisation, recent advances in OCT technology, and the importance of potential applications, this area is one of the most exciting and challenging in OCT research. PS-OCT is sensitive to the birefringence (dependence of the phase velocity on polarisation) and dichroism (dependence of the amplitude on polarisation) of the sample, as well as to the polarisation dependence of scattering. The magnitude and orientation of birefringence has occupied most attention to date, dichroism is expected to be of little importance, and the effect of scattering has been little investigated and is relatively poorly understood.

Birefringence in tissue [58] can be intrinsic, caused by anisotropy at the molecular level, for example, hydroxyapatite crystals in dental enamel, or it can be caused by form, the ordered layering of anisotropic structures on a scale large compared with the optical wavelength. Examples of this latter type include the cornea, muscles, nerves, tendons, cartilage, bones, and teeth. In such structures, the spatially-

resolved magnitude and orientation of the birefringence is an alternative contrast mechanism to standard OCT, providing alternative structural information which can be linked to the function and status of tissue.

The effect of scattering on polarisation is a complicating factor that has also been employed in a practical way in PS-OCT to a limited extent [61, 62]. The polarisation of light is altered at each single scattering event, depending in a complex way on the state of polarisation, scatterer size, shape, strength and the scattering angle [62, 63]. OCT seeks to discriminate single backscattering. Exactly 180-degree backscattering of linearly-polarised light from a spherical particle leaves the polarisation state unchanged, but if the input state at the scatterer is not linear, or if the scatterer is not spherical in shape, then the output polarisation state is altered. For example, the handedness of circularly-polarised light is reversed by backscattering. The effects of scattering in PS-OCT are manifested potentially in two ways:

1. effect is caused by scattering from the sample volume itself,
2. from the accumulation of polarisation changes due to multiple scattering.

In addition to rigorously characterize the polarisation properties of biological tissue, one should evaluate the 4×4 Müller matrix M, which connects the input Stokes vector S_{in} at some location r in the tissue to the output Stokes vector S_{out}, such that:

$$S_{out}(r)=M(r)S_{in}(r) \tag{5.2}$$

This approach though requires 16 independent measurements, one for each matrix element to obtain an image.

Such images could be used to determine the local birefringence and its orientation, although only values averaged over significant spatial regions have been presented to date [63]. Less complete information can be obtained by determining the output Stokes vector for a known input Stokes vector [63]. However, the need to determine only four independent parameters reduces the measurement time and data processing complexity. There has also been significant research into employing a

Jones matrix approach to analyse PS-OCT [58, 59]. If the degree of polarisation is everywhere unity then a Jones matrix approach is valid. A bulk optic PS-OCT is shown in figure 5.10.

Light from an SLD passes through a polariser, which selects a pure, linear, vertical input state. This is split 50/50 by a polarisation insensitive beam splitter into a reference and sample arm. Light in the reference arm passes through a Quarter Wave Plate (QWP) orientated at 22.5° to the incident polarisation. Following reflection from a reference mirror mounted on a translation stage the light emerges with a linear polarisation state 45° to the incident light. Light in the sample arm passes through a QWP orientated at 45° to the incident light so that circularly polarised light is incident on the tissue sample. After passing through the lens system and tissue sample the light is in an arbitrary polarisation state depending on the birefringence of the reflection site. The reference and sample beams recombine and are split into their horizontal (A_H) and vertical (A_V) polarised components of the interference intensity, by a polarising beam splitter.

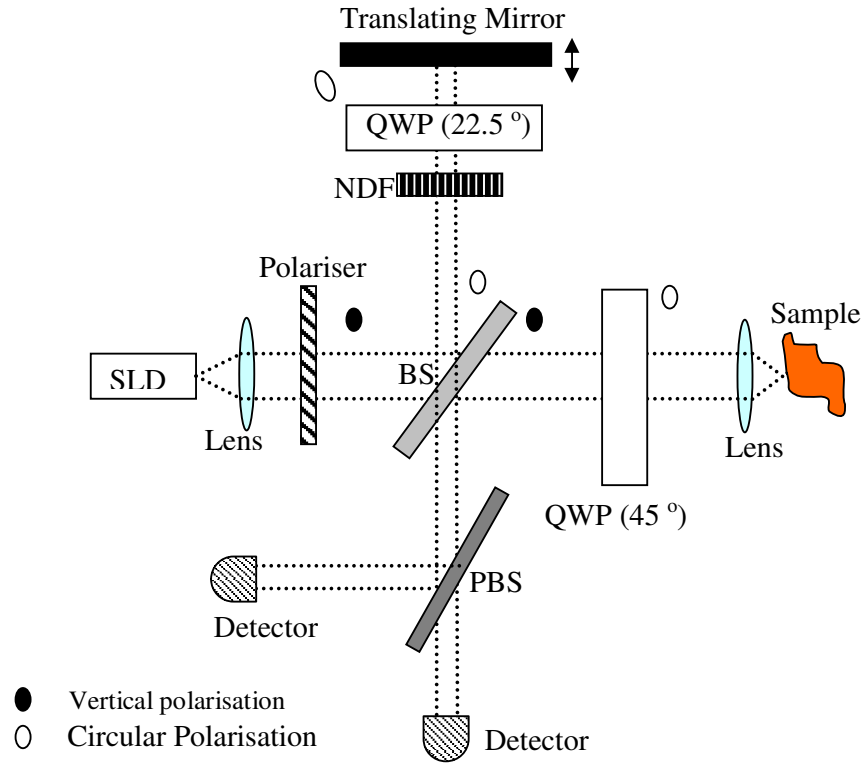

Figure 5.10: PS-OCT system; P; polarizer, NDF; neutral density filter, QWP: quarter wave plate, BS:beam splitter, PBS: polarisation sensitive beam splitter

The polarisation state from each reflection is then calculated using the Jones matrix formalism: Equation 5.3 for horizontal component and equation 5.4 for vertical component.

$$\text{Horizontal: } A_H = \sqrt{R_{(z)}}\cos(2k_0\Delta z + 2\alpha)\exp-\left(\frac{\Omega\Delta z}{c}\right)^2 \sin(k_0 z\delta) \tag{5.3}$$

$$\text{Vertical: } A_V = \sqrt{R_{(z)}}\cos(2k_0\Delta z)\exp-\left(\frac{\Omega\Delta z}{c}\right)^2 \cos(k_0 z\delta) \tag{5.4}$$

Where Δz is the path length difference between the two interferometer arms,
z is the depth of the light reflected from the sample,
$R_{(z)}$ is the reflectivity at depth z,
c is the speed of light in a vacuum,
k_0 is the attenuation of the coherent beam by scattering,
δ is the tissue birefringence, given by the difference in refractive indices along the fast and slow axis of the sample $\delta=n_s-n_f$.
α is the angle of the fast optical axis measured with respect to the vertical
and Ω is given by:

$$\Omega = \frac{\Delta\lambda c}{\lambda_0^2\sqrt{\ln 2}} \tag{5.5}$$

Where:
$\Delta\lambda$ is bandwidth of the source,
λ_0 is the centre wavelength
and n_s and n_f are the refractive indices along the fast and slow axes of the tissue respectively.

From the vertical and horizontal components detected the carrier frequency $[\cos(2k_0\Delta z)]$ within the coherence envelope $e^{-(\frac{\Omega\Delta z}{c})^2}$ is filtered out leaving a signal oscillating as a function of birefringence and depth. Assigning a grey scale value to

the common log (I_s) of both polarisation channels (I_H and I_V), forms the PS-OCT images.

$$\log\left(I_{s(z)}\right) = \log\left(I_{H(z)} + I_{V(z)}\right) \tag{5.6}$$

$$I_{H(z)} = R_{(z)} \sin^2\left(k_0 z\delta\right) \tag{5.7}$$

$$I_{V(z)} = R_{(z)} \cos^2\left(k_0 z\delta\right) \tag{5.8}$$

The phase retardation as a function of depth is given by:

$$\phi = \arctan\sqrt{I_H(z)/I_V(z)} = k_0 z\delta \tag{5.9}$$

In 1992 *Hee et. al.* [58] reported the first OCT system that could record the changes in the polarisation state of light being reflected from the sample and they demonstrated a birefringence sensitive ranging in a wave plate, an electro-optic modulator, and measurements in a calf coronary artery.

In 1997 *de Boer, Milner et. al* demonstrated the first two dimensional images of bovine tendon and the affect of laser induced thermal damage on the birefrigence of collagen using a pulsed laser for irradiation [61]. Since the dominant structure in human skin is collagen its birefringence has two components. One is from birefringence resulting from ordered proteins surrounded by a ground substance with a different refractive index and two, intrinsic birefringence results from chemical groups arranged in an ordered configuration with anisotropic optical retardance. Now, thermal damage which starts to take place between 56^{o}C and 65^{o}C reduces both form and intrinsic birefrigence by changing the collagen from a rodlike to a random coil structure. [63] So this reduction of collagen birefringence could be recorded from PS-OCT and can be used to determine burn injury. The resulting images of fresh bovine tendon 1mm wide by 700mm deep that *de Boer et. al.* obtained are exhibited in figure 5.11. Each pixel represents a 10μm 310μm area and the dynamic range of his system was 48dB. Deep blue and deep red represent noise [59].

The following year *De Boer et. al*. continued research in the field of PS-OCT again to assess the temperature effect on collagen birefringence but this time instead of using a pulsed laser to irradiate the porcine tendon was mounted in a rose chamber filled with 5% saline solution and used a thermocouple to monitor the temperature inside the chamber [49]. He then placed a heating device outside the chamber that could increase the temperature inside to 77°C. Finally he observed the effect that temperature could have on the sample at different temperatures, 25°C, 45°C, 55°C. The same year a demonstration of the birefringence in porcine myocardium was also demonstrated [60].

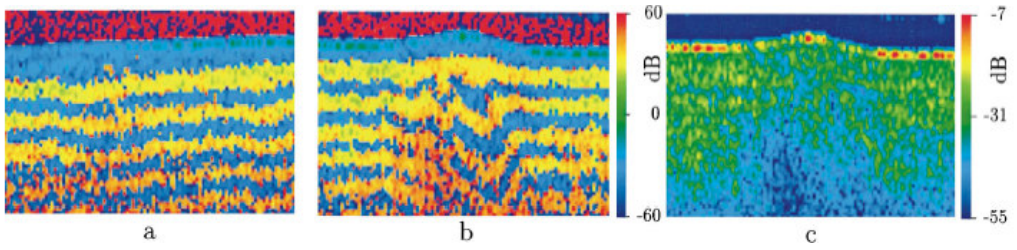

Figure 5.11: Images of fresh bovine tendon using PS-OCT [59]

a) Birefringence image of fresh bovine tendon.

b) Birefringence image of bovine tendon following exposure to three consecutive 1-J 150-ms laser pulses, spaced by 10 ms, incident from the upper left at 35°C with respect to the surface normal. The beam diameter was 2 mm. Initial surface temperatures after laser irradiation was 77 °C, dropping to 61 °C after 0.25 s.

c) Total backscattered intensity image of bovine tendon, constructed from the same measurement shown in b to demonstrate differences from the polarization-sensitive image [50].

In March 1999 *J.F de Boer et. al.* used the PS-OCT system to determine the Stokes parameters of backscattered light as a function of optical path in turbid media. To demonstrate the applications of this technique he determined the birefringence and optical axis in a fibrous tissue (rodent muscle) and in-vivo rodent skin [61]. This technique proved beneficial in biomedical optics because someone could simultaneously image the structural properties of turbid biological materials and their effects on the polarisation state of the backscattered light [62]. Later in this year PS-OCT was used to provide cross sectional images in the cornea and retina of rabbit

eyes [64] . In 1999 PS-OCT was also used to map the birefringence of skeletal muscle, bone, skin and brain tissue. [62]

In the years that followed a lot of research groups were investigating the potential applications of PS-OCT systems demonstrating different configuration for different applications. PS-OCT has also been applied to material characterisation and strain field mapping [64]. Furthermore a polarisation sensitive SD-OCT has been presented in 2002 by *Yasuno et al.*[65]

5.6 OCT endoscopes

Light based endoscopy appeared in the 1960's when fibre endoscopes [66] were made available. Such endoscopes were composed of a bundle of glass or optical fibres with imaging lenses glued onto the distal end and were used to transfer an image from the distal end to the proximal end. Alternatively other types of endoscopes deployed for image guidance during surgical procedures [67-69] employed CCD cameras (videoscopes) at the distal end of the fibre bundle.

The relative ease of generating high speed high resolution images from OCT systems prompted numerous efforts to implement OCT endoscopes. Some of the applications addressed were described in previous sections of this chapter. This section will aim to give an overview of the current OCT endoscopic technology.

Some important characteristics of an OCT probe intended for in-vivo imaging are:

- scanning range
- field of view
- speed
- flexibility
- size

Today's reported OCT probes can be divided into two main categories based on their scan modes:

1. side imaging probes [70-79]
2. forward imaging probes [80-90]

5.6.1 Side imaging OCT probes

The majority of endoscopic probes reported in the literature are side imaging and this section of the thesis will report a couple of them. The first side imaging OCT probe was reported in 1996 [70]. A schematic of this probe is shown in figure 5.12, the rotation was achieved by attaching the proximal end of the flexible probe to a motor and a gear system. At the distal end the beam emanating from the optical source was focused with a GRIN lens attached to an optical fibre and then reflected by a right angle prism.

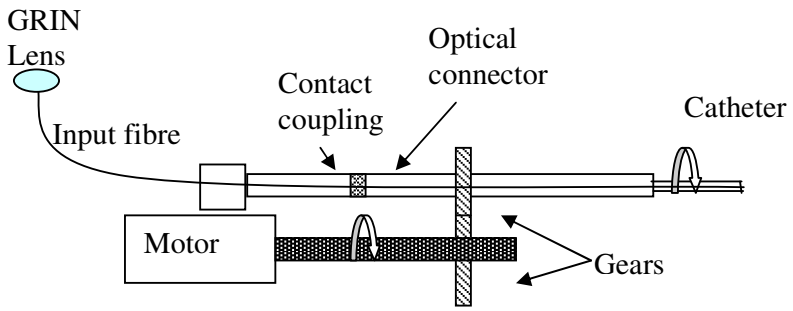

Figure 5.12: First side imaging OCT probe

Later in 2000 a similar but smaller side imaging OCT probe was reported by *Yang et. al.*[73]. In 2006 a longitudinal scanning endoscope was reported that housed an interferometer at the tip of the probe. Through out the years that followed several

side imaging OCT probes were reported. A comparison for those probes is illustrated in table.5.1

Table 5. 1: Reported side imaging OCT probes.

Year	Size (mm)	Axial Resolution (μm)	Lateral Resolution (μm)	Working Distance (mm)	Angular or Lateral scan range	Speed
1996[71]	1.1	20	38	~2.5	360^o	1rpm
1999[76]	N/A	9.3	30	0.7	5.5mm	1700A-scans/sec
2000[72]	0.4	6.7	17	0.08	360^o	N/A
2003[78]	2	~13	N/A	N/A	2mm	8000A-scans/sec
2004[74]	2.4	9.5	13	2	360^o	1000A-scans/sec
2004[75]	5	5	8	variable	360^o	2000A-scans/sec
2004[77]	1.5	5	1.5	0.5	35mm	3125A-scans/sec
2004[79]	2	16	18	0.3	6mm	14A-scans/sec
2005[73]	0.9	~13	~26	~0.35	2.5	4800A-scans/sec
2006[80]	2	2.4	10	0.3	>2.5mm	20000A-scans/sec

5.6.2 Forward imaging OCT probes

Forward imaging OCT probes are used to provide tissue structural information forward of a catheter probe for image guidance during surgery. The first probe of that kind was reported in 1997[81] by *Boppart et. al.* where an 6.4 mm PZT cantilever based handheld forward imaging instrument was used in open field surgery. The PZT was used to translate the fibre and a GRIN lens together for output scanning. A schematic is shown in figure 5.13.

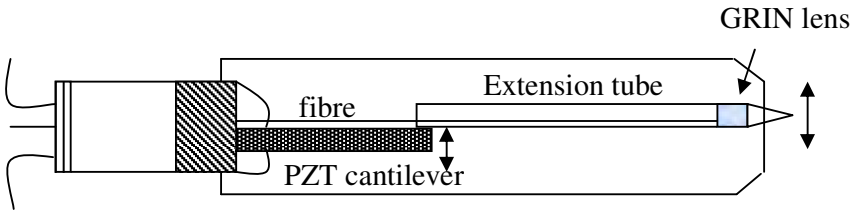

Figure 5.13: First forward imaging probe

Up to date, only one OCT system is reported using a fibre imaging bundles for forward imaging probes [90]. Figure 5.14 below depicts the configuration used.

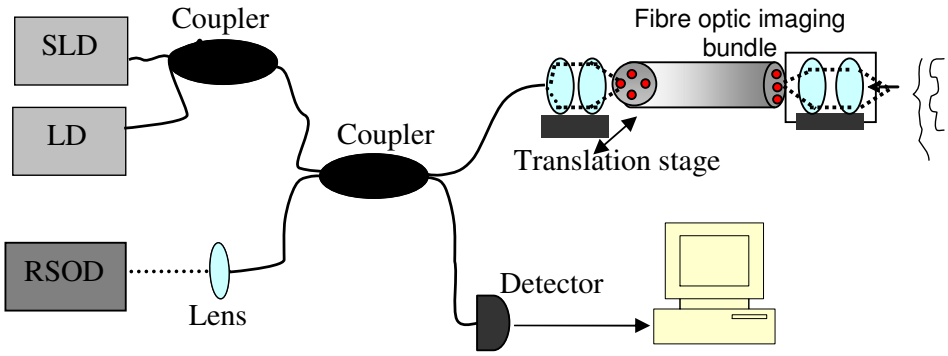

Figure 5.14: Michelson interferometer based fibre imaging bundle OCT, LD:Laser Diode, RSOD:Rapid scanning optical delay line.

This system was based on Michelson interferometer and an extra laser diode source was used for aiming purposes and their main source was an SLD emitting light at 1320nm. The light emanated from this source was guided to the Rapid Scanning Optical Delay Line (RSOD) forming the reference arm of the fibre optic Michelson interferometer. In addition the other half of the light from the source was guided by the single mode fibre of the coupler and was collimated and focused onto the input of the fibre optic imaging bundle by a system of lenses which were positioned onto a

micro-mechanical translation stage providing the means of lateral scanning the entrance plane of the fibre bundle. The emerging light from the fibre bundle in turn was collimated and focused by another system of lenses to the sample. In this study various lengths of fibre bundles were used and it was proven that if the bundle length is more than 900mm the ghost image that can be observed when using a shorter length fibre bundle are out of the display range. The limitations and disadvantages of using this approach will be discussed in a later chapter.

Later in the years that followed other designs for forward imaging probes were reported and are summarised in table 5.2

Table 5. 2: Reported forward imaging OCT probes

Year	Size (mm)	Axial Resolution (µm)	Lateral Resolution (µm)	Working Distance (mm)	Lateral scan range (mm)	Speed
1997[81]	>2.68	12	33	5	2	N/A
1997[83]	>2	10	20	5	2	100A-scans/s.
2001[85]	5	10	20	N/A	2.9	2400A-scans/s.
2003[84]	7.5x0.3	10	17	N/A	6	2400A-scans/s.
2003[86]	5	10	20	N/A	4.2	2400A-scans/s.
2004[82]	2.4	25	16	3.5	2.5	2.8kHz
2005[90]	N/A	10	12	N/A	2.8	N/A
2006[91]	1.65	9.3	10	1.4	0.93	250A-scans/s.
2006[93]	2.7	10	10	0-7.5	2.7	4096A-scans/s.

5.7 Modular View of an OCT System

From a modular point of view an OCT systems can be considered as integrated hardware and software modules and can be divided into (figure 5.15):

1. The imaging engine,
2. Computer control
3. Image processing
4. Beam delivery and probes,
5. Low coherence light source

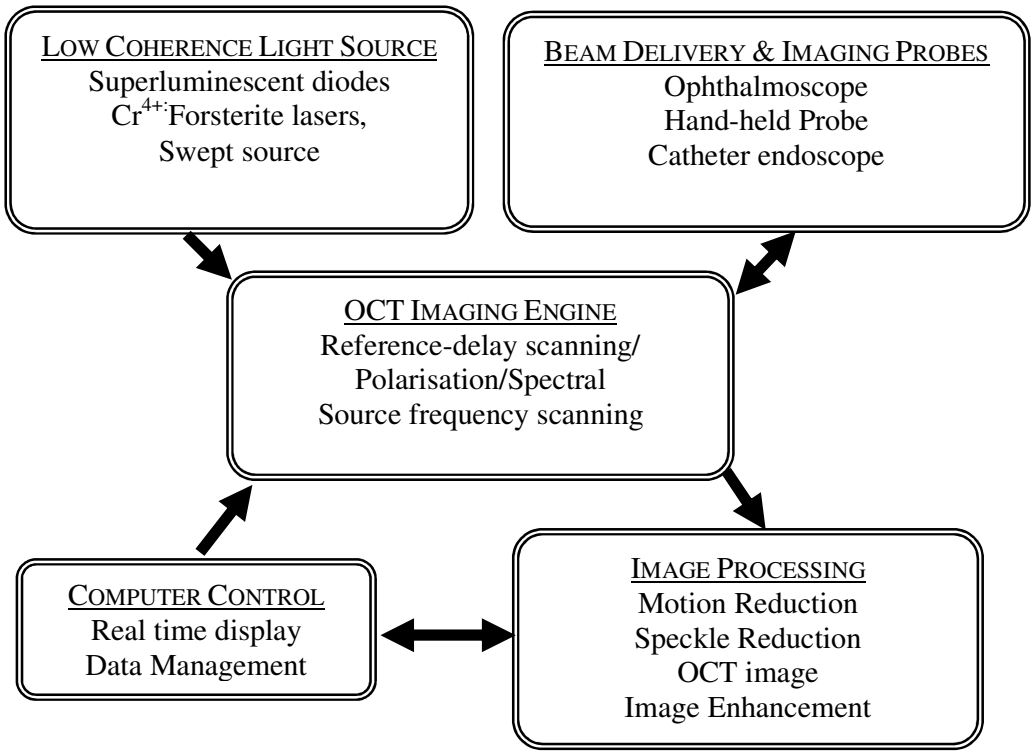

Figure 5.15: Modular view of an OCT.

5.8 Polarisation effects in OCT imaging

The state of polarisation of light doesn't only changes when it's guided through non-polarisation maintaining fibres but also when it propagates through turbid media as explained in a previous section [94]. These polarisation changes decrease the SNR and the visibility of the signal for an OCT system and thus need to be compensated to improve image quality.

This section will look at the what depths the OCT signal will start fading due to tissue birefringence for a few tissue samples Table 5.3 below shows the birefringence values of various tissue types at a specific wavelength. This data assisted the calculation of the phase change between the initial state of polarisation and the polarisation of light at different tissue depths. This was carried out to give an indication of how far the light can travel through these tissues before experiencing a phase change of 90^o which would result in zero visibility.

Table 5. 3: Birefringence values for several types of tissue

Type of tissue	Wavelength (nm)	Tissue birefringence
Porcine myocardium[96]	1310	0.00111
Myocardium [96]	1310	0.00066
Bovine tendon[97]	862	0.00370
Rat muscle [97]	856	0.0022

Using the following equation the phase change of the sample arm for each tissue can be calculated as a function of depth [97].

$$\Delta\phi = (2\pi)m + \frac{2\pi}{\lambda_0}\delta d \tag{5.10}$$

Where m is an integer corresponding to the order, λ_o is the centre wavelength and δ is birefringence.

Using the birefringence values as tabulated in table 5.3 a graph of tissue depth against phase change for various tissue types was plotted and is presented in figure 5.16. As can be observed for tissue with high birefringence like the bovine tendon, zero visibility for the signal will occur after 3mm of light travel. Esophageal tissue would be comparable to myocardium rather than bovine tendon (large amount of collagen fibres) therefore the light would have to gavel 10mm to 15mm until the signal is lost due to birefringence. As OCT systems have a depth penetration of 1-2mm the signal loss due to birefringence for these specific cases would be negligible.

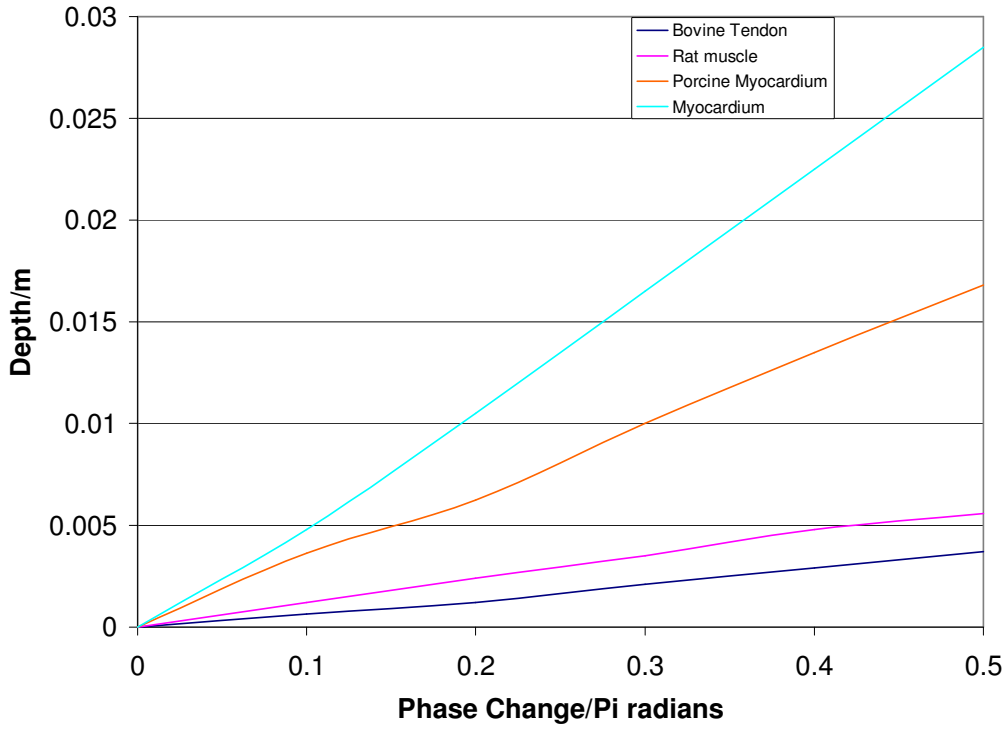

Figure 5.16: Plot of tissue depth vs phase change

References

1. Brezinski ME, Tearney GJ, Weissman NJ, Boppart SA, Bouma BE, Hee MR, Weyman AE, Swanson Ea, Southern JF, Fujimoto JG. *Optical coherence tomography for optical biopsy: Properties and demonstration of vascular pathology.* Circulation, Vol. 93 1996, pp1206-1213.

2. Rallan D., Harland C. C., Blackwell Publishing Ltd, *Clinical and Experimental Dermatology*, Vol. 29, 2004, pp 453–459.

3. Schmitt, J. M., Yadlowsky, M. J., Bonner, R. F. *Subsurface imaging of living skin with optical coherence microscopy*. Dermatology, Vol.191, 1995, pp93–98.

4. Valery V Tuchin, *Handbook of coherent domain optical Methods: Biomedical diagnostics, Environment and material science*. Kluwer Academic Publishing. NY, 2005

5. Bouma B.E., Fujimoto J. G., *Compact Kerr-lens mode-locked resonators*. Optics letters, Vol. 21, Issue 2, 1996, pp-134-136

6. Clivaz X., Marquis-Weible F., Salathe R. P., *Optical low coherence reflectometry with 1.9μm resolution,* Electronics Letters, Vol. 28, Issue 1, 1992, pp1553-1555.

7. Bouma B. E, Tearney G, Boppart S. *High-Resolution Optical Coherence Tomography using a mode-locked Ti: Al_2O_3 laser source*. Optics Letters, Vol. 20, 1995, pp1486-1488.

8. Drexler W, Morgner U, Kartner FX. *In-vivo ultra-high resolution Optical Coherence Tomography.* Optics Letters, Vol. 24, 1999, pp221-223.

9. Brezinski ME, Fujimoto JG. *Optical Coherence Tomography: High-resolution imaging in nontransparent tissue.* IEEE Journal of selected topics in quantum electronics, Vol. 55, 1999, pp1185-1192.

10. Ko T.H., Fujimoto J. G., Schuman J.S., Paunescu L.A, Kowalevicz A.M, Hartl I., Drexler W., Wollstein G., Duker J.S, Ishikawa H., *Comparison of ultrahigh and standard resolution optical coherence tomography for imaging of macular pathology,* Ophthalmology, Vol. 112, Isuue 11, 1995, pp1922

11. Wollstein G., Paunescu L. A., Ko T. H., Fujimoto J. G., Kowalevicz A. M., Hartl I, Beaton S., Ishikawa H., Mattox C., Singh O., Duker J., Drexler W., Schuman J. S., *Ultra-high resolution optical coherence tomography in glaucoma,* Ophthalmology, Vol. 112, Isuue 2, 2005, pp. 229-37.

12. Bouma B. E., Tearney G. J., Bilinsky I. P., Golubovic B., Fujimoto J. G., *Self-phase modulated Kerr-lens mode-locked Cr:forsterite laser source for optical coherence tomography*, Optics Letters, Vol. 21, Isuue 22, 1996, pp.1839-1841.

13. Ko T. H., Adler D. C., Fujimoto J. G., Mamedov D., Prokhorov V., Shidlovski V., Yakubovich S., *Ultrahigh resolution optical coherence tomography imaging with a broadband superluminescent diode light source*, Optics Express, Vol. 12, Issue 10, 2004, pp.2112-2119

14. Ergun E., Hermann B., Wirtitsch M., Unterhuber A., Ko T. H., Sattmann H., Scholda C., Fujimoto J. G., Stur M., Drexler W., *Assessment of central visual function in stargardt's diseas fundus flavimaculatus with ultra high-resolution Optical Coherence Tomography*, Invest Ophthalmol Vis Sci, Vol. 46, Issue 1, 2005, pp.310-316.

15. Herz P. R, Chen Y., Aguirre A. D., Fujimoto J. G., Mashimo H., Schmitt J., Koski A., Goodnow J., Petersen C., *Ultrahigh resolution optical biopsy with endoscopic optical coherence tomography*, Optics Express, Vol. 12, Issue 15, 2004.

16. Spence D. E., Kean P. N., Sibbett W., *60-Fsec pulse generation from a self-mode locked Ti-Sapphire laser*, Optics Letters, Vol. 16, Issue 1, 1991, pp. 42-44.

17. Zhou J. P., Taft G., Huang C. P., Murnane M. M., Kapteyn H. C., Christov I. P., *Pulse Evolution in a Broad-Bandwidth Ti-Sapphire Laser*," Optics Letters, Vol. 19, Issue 15, 1994, pp.1149-1151.

18. Fujimoto J. G., Boppart S. A., Tearney G. J., Bouma B. E., Pitris C., Brezinski M. E., *High resolution in vivo intra-arterial imaging with optical coherence tomography,* Heart, Vol. 82, 1999, pp.1221-1223.

19. Abraham E., Bordenave E., Tsurumachi N., Jonuskauskas G., Oberle J., Rulliere C., Mito A., *Real time two dimensional imaging in scattering media by use of femtosecond Cr^{4++}: fosterite laser*, Optics letters, Vol. 25, Issue 12, 2000, pp. 929-931.

20. Provino L., Dudley J. M., Maillotte H., Grossard N., Windeler R. S., Eggleton B. J., *Compact broadband continuum source based on microchip laser pumped microstructured fibre*, Electronics Letters, Vol. 37(9), 2001, pp.558-560.

21. Avdokhin A. V., Popov S. V., Taylor J. R., *Continuous-wave, high-power, in Raman continuum generation holey fibres,* Optics Letters, Vol. 28(15), 2003, pp.1353-1355.

22. Digonnet M. J., Liou K., *Analysis of a 1060nm Nd:SiO_2 superfluorescent fibre laser,* Journal of lightwave technology, Vol. 7 (7), 1989, pp.1009-1015

23. Morkel P. R., Jedrzejewski K. P., Taylor E. R., Payne D. N., *High gain superfluorescent neodymium-doped single mode fibre source,* IEEE photonics technology letters, Vol. 4 (7), 1992, pp706-708.

24. Shi Y., Poulson O., *High power broadband single mode Pr^{3+} doped fibre superfluorescent light source*, Electronics letters, Vol. 29 (22), 1993, pp. 1945-1946.

25. Iwatsuki K., *Er-doped superfluorescence fibre laser pumped by 1.48μm laser diode,* IEEE photonics technology letters, Vol. 2, 1990, pp. 237-238.

26. Takada K., Kitagawa T., Shimizu M., Horiguchi M., *High sensitivity low coherence reflectometer using erbium doped superfluorescent fibre source and erbium doped power amplifier,* Electronics letters, Vol. 29(4), 1993, pp.365-367.

27. Kumar K., Condit J. C., McElroy A., Kemp N. J., Hoshino K., Milner T. E., Zhang X. *Fast 3D in vivo swept-source optical coherence tomography using a two-axis MEMS scanning micro-mirror,* Journal of optics. A: Pure Applied. Optics, Vol. 10, 2008.

28. Huber R., Taira K., Wojtkowski M., Ko T. H., Fujimoto J. G., *High speed frequency swept light source for Fourier domain OCT at 20 kHz A-scan rate,* Photonics West - Bios 2005, Proceedings of Coherence Domain Optical Methods and Optical Coherence Tomography in Biomedicine IX (BO114)

29. http://www.santec.com [07/03/2006]

30. Huang D., Swanson E, Lin C.P., Schuman J. S., Stinson W. G., Chang W., Hee M. R., Flotte T., Gregory K., Pualifito C. A., Fujimoto J. G., *Optical coherence Tomography*, Science, Vol. 25., 1991, pp.1178-1181.

31. Ballif J., Giannoti R., Chavanne R., Walti R., Salathe R. P., *Rapid and scaleable scans at 21m/. in optical low coherence reflectometry,* Optics Letters, Vol. 21 (11), 1997, pp. 757-759

32. Swanson E. A., Huang D., Hee M. R., Fujimoto J. G., Lin C. P., Pualifito C. A., *High speed optical coherence domain reflectometry,* Optics letters, Vol. 17 (2), 1992, pp.151-153.

33. Tearney G. J., Bouma B. E., Fujimoto J. G., *High speeds phase and group delay scanning with a grating based phase control delay line,* Optics letters, Vol. 22 (23), 1997, pp.1811-1813

34. Rollins A. M., Kulkarni M. D., Yazdanfar S., Izaay J. A., *In-vivo video rate optical coherence tomography,* Optics express, Vol. 3 (36), 1998, pp.219-229.

35. Chen Z. P., Milner T. E., Dave D., Nelson J. S., *Optical Doppler tomographic imaging of fluid flow velocity in highly scattering media,* Optics letters, Vol. 22, 1997, pp. 64-66

36. Tearney GJ, Bouma BE, Boppart SA, Gloubovic B, Swanson EA, Fujimoto JG. *Rapid acquisition of in vivo biological images by use of optical coherence tomography,* Optics Letters, Vol. 21, 1996, pp.1408-1410.

37. Sergeev A.M., Gelikonov V.M., Gelikonov G.V., Feldchtein F.I., Kuranov R.E.V., Gladkove N.D., Shakhova N.M., Snopova L.B., Shakov A.V., Kunzetzova I.A., Danisenko A.N., Pochinko V.V., Ghumakov Y.P., Sterlozova O.S.. *In vivo endoscopic OCT imaging of precancer and cancer states of human mucosa*. Optics express Vol.1, 1997, pp.432-437.

38. Szydlo J, Bleuer H, Walti R. *High speed measurement in optical low-coherence reflectometry*. Measurement in Science and Technology, Vol. 9, 1998, pp.1159-1162.

39. Weiner A.M., Leaird D.E., Patel J.S., Wullert J.R. *Programmable femtosecond pulse shaping by use of a multielement liquid-crystal phase modulator*. Optics Letters, Vol. 15, 1990, pp.326-328

40. Schmitt J. M., *Optical Coherence Tomography (OCT): A review,* IEEE journal of selected topics in quantum electronics, Vol. 5, No. 4, 1999, pp.1205-1215

41. Yun S. H., Tearney G. J., de Boer J. F., Iftimia N., Bouma B. E., *High speed optical frequency-domain imaging*, Optics Express Vol. 11, No. 22, 2003, pp.2953-2960.

42. Huber R., Wojtkowski M., Fujimoto J. G., Jiang J. Y., Cable E., *Three-dimensional and C-mode OCT imaging with a compact, frequency swept laser source at 1300 nm*, Optics. Express, Vol. 13, 2005.

43. Huber R., Wojtkowski M., Fujimoto J. G., *Fourier Domain Mode Locking (FDML): A new laser operating regime and applications for optical coherence tomography,* Optics Express, Vol. 14, 2006.

44. Leitgeb R., Hitzenberger C. K., Fercher A. F., *Performance of Fourier domain vs. time domain optical coherence tomography*, Optics Express, Vol. 11, 2003, pp. 889-892.

45. de Boer J. F., Cense B., Park B. H., Pierce M. C., Tearney G. J., Bouma B. E., *Improved signal-to noise ratio in spectral-domain compared with time-domain optical coherence tomography*, Optics Letters, Vol. 28, 2003, pp. 2067-2070.

46. Ko T.H., Fujimoto J.G., Duker J.S., Paunescu L.A., Drexler W., Baumal C.R., Pulia.to C.A., Reichel E., Rogers, A.H. Schuman, J.S. *Comparison of ultrahigh- and standard-resolution optical coherence tomography for imaging macular hole pathology and repair*. Ophthalmology, Vol. 111, 2004, pp.2033–2043.

47. Choma M.A., Sarunic M.V., Yang C.H., Izatt J.A., *Sensitivity advantage of swept source and Fourier domain optical coherence tomography*. Optics. Express, Vol. 11, 2003, pp. 2183–2189.

48. Choma M.A., Hsu K., Izatt J.A., *Swept source optical coherence tomography using an all-fibre 1300-nm ring laser source*. Journal of biomedical optics, Vol. 10, 44009, 2005.

49. Gurses-Ozden R., Teng C., Vessani R., Zafar S., Liebmann J.M., *Ultrahigh-resolution ophthalmic optical coherence tomography*. Nature medicine, Vol. 7,pp. 502–507.

50. M. Sarunic, B. Applegate, S. Asrani, and J. Izatt, *Quadrature Projection Full Range High Speed Fourier Domain Optical Coherence Tomography*, Invest. Ophthalmol. Vis. Sci., E-Abstract 47, 2006.

51. Fercher A. F., Hitzenberger C. K., Kamp G., Elzaiat S. Y., *Measurement of Intraocular Distances by Backscattering Spectral Interferometry*, Optics Communications, Vol. 117, 1995, pp. 43-48.

52. Hausler G., Linduer M. W., *Coherence radar and spectral radar-new tools for dermatological diagnosis*, Journal of Biomedical Optics, Vol. 3, 1998, pp. 21-31.

53. Choma M.A., Sarunic M.V., Yang C.H., Izatt J.A., *Sensitivity advantage of swept source and Fourier domain optical coherence tomography*. Optics. Express, Vol. 11, 2003, pp. 2183–2189.

54. Nassif N. A., Cense B., Park B. H., Pierce M. C., Yun S. H., Bouma B. E, Tearney G. J., Chen T. C., J. F. de Boer, *In vivo high-resolution video-rate spectral-domain optical coherence tomography of the human retina and optic nerve*, Optics Express, Vol. 12, 2004.

55. Leitgeb R., Wojtkowski M., Kowalczyk A., Hitzenberger C. K., Sticker M., Fercher A. F., *Spectral measurement of absorption by spectroscopic frequency-domain optical coherence tomography*,Optics Letters, Vol. 25, 2000, pp. 820-822

56. Blazkiewicz P., Gourlay P. M., Tucker J. R., Rakic A. D., Zvyagin A. V., *Experimental demonstration of signal-to-noise-ratio improvement of Fourier-Domain Optical Coherence Tomography,* Optics letters, 2004, Vol 4, pp45-49.

57. Vergnole S., Lamouche G., Dufour M., Gauthier B., *Common path swept-source OCT interferometer with artifact removal* Proceedings. SPIE, Vol. 6847, 2008.

58. Hee MR, Huang D, Swanson EA, Fujimoto JG. *Polarisation sensitive low coherence reflectometer for birefringence characterisation and ranging*. Journal of Optical Society of America B, Vol. 9, 1992, pp.903-908.

59. De Boer JF, Milner TE, Van Gemert MJC, Nelson NJ. *Two diamensional birefringence imaging in biological tissue by polarisation sensitive optical coherence tomography*. Optics Letters, Vol. 22, 1997, pp.934-936.

60. Everett M, Schoenenberger K, Colston B. *Birefringence characterization of biological tissue by use of Optical Coherence Tomography*. Optics Letter, Vol. 23, 1998, pp.228-30.

61. De Boer JF, Milner TE, Nelson JS. *Determination of depth resolved Stokes parameters of light backscattered from turbid media using polarisation sensitive optical coherence tomography*. Optics Letters, Vol. 24, 1999, pp.300-302.

62. De Boer J, Srinivas S, Park B. *Polarisation effects in Optical Coherence Tomography of various biological tissues*. IEEE Journal of Selected Topics in Quantum Electronics, Vol. 5, 1999, pp.1200-1203.

63. Schoenenberger K, Colston BW, Maitland DJ. *Mapping of birefringence and thermal damage in tissue by use of Polarisation-Sensitive OCT,* Applied Optics, Vol. 37, 1998, pp.6027-6037.

64. Shifter D, Burgholzer P, Hogliner O, Gotzinger E, Hitzenberger *C. Polarisation sensitive optical coherence tomography for material characterisation and strain field mapping*. Applied Physics A, Vol. 76, 2003, pp. 947-951.

65. Yasuno, Y., Makita, S., Sutoh, Y., Itoh, M. and Yatagai, T., *Birefringence imaging of human skin by Polarization-Sensitive spectral interferometric Optical Coherence Tomography*. Optics Letters 27, 2002, pp.1803-1805.

66. Wallace F. J., *Fibre optic endoscopy,* Journal of urology, Vol. 90, 1963, pp. 324-334.

67. Burke R. P., Michielon G., Wernovsky G., *Video assisted cardioscopy in congenital heart operations,* Ann. Thorac. Surgery, Vol. 58, 1994, pp.864-868.

68. Gomes W. J., Goldenberg A., Buffolo E., Losso L. C., Marcondes W., Rolla F., Palma J. H., Goldenberg S., *Video endoscopic dissection of multiple pedicled arterial grafts for use in minimally invasive coronary artery bypass surgery,* Journal of cardiovascular surgery, Vol. 41, 2000, pp. 7-9

69. Morita T., Tamura J., Miyazaki Y., Higashidani Y., Onishi S., *Evaluation of endoscopic and histopathological features of serrated adenoma of the colon,* Endoscopy, Vol. 33, 1994, pp. 747-749.

70. Wojtkowski M., Srinivasan V. J., Ko T. H., Fujimoto J. G., Kowalczyk A., Duker J. S., *Ultrahigh-resolution, high-speed, Fourier domain optical coherence tomography and methods for dispersion compensation*, Optics. Express, Vol. 12, 2004, pp.2404–2422.

71. Tearney G. J., Boppart S. A., Bouma B. E., Brezinski M. E., Weissman N. J., Southern J. F., Fujimoto J. G., *Scanning single-mode fiber optic catheter-endoscope for optical coherence tomography*, Optics Letters, Vol. 21, 1996, pp.543–545.

72. Li X. D., Chudoba C., Ko T. H., Pitris C., Fujimoto J. G., *Imaging needle for optical coherence tomography*, Optics Letters, Vol. 25, 2000, pp.1520–1522.

73. Yang V. X. D., Mao Y. X., Munce N., Standish B., Kucharczyk W., Marcon N. E., Wilson B. C., Vitkin I. A., *Interstitial Doppler optical coherence tomography*, Optics Letters, Vol. 30, 2005, pp.1791–1793, 2005.

74. P. H. Tran, D. S. Mukai, M. Brenner, and Z. P. Chen, *In vivo endoscopicoptical coherence tomography by use of a rotational micro-electromechanical system probe*, Optics Letters, Vol. 29, 2004, pp.1236–1238.

75. P. R. Herz, Y. Chen, A. D. Aguirre, K. Schneider, P. Hsiung, J. G. Fujimoto, K. Madden, J. Schmitt, J. Goodnow, C. Petersen, *Micromotor endoscope catheter for in vivo, ultrahigh-resolution optical coherence tomography*, Optics Letters, Vol. 29, 2004, pp. 2261–2263.

76. B. E. Bouma, G. J. Tearney, *Power-efficient nonreciprocal interferometer and linear-scanning fiber-optic catheter for optical coherence tomography*, Optics Letters, Vol. 24, 1999, pp. 531–533.

77. P. R. Herz, Y. Chen, A. D. Aguirre, J. G. Fujimoto, H. Mashimo, J. Schmitt, A. Koski, J. Goodnow, C. Petersen, *Ultrahigh resolution optical biopsy with endoscopic optical coherence tomography*, Optics Express, Vol. 12, 2004, pp. 3532–3542.

78. V. X. D. Yang, M. L. Gordon, S. J. Tang, N. E. Marcon, G. Gardiner, B. Qi, S. Bisland, E. Seng-Yue, S. Lo, J. Pekar, B. C. Wilson, I. A. Vitkin, *High speed, wide velocity dynamic range Doppler optical coherence tomography Part III: In vivo endoscopic imaging of blood flow in the rat and human gastrointestinal tracts*, Optics Express, Vol. 11, 2003, pp. 2416–2424.

79. A. R. Tumlinson, L. P. Hariri, U. Utzinger, J. K. Barton, *Miniature endoscope for simultaneous optical coherence tomography and laser-induced fluorescence measurement*, Applied Optics, Vol. 43, 2004, pp. 113–121.

80. A. R. Tumlinson, J. K. Barton, B. Povazay, H. Sattman, A. Unterhuber, R. A. Leitgeb,W. Drexler, *Endoscope-tip interferometer for ultrahigh resolution frequency domain optical coherence tomography in mouse colon*, Optics Express, Vol. 14, 2006, pp.1878–1887.

81. S. A. Boppart, B. E. Bouma, C. Pitris, G. J. Tearney, J. G. Fujimoto, M. E. Brezinski, *Forward-imaging instruments for optical coherence tomography*, Optics Letters, Vol. 22, 1997, pp.1618–1620 .

82. X. M. Liu, M. J. Cobb, Y. C. Chen, M. B. Kimmey, X. D. Li, *Rapid-scanning forward-imaging miniature endoscope for real-time optical coherence tomography*, Optics Letters, Vol. 29, 2004, pp. 1763–1765.

83. A. M. Sergeev, V. M. Gelikoniv, G. V. Gelikonov, F. I. Feldchtein, R. V. Kuranov, N. D. Gladkova, *In vivo endoscopic OCT imaging of precancer and cancer states of human mucosa*, Opt. Express, Vol. 1, 1997, pp.432–440.

84. Y. T. Pan, Z. G. Li, T. Q. Xie, C. R. Chu, *Hand-held arthroscopic optical coherence tomography for in vivo high-resolution imaging of articular cartilage*, Journal of biomedical optics, Vol. 8, 2003, pp. 648–654.

85. Y. T. Pan, H. K. Xie, G. K. Fedder, *Endoscopic optical coherence tomography based on a microelectromechanical mirror*, Optics Letters, Vol. 26, 2001, pp. 1966–1968.

86. T. Q. Xie, H. K. Xie, G. K. Fedder, Y. T. Pan, *Endoscopic optical coherence tomography with a modified micro-electromechanical systems mirror for detection of bladder cancers,* Applied Optics, Vol. 42, 2003, pp.6422–6426.

87. J. M. Zara, S. Yazdanfar, K. D. Rao, J. A. Izatt, S. W. Smith, *Electrostatic micromachine scanning mirror for optical coherence tomography,* Optics Letters, Vol. 28, 2003, pp. 628–630.

88. A. Jain, A. Kopa, Y. T. Pan, G. K. Fedder, H. K. Xie, *A two-axis electrothermal micromirror for endoscopic optical coherence tomography*, IEEE Journal of selected topics in quantum electronics, Vol. 10, 2004, pp. 636– 642.

89. J. T. W. Yeow, V. X. D. Yang, A. Chahwan, M. L. Gordon, B. Qi, I. A. Vitkin, B. C. Wilson, A. A. Goldenberg, *Micromachined 2-D scanner for 3-D optical coherence tomography*, Sensors Actuators, A , Vol. 117, 2005, pp.331–340.

90. T. Q. Xie, D. Mukai, S. G. Guo, M. Brenner, Z. P. Chen, *Fiber optic bundle-based optical coherence tomography*, Optics Letters, Vol. 30, 2005, pp.1803–1805.

91. J. Wu, M. Conry, C. Gu, F. Wang, Z. Yaqoob, C. Yang, *Paired angle rotation scanning optical coherence tomography _PARS-OCT_ forward-imaging probe*, Optics Letters, Vol. 31, 2006, pp.1265–1267.

92. N. Hanna, D. Saltzman, D. Mukai, Z. Chen, S. Sasse, J. Milliken, S. Guo, W. Jung, H. Colt, M. Brenner, *Two-dimensonal and 3-dimensional optical coherence tomographic imaging of the airway, lung, and pleura*, IEICE Trans. Commun., Vol. 129, 2005, pp.615–622 2005

93. T. Q. Xie, S. G. Guo, Z. P. Chen, D. Mukai, M. Brenner, *GRIN lens rod based probe for endoscopic spectral domain optical coherence tomography with fast dynamic focus tracking,* Optics Express, Vol. 14, 2006, pp. 3238–3246.

94. Jarry G., Steimer E., Damaschini V., Epifanie M., Jurczak M., Kaiser R., *Coherence and polarisation of light propagating through scattering media and biological tissues,* Applied Optics, Vol. 37, (31), 1998, pp.7357-7367

95. Schoenenberger K., Colston B. W., Maitland D. J., Dasilva L. B., Everett M. J., *Mapping of birefringence and thermal damage in tissue by use of polarisation sensitive optical coherence tomography,* Applied Optics, Vol. 37 (25), 1998, pp. 6027-6037

96. Deboer J. F., Srinivas S. M., Park B. H., Pham T. H., Chen Z. P., Milnet T. E., Nelson J. S., P*olarisation effects in optical coherence tomography of various biological samples*, IEEE journal of selected topics in quantum electronics, Vol. 5 (4), 1999, pp.1200-1203

97. H. D. Young, *University physics,* Addison-Wesley publishing company, 1992, 8th edition.

.

Chapter 6

IMPLEMENTATION OF A TIME DOMAIN FIZEAU BASED OCT SYSTEM

6. Implementation of a time domain Fizeau based OCT system

Although a fibre Michelson interferometer based OCT allows flexible deployment, as previous chapters have explained it has serious drawbacks such as signal fading or, at times, complete signal loss, arising due to the fact that the state of polarisation of light propagating in standard optical fibre is not generally maintained. When, from time to time, the states become orthogonal, the signal will be completely lost as seen in figure 6.1.

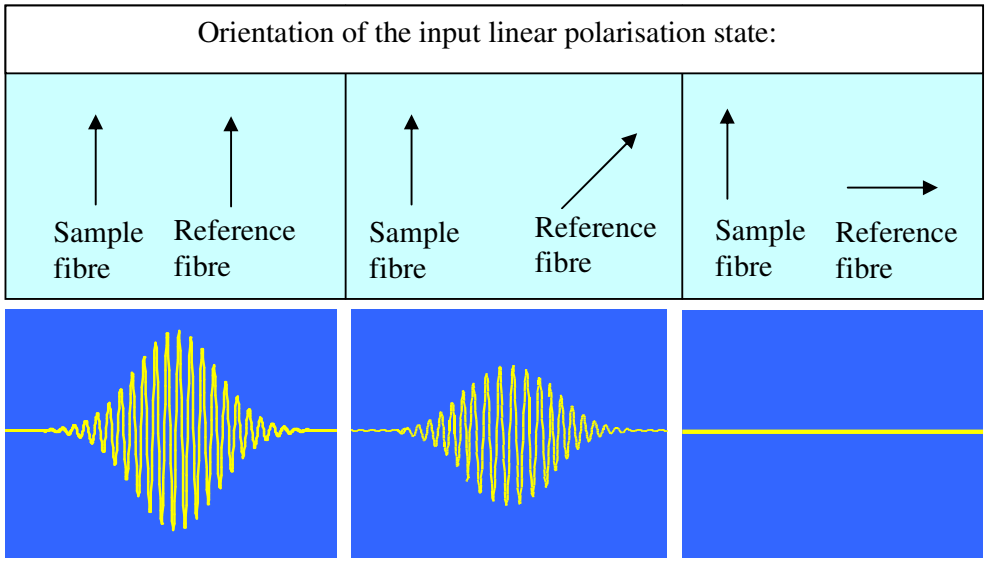

Figure 6.1: Evolution of input polarisation in the sample & reference arms of a Michelson OCT without using polarisation controllers and the resulting OCT signal.

This is not a severe problem if the sensitivity drift is slow, since the visibility value will exceed 0.5 during about 70% of the measurement time. However, polarization changes within the duration of an A-scan, such as might be experienced during endoscopic manipulation, are more of a problem. Variations on this timescale can introduce artefacts into the OCT image, in the form of spurious interfaces or regions of missing data [1].

This chapter will describe the implementation of a more beneficial configuration, the Fizeau based OCT, that will address the signal fading problem and would not require the incorporation of polarisation state controllers or high birefringence fibres thus reducing the cost of development. One of the aims of this project was to identify, specify and purchase parts or components required for the development of hardware and software. This chapter will also outline the apparatus used, implementation procedures (software and instrumental), testing procedures and will present experimental results obtained. Finally the overall performance of the developed single point time domain Fizeau interferometer based OCT will be assessed.

6.1 System overview & apparatus

Previous theoretical [2] and experimental [3] work on a time domain Fizeau based OCT system has been demonstrated using several balancing/processing interferometer configurations as illustrated in figure 6.2.

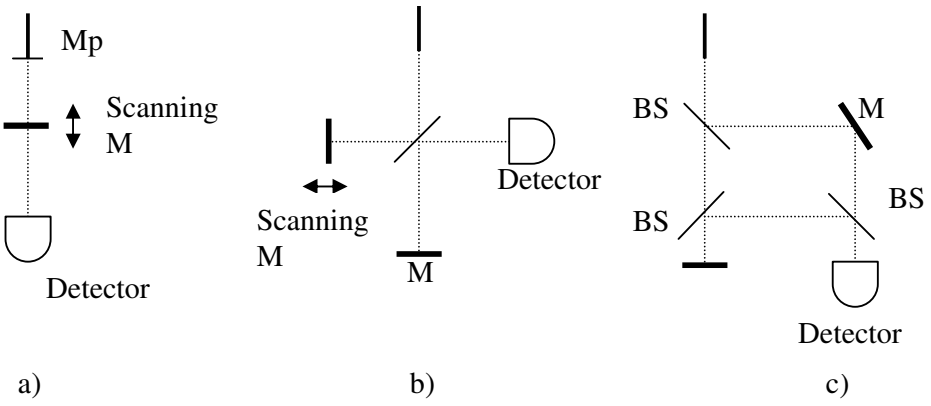

Figure 6.2: Balancing/processing interferometers a) Fabry-Perot b) Michelson c) Mach-Zehnder ; M:mirror, BS: beamsplitter.

The Fizeau interferometer as a sensing interferometer will provide environmental stability since both the reference and the sample beam will travel down the same fibre path as shown in figure 6.3. Thus any changes in fibre bend radii or any temperature fluctuation will not affect the autocorrelation signal. The reference beam will be formed by the 4% Fresnel reflection from the fibre end tip and the sample beam will be formed by the backreflected/backscattered light from the sample itself.

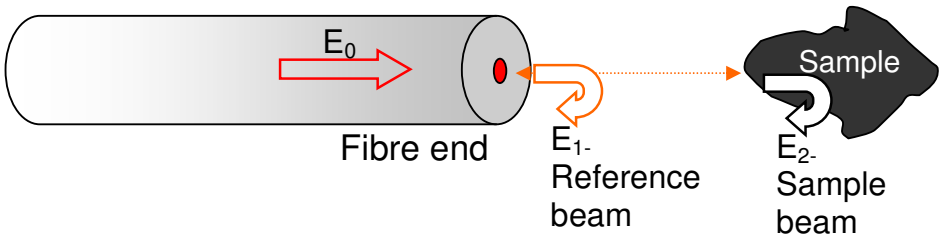

Figure 6.3: Fizeau/sensing interferometer, E_0, E_1, E_2: Electric fields

A schematic diagram of a Fizeau interferometer based OCT balanced with a Mach/Zehnder interferometer is shown in figure 6.4.

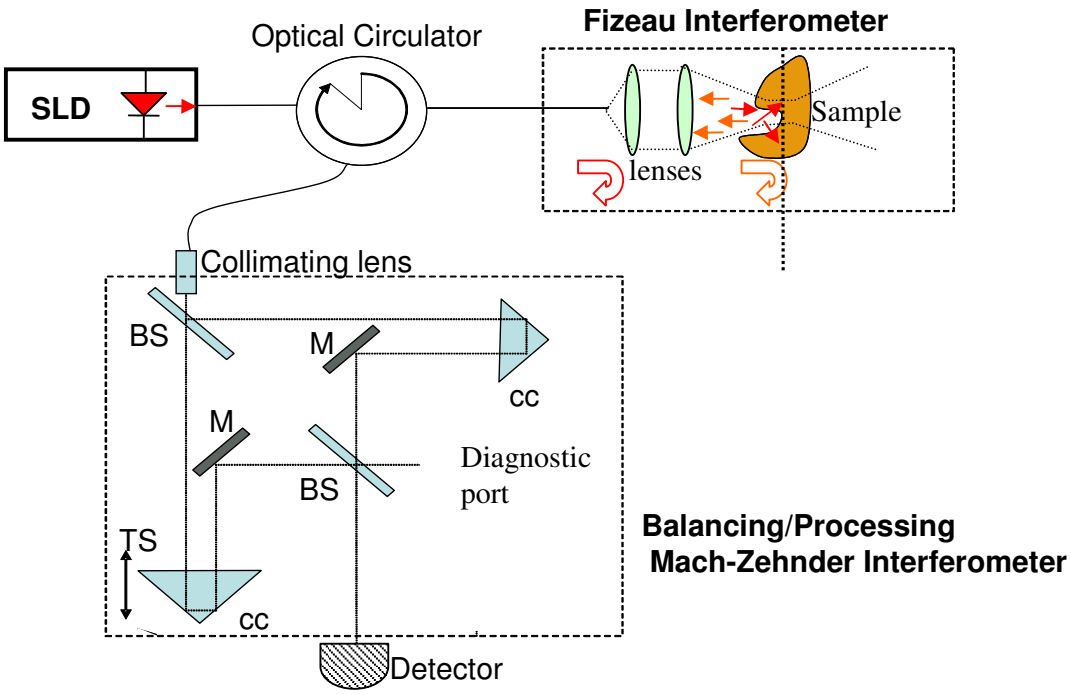

Figure 6.4: Fizeau interferometer based OCT- BS:beamsplitter, M:Mirror, TS:Translation stage, CC:corner cube

6.1.1 Optical Source

As stated in the historical review numerous optical sources have been considered for OCT. The most frequently used source for a T.D. OCT has been the superluminescent diode - SLD. This is due to its relatively low cost, robustness and ease of use. Previous experimental work in our laboratory used an SLD fibre pigtailed source centred at 1550nm wavelength with 2mW fibre output and bandwidth of 40nm (Opto Speed SLD1550D). The choice of the 1550nm wavelength would give an increased depth resolution which is important for imaging biological samples. The calculated axial resolution would be in the range of 17μm which is sufficient for measuring epithelial layer thickness (50μm-120μm) [2]. Additional output power from the source would be beneficial for the overall performance of the system. Additional power illuminating the sample increases the power of the backreflected/backscattered light from the sample hence increasing the SNR performance of the system.

For this reason a more suitable fibre pigtailed (single mode fibre) SLD source was identified and purchased. The centre wavelength of this source (*Covega SLD 1005)* was again at 1550nm and the fibre coupled output optical power was 20mW for 800mA injection current. The source was housed in a standard 14-pin butterfly package with integrated thermoelectric cooler and thermistor (thermistor resistance 10K). Due to its high output power the source was purchased with an in built fibre isolator that was spliced to the fibre pigtail. The isolator ensured safe operation as any optical feedback would not be directed to the source itself causing instabilities. The Full Width Half Maximum (FWHM) of the source was 56.2nm giving rise to 18.8μm axial resolution, again sufficient to image epithelial tissue. The light/current (L/I) characteristics of the SLD were also measured in the laboratory to ensure that they were consistent with the manufacturer's specification.

One end of a single mode fibre patchcord at 1550nm was connected to the fibre pigtail of the source and the other to the optical power meter. The SLD was connected to the temperature controller and driver current controller. Operating at a temperature of 20^{o}C-22^{o}C different injection currents were used (figure 6.5).

Although the maximum injected current to the SLD could be 800mA, resulting in 20mW output power our driver controller at the time of measurement could only reach up to 500mA resulting in 11.5mW of power at the output. As seen in figure 6.5 there is a difference of 2mW from the measured to the specified optical power that's due to connector losses.

The optical spectrum of the SLD for an OCT system is a critical factor as it determines the axial resolution of the system. Thus the spectral characteristics of the SLD were experimentally measured by connecting the end of the patchcord to an optical spectrum analyser. The spectrum analyser in turn was connected with a GPIB card to the computer. A LabView™ program was developed to control the spectrum analyser and capture the data.

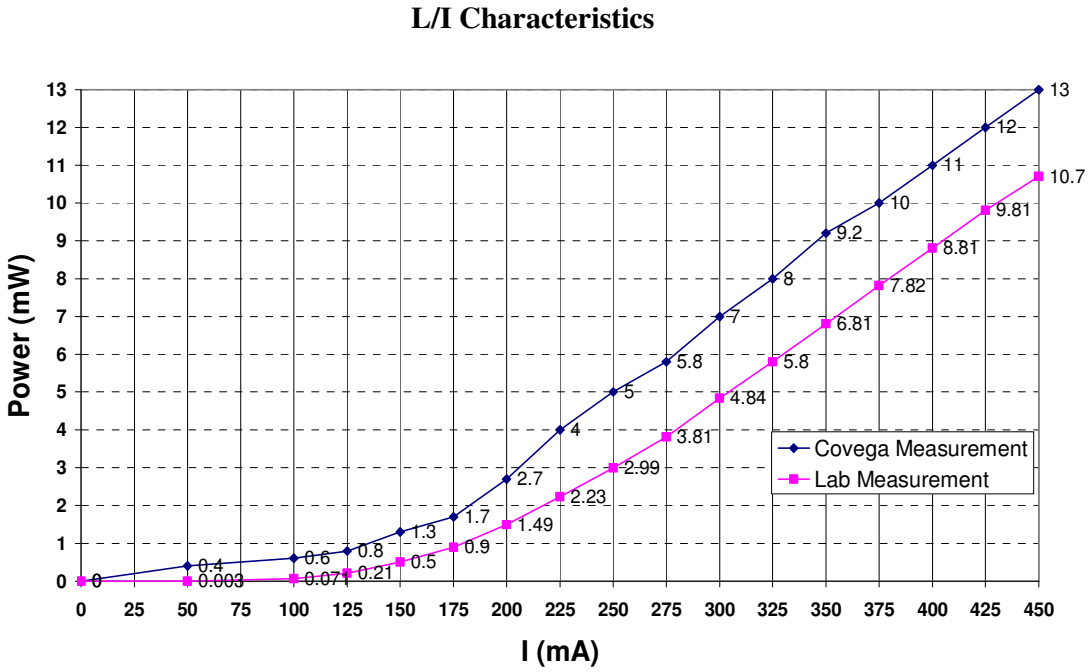

Figure 6.5: L/I (Light/Current) characteristics

Spectral characteristics of the SLD were measured at different injection currents. The captured data are plotted in figure 6.6. It can be seen that the source has a near Gaussian profile with a 54nm FWHM at 475mA injected current. It can also be observed that, increasing the injection current, the centre wavelength was shifting by a

few nanometers until it reached its specified position (1552.25nm). Furthermore the ripple on the source when the resolution on the spectrum analyser was set to 0.1 nm was measured to be 0.18dB.

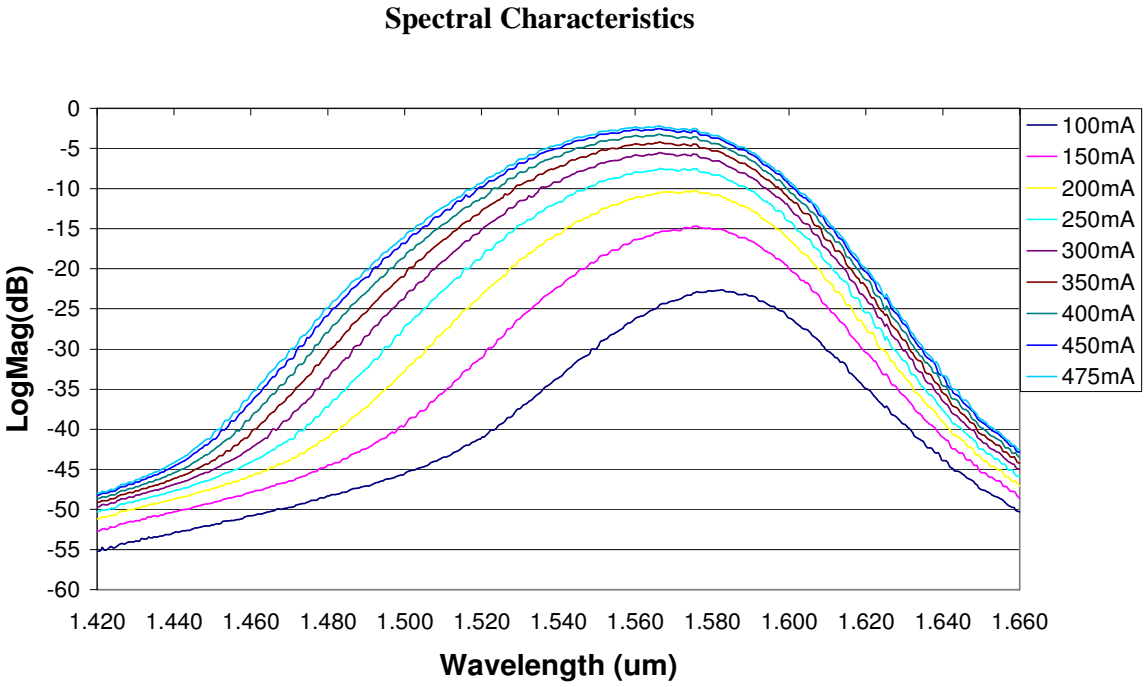

Figure 6.6: Spectral characteristics of SLD at different injecting currents.

The temperature sensitivity of the source was measured and is presented in figure 6.7. The source was driven at different temperatures from 20°C to 29°C and the spectrum dependence was measured by the spectrum analyser. The whole spectrum together with the centre wavelength was shifted by a few nanometers (10.8nm) to a longer wavelength region. As the temperature was decreased gradually to 20°C the centre wavelength recorded was according to the manufacturer's specification.

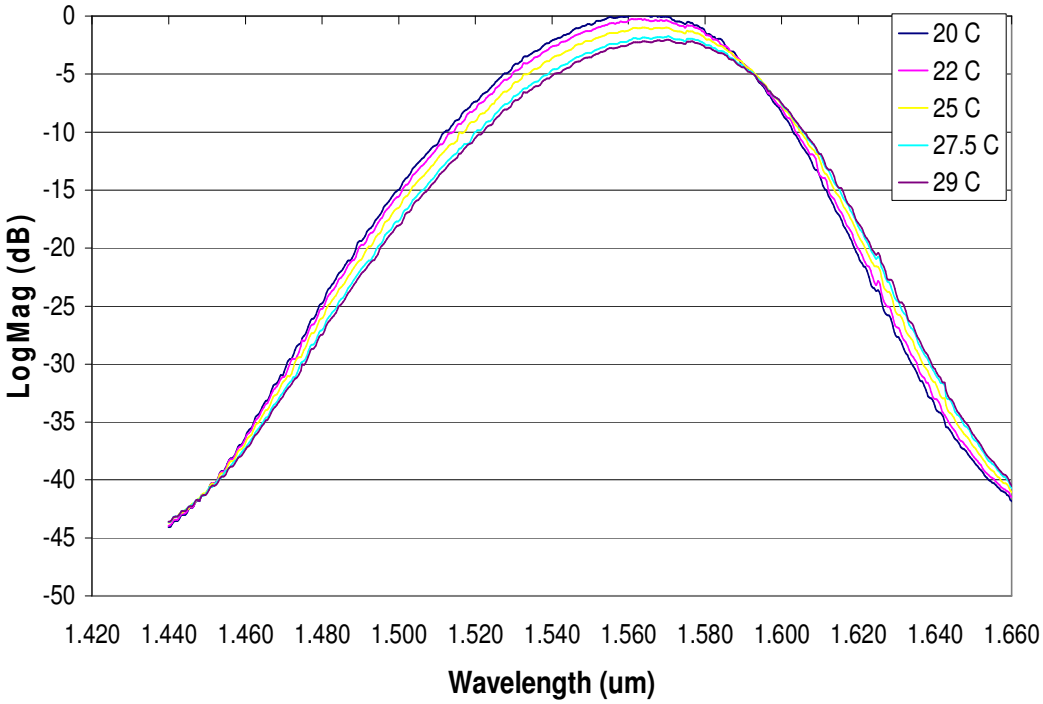

Figure 6.7: Spectral characteristics of the SLD driven at different temperatures

6.1.2 Optical Circulator

The use of an optical circulator in a Fizeau interferometer based OCT was first proposed by *Beddows et.al*. in 2002 [2]. The use of a fibre optic circulator instead of a fibre optic coupler will result in a more efficient use of the optical power in the system. In a Fizeau interferometer based OCT system with a two by two fibre optic coupler, as seen in figure 6.8, a percentage of the optical power from the optical source will be divided and directed to the sample. The third leg of the coupler will remain unused and 50% of the light is lost. The incorporation of a fibre optic circulator instead of coupler will transmit all the light from the optical source to illuminate the sample under test.

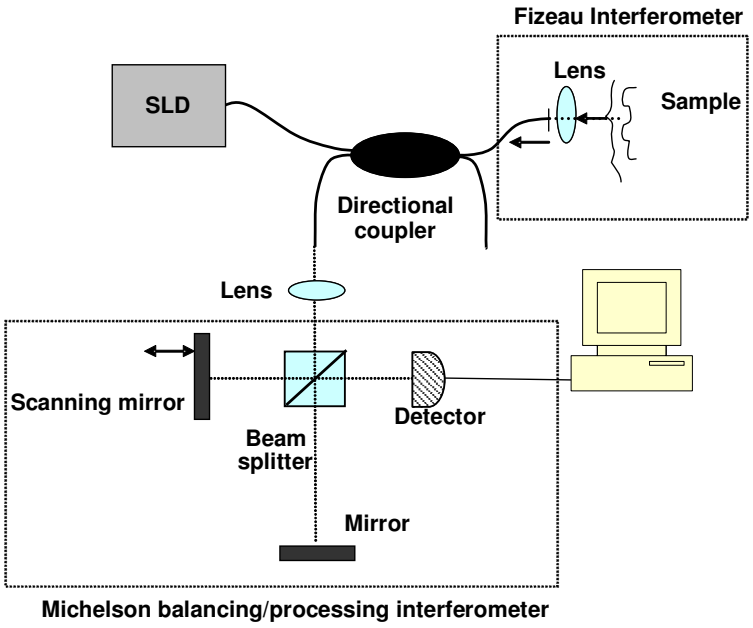

Figure 6.8: Fizeau based OCT with a Michelson balancing/processing interferometer and a fibre optic coupler.

In a circulator the light entering port 1 will be transmitted to port 2 and the backreflected/backscattered light entering port 2 will then be transmitted to port 3 as seen in figure 6.9 with almost negligible leakage of light back to port 1. It has been proved that the incorporation of fibre circulator in such a system would also increase the SNR since more light will illuminate the sample under test [3]. The circulator is a non-reciprocal device consisting of beamsplitters and glass rods and Faraday rotarors to guide the light to the desired port.

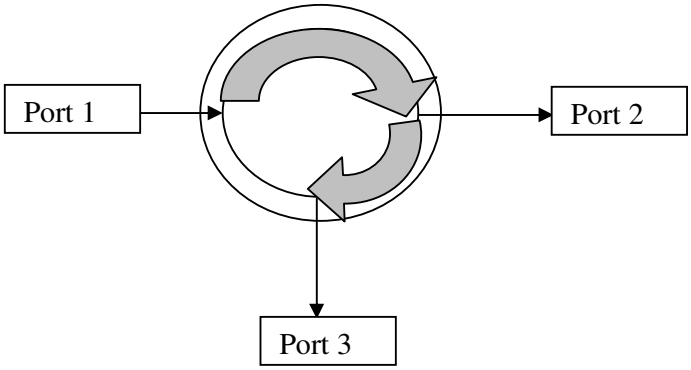

Figure 6.9: Fibre optic circulator

The circulator that was incorporated into the proposed system was operating at 1550nm, had three ports and the transmission throughput at each port was 0.87.

6.1.3 Probe/ Focusing lens system

The process followed for the design of the focusing system is outline in figure 6.10. Since the profile of the source is Gaussian, the focal length of the lenses was calculated using the laws of Gaussian optics.

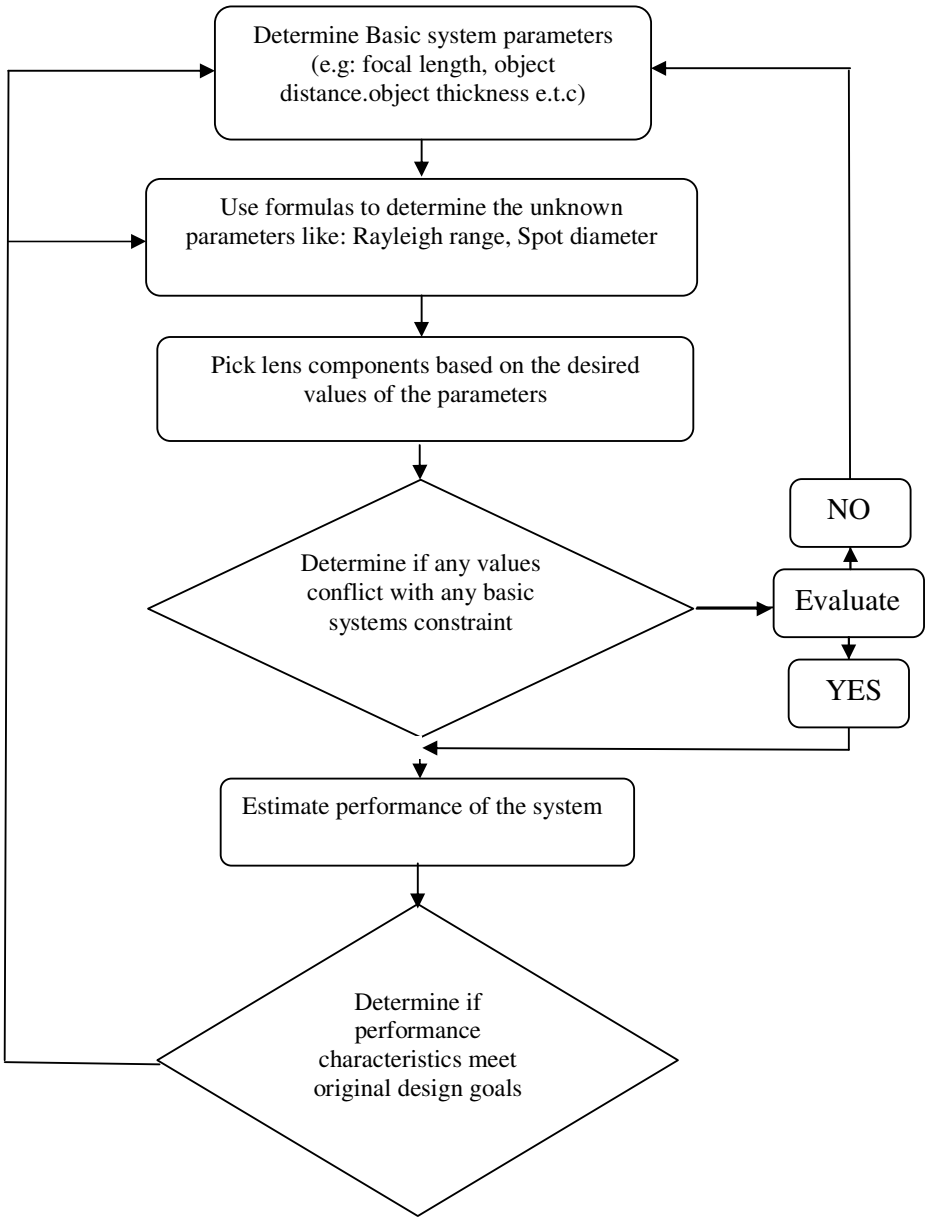

Figure 6.10: Process for the probe design

The output light from the optical fibre as seen in figure 6.11 diverges at an angle φ. This light is collected and collimated by a biconvex lens (L_1) with a constant beam diameter (W_2). This biconvex lens is placed at its focal distance (X_1) from the end of the fibre. The beam waist of the collimated beam is calculated by:

$$\tan\varphi=\frac{W_2}{X_1} \tag{6.1}$$

X_1: focal length of L_1

W_2: Beam width of diverging beam

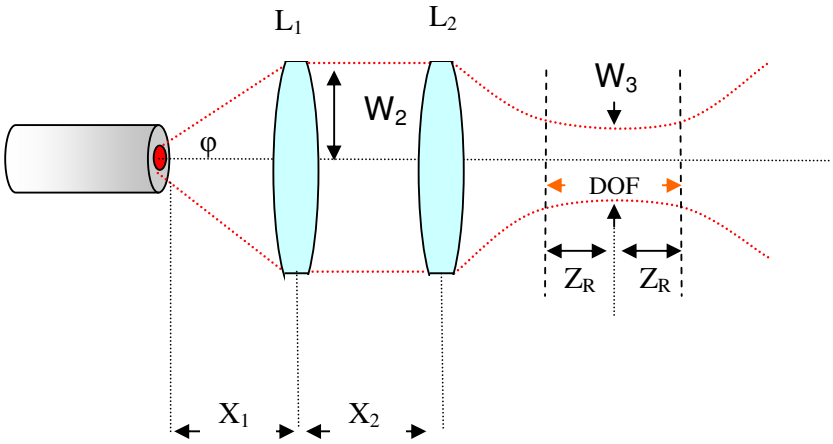

Figure 6.11: Probe schematic- DOF:depth of focus, $L_{1,2}$:lenses, W_2:beam width of the diverging beam, W_3:beam waist, X_1:focal distance, Z_R: Rayleigh range

The collimated beam is collected by a second biconvex focusing lens (L2) where the beam waist is given by:

$$W_3=\frac{\lambda f}{\pi W_2} \tag{6.2}$$

f: focal length

W_3: beam waist

The Rayleigh range (Z_R) of a laser beam is the distance from the beam waist (in the propagation direction) where the beam radius is increased by and calculated by equation 6.3 [4].

$$Z_R = \frac{\pi W_3^2}{\lambda} \tag{6.3}$$

The diameter of the first biconvex was 10mm with a focal length of 15mm and the diameter of the second was 10mm with a focal length of 40mm. Substituting these values into the above equations result in a theoretical beam waist of 23µm in air and a Rayleigh range of 540µm. Scanning can typically be performed through about three Rayleigh ranges, centred on the position of best focus, without severe loss of SNR or spatial resolution. Therefore, for this system, the accessible depth as defined by the Rayleigh range is about 1.5-2 mm. In a high-index medium, the beam waist and the Rayleigh range are increased; for a material of index 1.5, the observed performance of this system is expected to be reasonably constant within a sample depth range of about 3 mm. The resulting theoretical value is more than sufficient to image changes in thickness of epithelial tissue.

The lenses were housed into a compact cylindrical metal case of 9cm in length and 2cm in diameter as shown in figure 6.12. On one end a fibre connector was placed to allow the fibre of the second port of the circulator to be screwed on. The lenses were mounted on frames inside the housing.

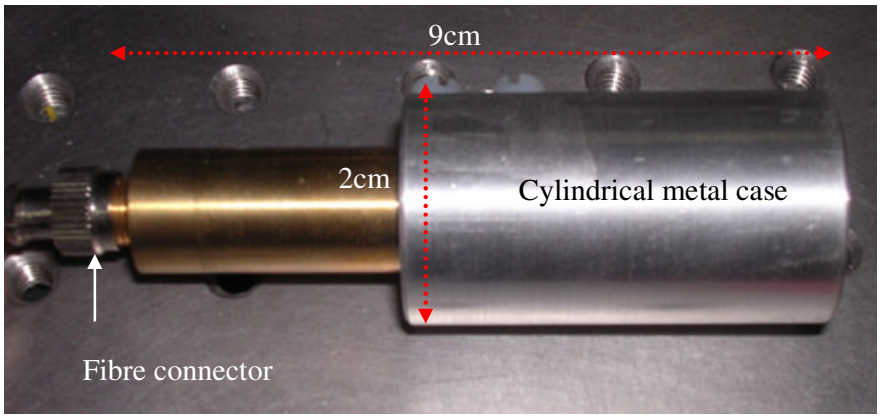

Figure 6.12: Probe

The beam from the second lens was focused 1.6mm outside the end of the metal housing. The measurements made to determine this value are presented in figure 6.13. A mirror was mounted onto an XYZ coordinate translation stage with micrometer drives and was stepped in small increments away from the probe housing. The alignment of the system probe and mirror was optimised to provide the possible throughput. The power levels were measured from the third port of the fibre circulator that was attached to an optical power meter controlled by a LabView™ program to take measurements at every step of the scanning stage.

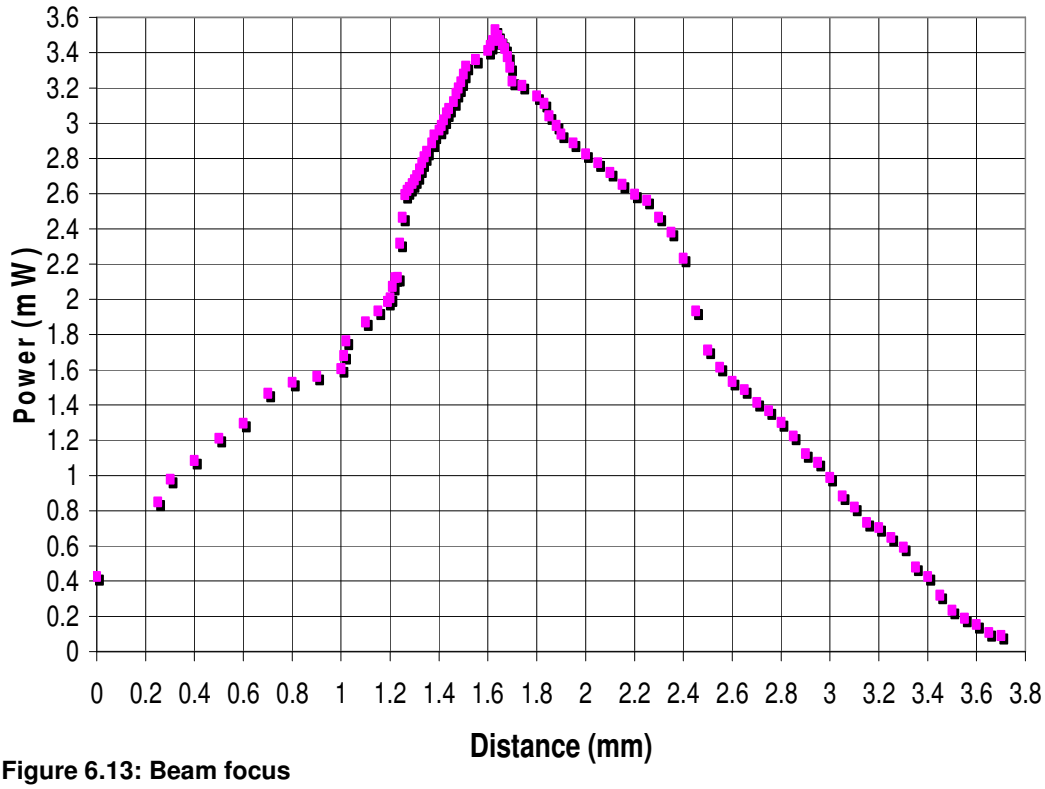

Figure 6.13: Beam focus

6.1.4 Other optics

The balancing/processing interferometer constructed was a bulk optic Mach-Zehnder type. The third port of the circulator was connected with a fibre pigtailed GRIN (Gradient Index) lens patchcord from *OzOptics Inc*. that provided a collimated constant beam diameter of 0.4mm. The collimated beam was then amplitude-divided

by a broadband plate beam splitter (1200nm-1600nm). Additional broadband beamsplitters, mirrors and corner cubes were also used as illustrated in figure 6.14.

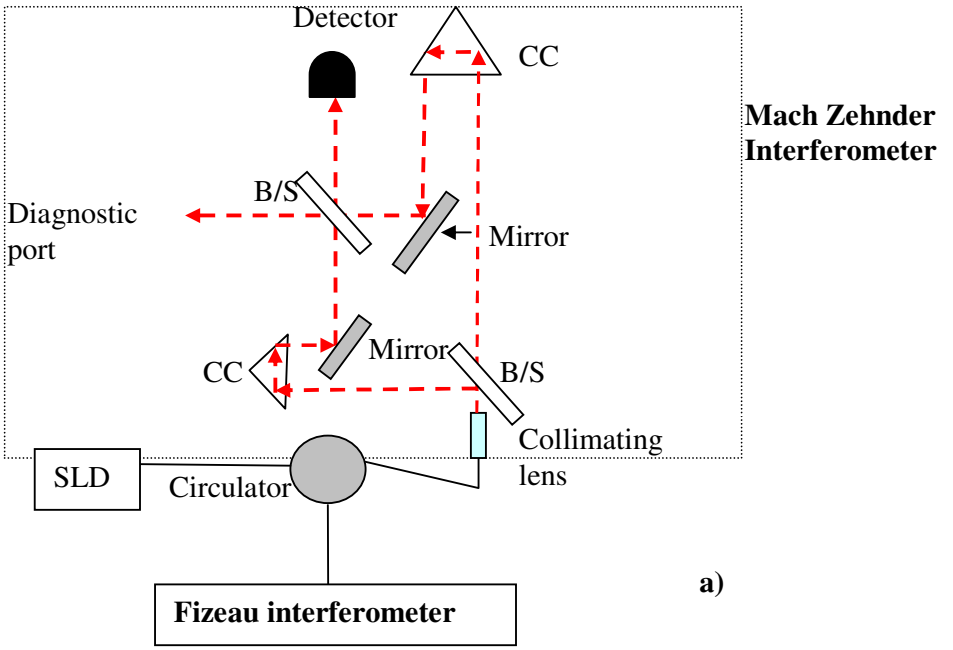

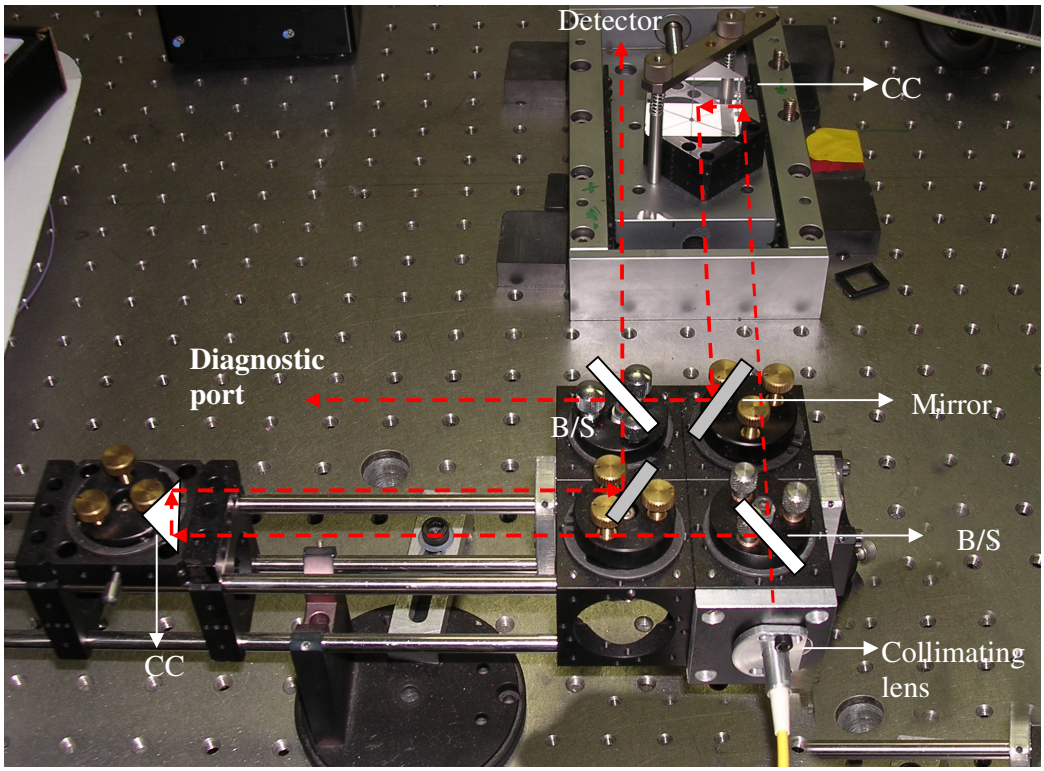

Figure 6.14: Bulk optic balancing/processing Mach-Zehnder interferometer. B/S:beamsplitter, CC:corner cube a) Schematic arrangement b) photograph.

Plate beam splitters are used in the bulk-optic part of the system because their polarisation sensitivity is lower than that of cube beam splitters. One surface of each beam splitter is anti-reflection coated to prevent "ghosting". The bulk optic Mach-Zehnder balancing interferometer was constructed and mounted in microbench equipment and stages as is depicted. The beamsplitters and mirrors were mounted onto rotational stages for a more accurate alignment. One port of the Mach-Zehnder interferometer was used for OCT signal detection and the other port for diagnostics, measuring properties like optical power levels, signal power levels etc.

6.1.5 Translation stages

A way to match the optical path length difference between the sample beam and the reference beam in a T.D. OCT system is to use a fast and accurate translation stage capable of scanning 2.5mm of distance or more. In this OCT system a linear DC motor based translation stage with rotary encoder from *Physik Instrumente* Ltd.(M-155.11) capable of scanning 10cm of distance was used. A direct current motor is operated in closed loop (feedback control mechanism-encoder); DC motor driven stages have the characteristics of lack of vibration, smooth running and wide speed range [5]. The stage was equipped with a rotary encoder (feedback control) measuring counts per revolution of the leadscrew when the stage was moving. Leadscrew drives consist of a motor driven screw with a nut coupled to the sled of the stage and the nut is spring preloaded to reduce the bidirectional errors [6]. The bidirectional accuracy is the capability of the stage to return to a position from any position regardless of direction [6]. The bidirectional repeatability of the stage according to manufacturer was 2μm and the unidirectional repeatability was 1μm. For this reason the OCT data were captured only when the stage was moving in one direction. A PID (Proportional Integral Derivative) circuit and algorithm was used to correct any motion errors and was tuned for optimum performance (High accuracy –low step and settle time). The travel distance of this stage is more than enough as only 3mm of travel is the limit of an OCT depth scan. A stage with a long travel distance though is more beneficial as the path length condition for the sample and reference beam is determined with less effort. The maximum speed of it was 1.7mm/s with a minimum incremental motion of

1μm and a straightness travel precision of less than 0.5μm. The stage's travel distance, speed and incremental step was driven with a C-843 computer PCI plug-in board that was controlled by means of a LabView™ program. The accuracy of the stage was tested during implementation of the system.

The only way to form 2D OCT images is to scan the sample beam across the sample under test [7]. Thus the probe was mounted onto a miniature translation stage (M110.1DG- figure 6.15) from the same company.

Figure 6.15: Miniature DC motor stage [7]

This DC motor stage was also equipped with a rotary encoder and the maximum travel distance was 25mm with maximum speed of 1.5mm/sec (other specification same as previously described). Hence the sample under test could be scanned over 25mm with various step sizes determining the pixel size. The image to be produced would be 3mm in depth by 25mm in the transverse direction.

6.1.6 Data acquisition, software development

At the detection port of the Mach-Zehnder interferometer an InGaAs PIN photodetector (Hamamatsu G.8376-03) was used. The detector was housed in a metal case with an amplifier circuit and a control circuit with low and high gain settings. The active area of the detector was 0.3mm^2 and had a spectral response from 900nm

to 1700nm with peak sensitivity at 1550nm. An external 12V battery provided power to the detector, and the captured signals were transmitted to the Data Acquisition (DAQ) board.

The signal processing pathway converts the interferometric optical power fluctuation at the photodetector to a digitised data array containing information on the sample reflection vs. longitudinal location. The photodetector converts the optical signal to an electrical voltage. This electrical signal is then filtered to remove the frequency components outside of the signal band. The filtered signal is amplified and then demodulated. Demodulation could be performed by at least two methods. In lock-in detection, the detector output is mixed with a waveform at the modulation frequency and the resulting baseband signal is recovered by low pass filtering. Alternatively in our case the filtered detector output could be rectified to produce the baseband signal, which is then extracted by low pass filtering. At this stage, the analog voltage is digitised using a sampling frequency greater than the Nyquist rate.

The DAQ card (PCI 6221) from *National Instruments Inc*. (NI) had a signal range sensitivity of 97.6μV when set to the maximum voltage range -10V to 10V and the resolution was 16bit.When set to minimum voltage range -200μV to 200μV it provided a range sensitivity of 5.2μV and range accuracy of 112μV. The high resolution card provided the means of detecting the smallest variation of the OCT signal in the range of μV. Detecting low amplitude interferometric signals deep within the sample is crucial as valuable information about the samples morphology could be uncovered.

The whole instrument was controlled by means of a LabView™ program. The program developed included the synchronisation of the scanning stages and data acquisition. Thus when the stage was initialised to move to a specific position data were acquired after each step. The captured data were then high pass filtered, rectified and in turn low pass filtered and stored. In addition, the Graphical User Interface (GUI) developed (Appendix A) provided the means of controlling and readjusting the speed and travelled distance of the depth scanning mechanism together with the number of scans required by the user. The data captured were also displayed on the PC screen for evaluation. Furthermore the GUI allows the readjusting of the filtering

schemes choosing different kinds of filter types and cut-off frequencies. Further improvements to this program will be described further on.

6.2 Implementation

In a Fizeau-type OCT system, the reference reflection is derived either from a glass plate positioned close to the sample or, preferably, from the reflection at the end of the delivery fibre. This removes the requirement to suppress the fibre end reflection, which can in any case be difficult to achieve. The selected reference reflectivity affects system sensitivity. The usual 4% fibre end reflectivity is quite appropriate for typical reflectivities expected from biological samples but, if required, the fibre end can be coated with titanium dioxide to increase the reflectivity up to a value of around 30% [9].

The sensitivity of the system is defined by the signal-to-noise ratio (SNR), which affects the depth-dependent contrast seen in the OCT images, and therefore both the maximum depth at which acceptable imaging can be achieved and the minimum change in refractive index that can be detected. SNR is typically rather lower in Fizeau-type OCT systems than in those based on Michelson interferometers, because there is a larger DC background, resulting from light that does not participate in the interference process [3]. The excess noise term arising from this cannot be cancelled using balanced detection, because the noise on the two complementary outputs from the Mach-Zehnder interferometer is out of phase, as is the AC signal term [9].

For the basic system shown in figure 6.8, 50% of the source light is lost in the directional coupler, and a further 50% loss occurs in the processing interferometer. In our experimental arrangement, shown in figure 6.16, the coupler was replaced by a polarisation-independent optical circulator, which greatly increases the optical efficiency.

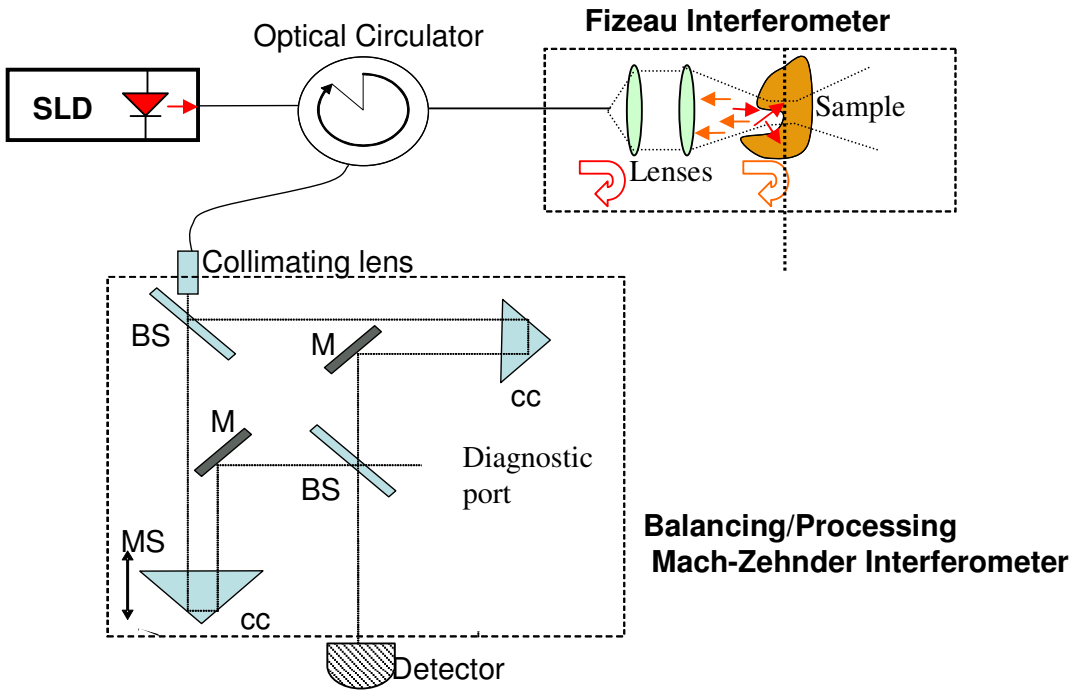

Figure 6.16: Fizeau interferometer based OCT, BS: beamsplitter, M: Mirror, CC:corner cube, MS:moving stage

The source was a pigtailed super-luminescent diode (*Covega* SLD 1005) centred at 1550 nm, with a full-width half maximum (FWHM) of 55 nm, and an output power of 9.5 mW following the fibre pigtail. Light from the source is routed through the circulator from one port to the next, with a consequent transfer loss of only a few percent. Thus, neglecting losses, all light from the broadband source is delivered by the optical circulator to the Fizeau sensing interferometer. An optical power of 7.6 mW was measured onto the sample. Both the fibre end-reflection and the back-scattered light from the sample are then directed to the bulk-optic Mach-Zehnder balancing interferometer, where the light is collimated using a fibre-connected GRIN lens and then amplitude-divided by a plate beam splitter. In one arm of the interferometer, a 45^{o} glass prism is mounted on a computer-controlled translation stage, which allows both adjustment of the gross path length difference, to match that in the Fizeau interferometer, and high-resolution A-scanning. The beam offset

introduced by the prism allows all the retro-reflected light to continue through the interferometer, and thus minimises losses. A second 45^{o} prism acts as a reflector in the other interferometer arm. In principle, only one of the interferometer arms need include a prism, but the symmetrical arrangement using two prisms is better for minimisation of dispersion effects. Measurements of optical power distribution within the system were taken at every step. An overall loss of 50% of power was measured in the processing interferometer due to multiple reflections of the beam and misalignment.

The two interferometer beams recombine at the second beam splitter. The signal is acquired by an InGaAs photodetector and digitised using a 200,000 samples/ sec, 16-bit A/D card housed within a PC. The voltage range on the DAQ card was readjusted manually in order to achieve maximum range sensitivity and accuracy of the acquired OCT signal. An A-scan was obtained using a mirror in the sample arm producing a coherence function with a FWHM value of 19 µm in air which closely agrees with theoretical estimated value of 18.8µm for the 56.2nm of bandwidth of the source. In a typical biological sample the theoretical axial resolution of the system would be about 13.4µm. The A-scan image of the system with a mirror as a sample is illustrated in figure 6.17.

The repeatability of the stage used in the depth scanning mechanism for 30 consecutive scans was found to be in the order of 1.1µm. The environmental downlead insensitivity of the system was also tested. The fibre from the circulator that formed the Fizeau interferometer was heated using a hair dryer (40^{o}C-60^{o}C) and the fibre was twisted many times (~2-3 loops). The signal visibility remained unaffected. This experiment verified that the use of a Fizeau interferometer in OCT systems will not affect the signal visibility when fibre bending and temperature changes take place.

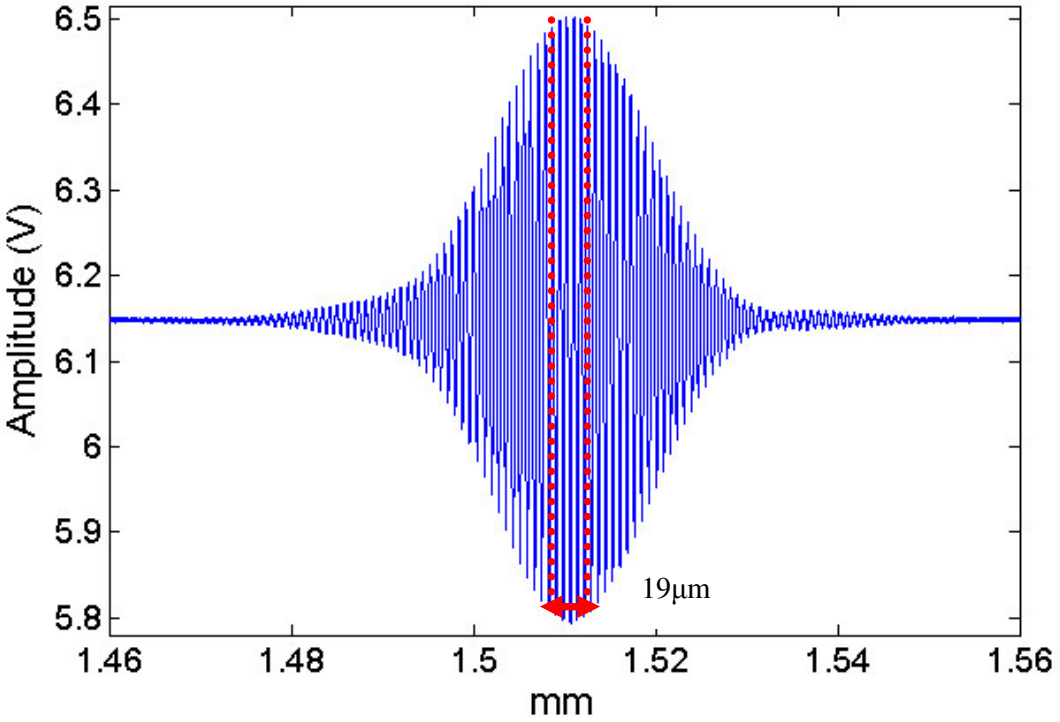

Figure 6.17: A-Scan from mirror sample showing 19µm of coherence length. (19µm width is not drawn to scale)

The probe-end focusing head gives a theoretical beam waist of about 23 µm in air, and a Rayleigh range of around 540µm. Scanning can typically be performed through about three Rayleigh ranges, centred on the position of best focus, without severe loss of SNR or spatial resolution. Therefore, for this system, the accessible depth as defined by the Rayleigh range is about 1.5-2 mm.

6.2.1 Signal processing scheme

With the stage scanning at 1 mm/sec, the frequency of the OCT fringes acquired by the photodetector was about 1.3 kHz. The DC background was first removed by passing this signal through an analogue high-pass filter with a cut off of a few Hz. A gain in the range 100-1000 was then applied, to obtain a signal in the

appropriate voltage range for digitisation. Following amplification, the signal was rectified, which is achieved by taking the absolute values of the carrier fringes. The envelope width of about 19μm is unchanged by rectification. Application of a low-pass filter, following rectification, removes the carrier fringes leaving only the envelope. Care must clearly be taken over the filter functions chosen, to minimise distortion or attenuation of the envelope signal. In our system, second-order Butterworth filters were found to give the best performance.

The signal processing described above can be carried out using either using analogue hardware filters or in software, post-digitisation. With this SLD source and with the stage scanning at 1mm/sec, a sampling rate of 5-10 kHz is required to capture the entire OCT signal, including carrier fringes. However, if the signal is first rectified and carrier fringes discarded using hardware filtering, the sampling rate required to adequately digitise the envelope signal alone is about two orders of magnitude lower, and the memory space required for image storage is also reduced. Hardware filtering is also faster. It is important, as far as possible, to match the amplitude of the electrical signal to the voltage range for the A/D card, to make optimum use of the number of bits available. This can often be partially achieved by setting an input voltage range for the card, but amplification of the signal may also be necessary.

In this system, the sampling rate of the A/D card allowed for capture of both carrier and envelope fringes, so software filtering was used. Greater choice is then available over the form of the filter functions used. A second-order Butterworth filter was found to provide the best rejection of out-of-band frequencies for this system, while minimising peak reduction and distortion. When the path delays between the reference and the sample signal were matched at the Mach-Zehnder interferometer the SNR obtained from a mirror surface in the sample arm following this filtering procedure was 80 dB. The 80dB interferometric signal detected above the noise floor indicates that the system can detect signal powers in the range of 10^{-8} of incident power.

The LabView™ program developed calculated the SNR from 30 scans by taking an average value of the peak amplitude and an average of the standard

deviation from the noise floor. Figure 6.18 shows (a) unfiltered and (b) filtered and rectified OCT signals for the mirror sample.

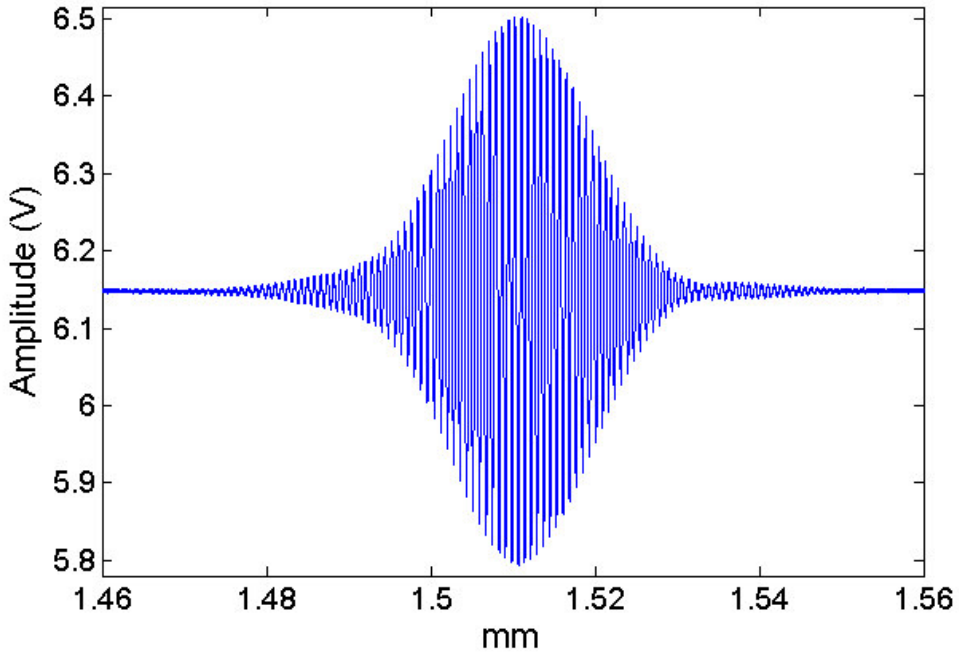

a)

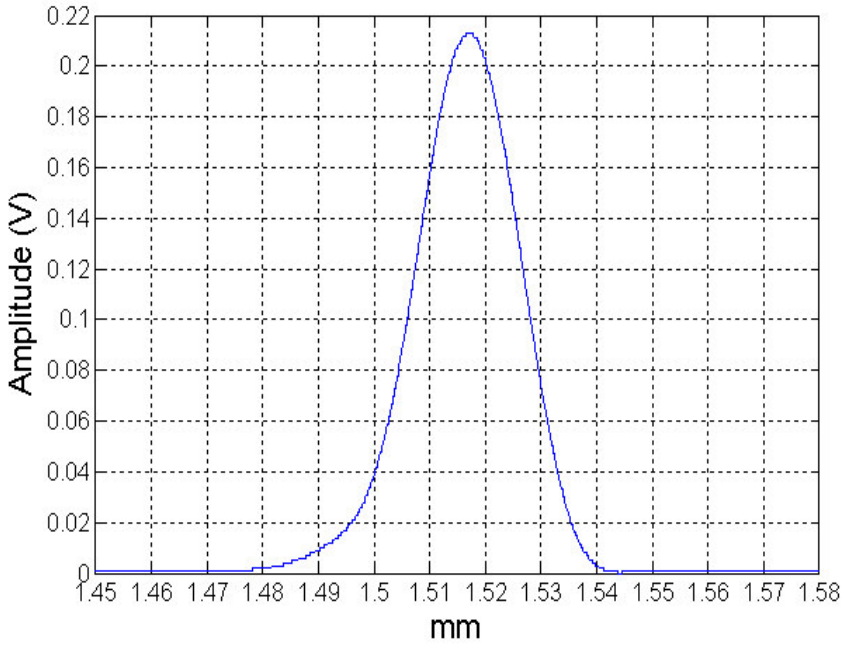

b)

Figure 6.18: a) Unfiltered OCT signal obtained with a mirror surface in the sample arm. b) Envelope signal obtained following filtering and rectification

6.3 System Sensitivity

The sensitivity of the system was assessed using Cargille oils of extremely well calibrated refractive index, deposited on a glass microscope slide of 1 mm thickness. Measurements were performed with the OCT probe mounted vertically, as shown in figure 6.19. A cylindrical collar, adjustable in height, was fixed around the probe end such that the upper end of the cylinder could be positioned at the best focus distance from the lenses and used as a platform for mounting the oil samples. This provided a repeatable measurement system, where the oil/glass interface was at precisely the same distance from the probe end on each occasion, to within a few microns. Addressing the sample with the beam coming from below the slide ensured that the beam focus position was not altered by travelling through samples of differing thickness and/or refractive index. The oils were extracted from the bottles and deposited onto the microscope glass slide with the use of a pipette.

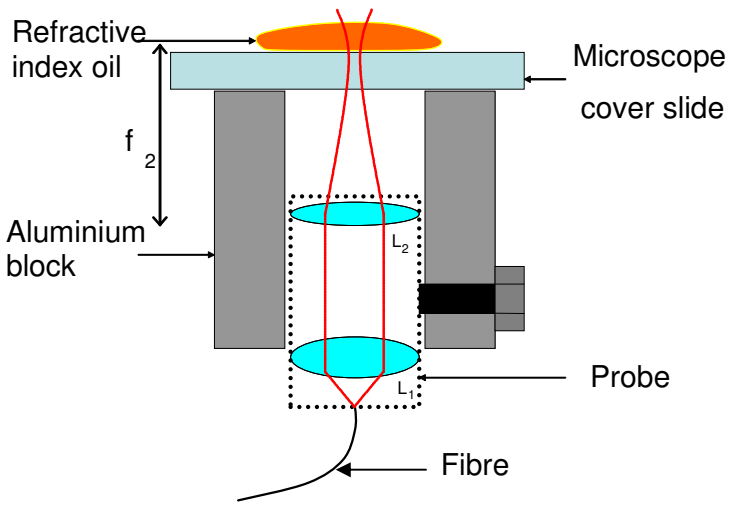

Figure 6.19: Experimental arrangement for reflectivity measurements on calibrated refractive-index oils. L = lens. The distance f_2 corresponds to the focal length of the second lens in the probe head

The Fresnel equations provide the wavelength-dependent transmission and reflectivity for an interface between two isotropic dielectric media. For normal incidence, the reflectivity equation simplifies to:

$$R = \left(\frac{n_{glass} - n_{oil}}{n_{glass} + n_{oil}} \right)^2 \quad (1)$$

Thus the reflectivity of an interface can be calculated, provided that refractive indices (RIs) are known at the wavelength of interest.

For the microscope slide, the RI was calculated from the ratio of optical thickness, measured using the OCT system as 1.52 ± 0.0011 mm, to the actual physical thickness, measured using vernier calipers as 0.999 ± 0.0011 mm. Thus the refractive index of the microscope slide can be calculated using the value of the optical thickness (OT) and physical thickness (PT):

$$n_{glass} = \frac{OT}{PT} \quad (2)$$

This yielded a RI of 1.52 (±0.01) at 1550 nm. For the Cargille oils used, the RI was quoted at 588.3 nm, and was converted to 1550 nm in each case using the Cauchy equation provided with the bottles. The RI values obtained at 1550 nm were generally about 0.01 lower than the quoted values at 588.3 nm, and the accuracy of the calculated value at 1550 nm was about 0.007.

For the experimental SNR sensitivity of the system Cargille oils of different refractive indexes were used. A set of preliminary data can be seen in figure 6.20. This figure represents experimental A-scans for three different oils. Depth scanning (X-mm) was done across 3 mm. The bottom surface of the microscope slide (air/glass interface) is represented by the first high amplitude peak.

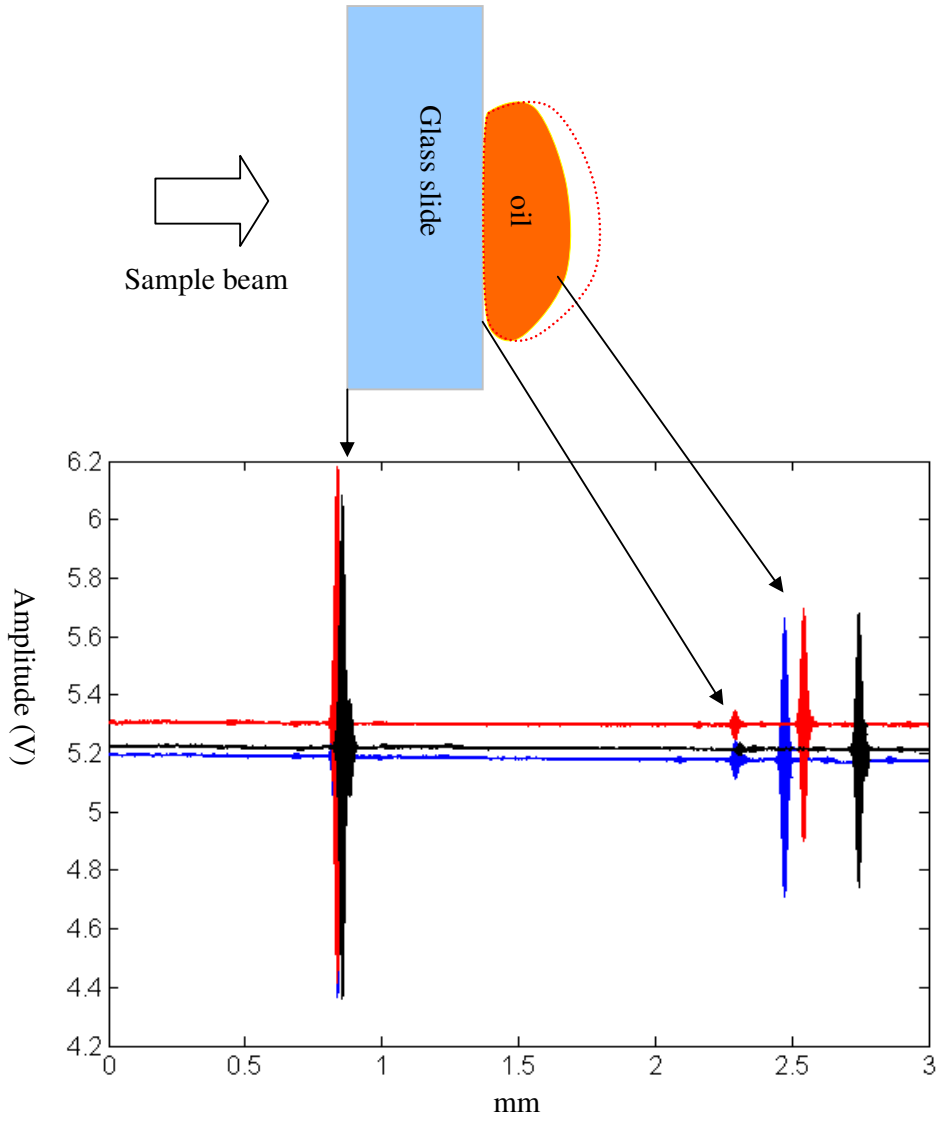

Figure 6.20: Three A scan images for 3 different oils with different RI's –Different colors show different oils

It is noted that for all three A-scans the first peak (bottom surface of microscope glass slide) is approximately in the same position. The position variation of the signal by 1.1µm is due to the bidirectional repeatability of the translation stage used. The second lower amplitude peak is the top surface of the microscope glass slide (glass/oil interface) and the third one represents the oil/air interface. The last

peaks do vary in position as different oil quantities were deposited onto the glass slide resulting in different optical and physical thicknesses.

The lower surface of the microscope slide acts as a useful reference surface for the measurements, since the OCT peak obtained for this glass/air interface should be the same on each occasion. The sample position was set by placing a microscope slide on the platform, and adjusting the mount position until the OCT signals received for the upper and lower surfaces of the slip were of approximately equal intensity. Measurements were then made for a series of oils with indices ranging from 1.400-1.600. The total reflected power was assumed to result from the sum of reflections at the air/glass and glass/oil interfaces.

$$R_s = R_{\text{air-glass}} + R_{\text{glass-oil}} \tag{3}$$
$$= \left(\frac{n_{air} - n_{glass}}{n_{air} + n_{glass}} \right)^2 + \left(\frac{n_{glass} - n_{oil}}{n_{glass} + n_{oil}} \right)^2$$

For each of the oils, the SNR of the glass/oil signal peak was assessed. This was obtained from the ratio of the peak amplitude to the standard deviation of the noise amplitude.

$$SNR_{glass/oil} = 20\log_{10}\left(\frac{A_{glass/oil}}{\sigma_{noise}} \right) \qquad \text{(Ratio not squared)} \tag{4}$$

The results are plotted in figure 6.21. As expected, the SNR decreases as the index of the oil asymptotically approaches that of the substrate. The smallest index difference measured in this experiment was about 0.01, which resulted in an SNR of 35.5 dB measured directly from the detector output, or 64.5 dB when software filtering was applied.

Differences in RI between regions within a biological sample tend to be in the second or third decimal place [11]. The results from the oil measurements suggest that the SNR obtained from this system is sufficient for good-quality imaging from samples with this level of RI variation like human skin [11].

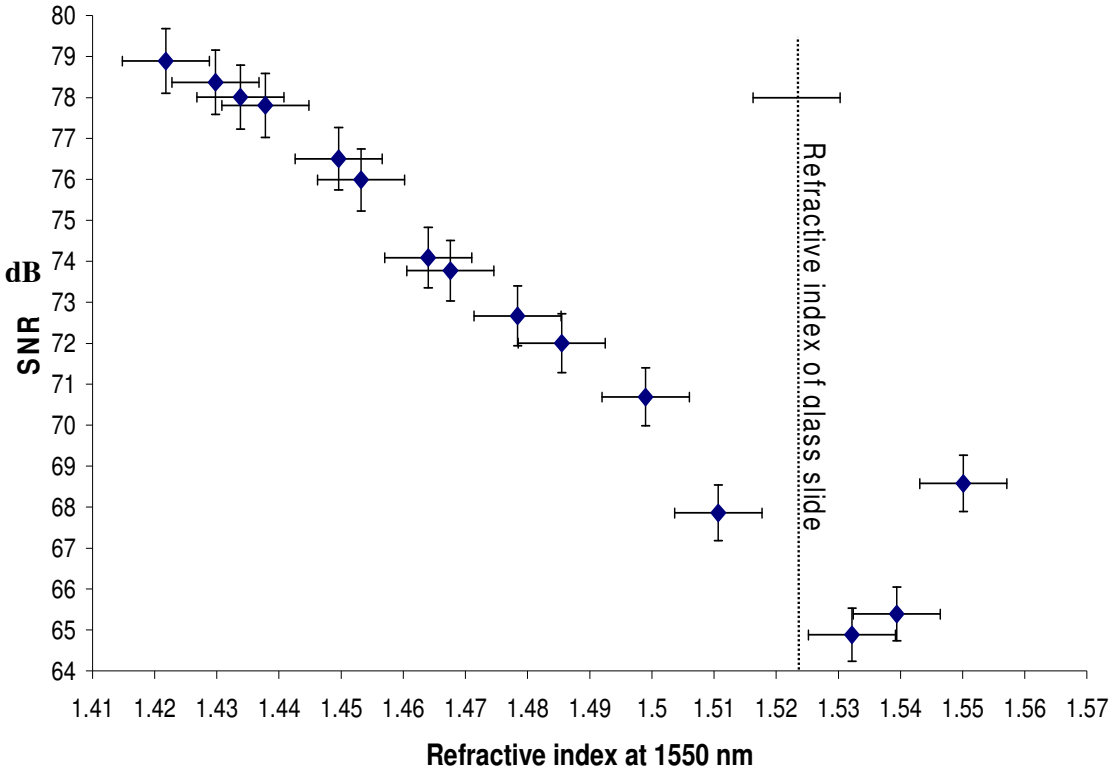

Figure 6.21: Graph showing SNR of the OCT signal for a series of oils, of known refractive index, deposited on a glass microscope slide.

6.4 A-scan results and images

More than one interference signal will be obtained from a single scan if the sample under investigation is a multilayered structure. Several multilayered lab samples were viewed and the results are presented in this section.

A brown dry onion skin was used as a laboratory sample to image the thin outer brown dry layers of an onion which were not removed. The whole onion was placed onto a mount and was moved towards the focused point of the sample beam. The onion can be considered as a useful biological sample as water and other minerals that absorb light are also found in human samples. Also structures of similar

dimensions are found in both vegetable and animal samples. The multilayer structure of the onion can be seen in figure 6.22. As expected the first peak would be the first highly reflecting surface and as the beam penetrates deeper, due to absorption and scattering the amplitude of the interferometric signals corresponding to deeper layer interfaces are reduced.

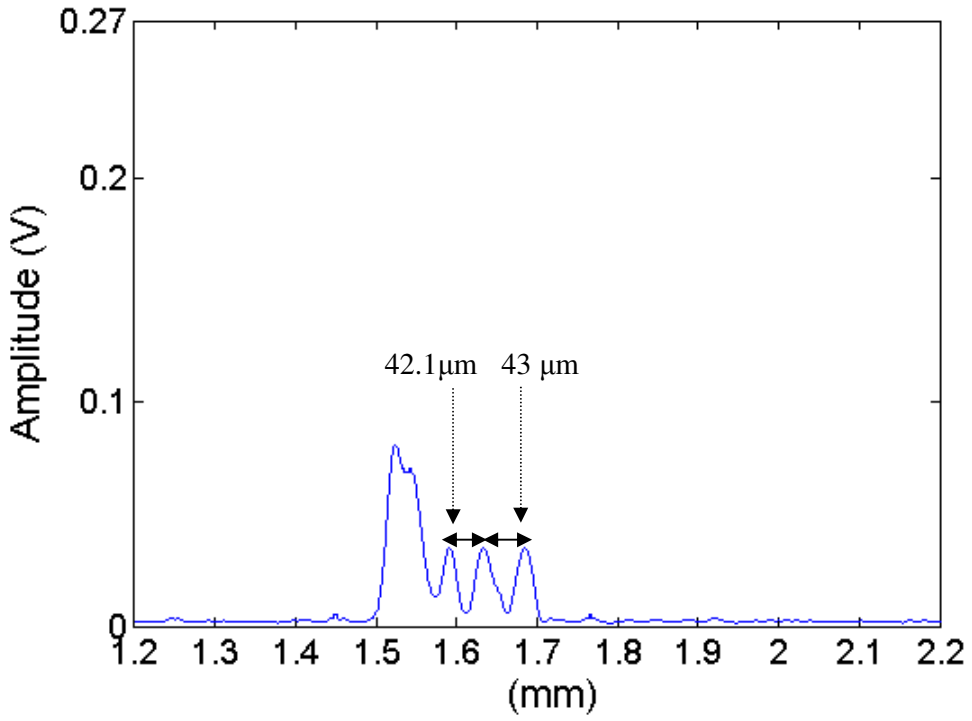

Figure 6.22: A-scan image of the outer dry brown layers of an onion after filtering and rectification

The depth information revealed for the onion skin is within 0.3mm identifying two layers. Due to high water quantities the absorption value is higher limiting the observation of deeper layers. The optical thickness for one layer for that particular onion was found to be in the range of 42-43µm. This type of sample was also used for the next proposed system and it was found that the layer thicknesses of the brown onion were the same order of magnitude (chapter 7).

The top of human thumb was also imaged. An A-scan image is depicted in figure 6.23. The thickness of the epidermis varies for different skin types. It is the thinnest on the eyelids with a thickness of 0.05 mm and the thickest on the palms and soles with a thickness of 1.5 mm [12]. The same principle applies to the dermis layer of skin. Its thickness depending on the location varies accordingly; it could be 0.3mm thick on the eyelid and 3mm on the back [12]. The stratum corneum that is also imaged in the A-scan image is the outermost layer of the epidermis and it's mainly composed of dead cells. The thickness of it varies according to the amount of protection required by the body (thick stratum corneum layer at soles of feet). Generally the thickness of this layer is about 0.04mm. In the A-scan image taken from the top of a thumb 0.5 mm of depth information is revealed. The first and second peak corresponds to the stratum corneum layer measuring roughly ~0.08 mm of optical thickness.

Although two dimensional images could be acquired for all the samples used in this research since sufficient SNR was measured by the system, due to time restrictions this research moved to the next stage.

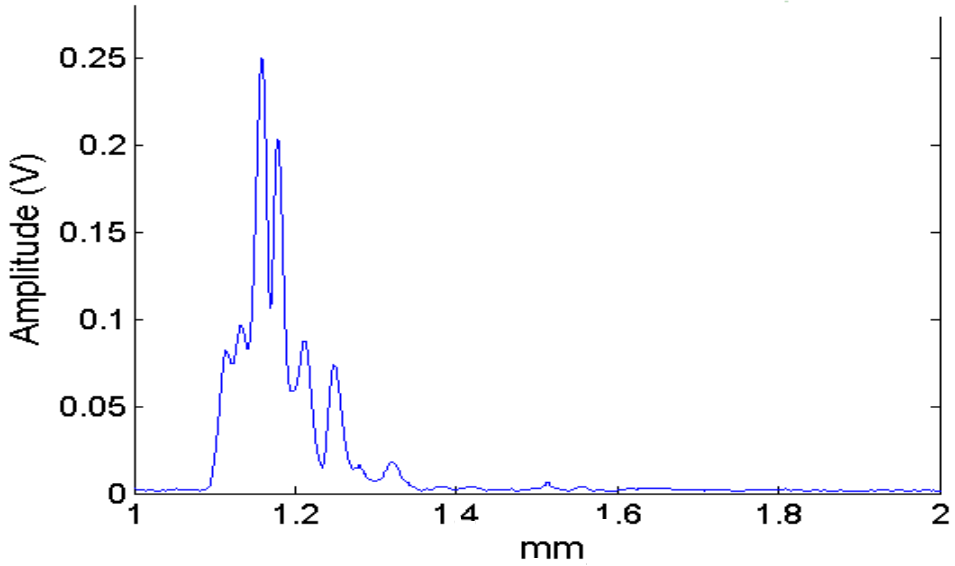

Figure 6.23: A-scan images from the top of thumb skin after filtering and rectification

6.5 Discussion

This chapter outlined the implementation procedures and challenges faced in constructing a time domain Fizeau interferometer based OCT system. In such a system since an inherent optical path length mismatch is present an additional balancing/processing interferometer is needed and possible options of different configurations for the balancing/processing interferometer were also exhibited A detailed description and schematic of the optical set-up of the system were also provided, describing step by step the development. One of the key components for an OCT system is the optical source since its characteristics are coupled with the performance of the OCT system (axial resolution). Thus, the characteristics of the optical source used were measured experimentally and analysed in conjunction with the theoretical calculated values. Procedures for the construction of a system of lenses forming a probe were also explained as the transverse resolution of OCT follows the same principles as in microscopy and depends on the characteristics of the lenses used. Filtering and data acquisition schemes of the experimentally measured interferometric signal were also investigated.

The aims of this part of the research were met through these series of experiments. The “downlead insensitivity” of the system was experimentally verified by heating and twisting the fibre end while observing that there was no change in the detected interferometric signal. Environmentally induced phase and polarisation changes did not affect the visibility of the interferometric signal thus there is no need for incorporating polarisation maintaining parts that will add to the cost [13]. Proper modifications have to be made for the system to operate in vivo. These modifications could include the miniaturisation of the probe, the proposed diameter could be in the range of 1-2.5 mm [14]. Improved depth and transverse scanning speeds are required to avoid artefacts being generated from the sample motion.

Secondly, the value of the experimentally measured SNR of the system is sufficient to image biological structures. Several lab samples and biological samples were used and A-scan images provided sufficient information of their refractive index

profile. Measurements of the refractive indices and optical length were exhibited for several samples.

This system used time-domain processing techniques, but it would also be possible to operate the system as a Fourier-domain instrument [15] by fixing the path-length in the processing interferometer and dispersing the output signal onto a spectrometer. This inevitably leads to a relatively large DC background, and it might appear preferable to dispense with the processing interferometer altogether. However, the path-length inherent to the Fizeau interferometer is generally too large to allow for Fourier-domain operation in this mode, unless an external reflector is used to generate the reference reflection or a probe end miniature interferometer is used [15].

Concluding the first stage of this research work, it provided the desired experimental values for the SNR of the system coupled with promising results of A-scan images to continue onto the second stage. The incorporation of a coherent imaging fibre bundle is described in chapter 7.

References

1. Lefevre, HC, *Single-mode fibre fractional wave devices and polarization controllers*, Electronics. Letters, Vol. 16, 1980, pp778-780.

2. Beddows R, James S.W., Tatam R.P., *Improved performance interferometer design for optical coherence tomography,* Proceedings of the 15th International Conference on Optical Fibre Sensors, Portland, Oregon, USA, 2002, pp. 527–530.

3. Ford H. D., Beddows R., Casaubieilh P., Tatam R. P., *Comparative signal-to-noise analysis of fibre-optic based optical coherence tomography systems*, Journal of modern optics, Vol. 52, No. 14, 2005, 1965–1979.

4. Pedrotti F. L., *Introduction to optics,* Published by Pearson Prentice Hall, 2006, ISBN 0131499335, 9780131499331

5. Naitoh H., Tadakuma S., *Microprocessor-based adjustable-speed DC motor drives using model reference adaptive control,* IEEE transaction on industry applications, 1987.

6. Dote Y., Servo *Motor and motion control using digital signal processors,* Prentice-Hall Digital Signal Processing Series, 1990,ISBN:0-13-807025-3.

7. Podoleanu, A. G., Rogers, J. A., Jackson, D. A., Dunne, S., *Three dimensional OCT images from retina and skin*. Optics Express, Vol. 7, 2000, pp 292–298.

8. Physik Instrumente, website: http://www.pi.ws [09/02/2008]

9. Naci Inci M, Kidd S R, Barton J S, Jones J D, *Fabrication of single-mode fibre optic Fabry-Perot interferometers using fusion spliced titanium dioxide optical coatings*, Measurement Science and Technology, Vol. 3, 1992,pp 678-84.

10. Sharma U, Kang J U, Fried N M , *Fizeau optical coherence tomography: sensitivity optimization and system analysis,* Conference on Lasers and Electro-Optics (CLEO) (San Jose, California, 22-27 May, 2005) Vol 3. , 2005, pp2061-2063.

11. Ding, H., Lu, J.Q., Wooden, W.A., Kragel, P.J. and Hu, X.-H., *Refractive Indices of human skin tissues at eight wavelengths and estimated dispersion relations between 300 and 1600 nm*, Institute of physics publishing, Physics in medicine and biology, Vol. 51, 2006, pp1479-1489.

12. Montagna W. *Structure and function of skin*, New York publishing, Academic Press, 1962.

13. Kersey A D, Marrone M J, Dandridge A, Tveten A B, *Control scheme for polarization-induced signal fading in multiplexed optical fibre interferometric sensors,* Journal of lightwave Technology, Vol. 6, 1998, pp1599-1609

14. Divettia A., Hsieh T. H., Zhang J., Chen Z., Bachman M., Li G. P., *Dynamically focussed optical coherence tomography for endoscopic applications,* Applied physics letters, Vol. 86, 2005.

15. Leitgeb R, Hitzenberger C K and Fercher A F, *Performance of Fourier domain vs. time domain optical coherence tomography,* Optics Express, Vol.11, 2003,pp 889-894

Chapter 7

IMPLEMENTATION OF A FIZEAU BASED OCT SYSTEM USING COHERENT FIBRE OPTIC IMAGING BUNDLES

7. Fizeau interferometer based OCT system using fibre optic imaging bundles

The previous chapter described the advantages of environmental stability offered by a Fizeau interferometer based OCT system. It explained the experimental procedures and implementation challenges faced during the construction of such a system. The data that were collected and analysed provided sufficient knowledge and information for the implementation procedures to be followed for a similar system incorporating coherent fibre optic imaging bundles.

Ex-vivo measurements on biological samples using OCT can be conveniently performed using bulk-optic OCT instrumentation [1], but the acquisition of in vivo images, for example from arteries or within the gastro-intestinal tract, requires the use of a flexible, endoscopic probe [2]. It was realized early in the history of OCT that the

incorporation of optical fibre components was unavoidable. As described in chapter 5, in recent reports, OCT endoscopic and catheter-based probes have been developed for clinical use [3, 4] to image tissues. Previous reports described successful implementations of such probe systems using movable parts such as microelectromechanical systems (MEMS) micromotors [4], (MEMS) mirrors, rotary fibre joints [5] or [6] linear motors. However, the construction of such scanning systems for use inside the body is a complex task, as electrical power must be delivered to the endoscope tip to drive the scanner and the whole system must be miniaturised to fit inside an endoscope. Since miniaturisation is necessary the mirror size and numerical aperture are limited by the endoscope size thus the lateral resolution of the system is subsequently restricted. Additionally the sweep distances obtainable with MEMS probes may also be quite limited due to the confined spaces of the endoscopic probe.

This chapter will aim to describe a novel approach for a flexible OCT endoscope using coherent fibre optic imaging bundles. This chapter will give an overview and technical description of coherent imaging fibre bundles and provide a description and an analysis of the implementation procedures followed. Finally A-scan images and 2D images produced by the system will also be presented.

7.1 Coherent fibre optic imaging bundles

For video imaging of internal structures and tissues during internal exploration and surgery coherent optical fibre bundles were previously used [7, 8]. Such means enable a physician or surgeon to see the surface of internal structures using visible light by means of a video camera coupled to one end of the fibre bundle [9].

Typically a coherent fibre bundle consists of a bundle of optical fibres that typically are arranged in such a way to remain parallel to each other for the entire length of the bundle, meaning that the nearest neighbouring fibres of a particular fibre

on one end of the bundle are also the neighbouring fibres on the other end. The fibres of the bundles used in this system were arranged in the same relative position at both ends and in the middle were loose. Each fibre in the bundle typically has a high refractive index core, and a low refractive index cladding. The light emanating from an optical source and incident onto one end of the bundle is confined to the cores by total internal reflection. If an image is focused onto one end of the bundle, various points on the image are conducted through their respective fibres to the other end of the bundle. Since the bundle is coherent, these points or pixels of the image appear in the same relative positions as they were on the incident end. Thus every point of light emerging from the bundle will constitute the image and this can be further imaged onto a sensor and be displayed onto a monitor.

Typical diameters of such bundles are in the range of 0.5-5.0 mm, and their lengths can vary from 10 cm or longer, up to several meters. Such bundles can hold from several hundred to 100,000 fibres forming a very detailed picture (100,000 pixels). Due to their small size and flexibility the bundle can be threaded through the vascular system, the gastrointestinal, urinary, or respiratory tracts and can be integrated into a catheter with surgical instruments. Consequently the advantage of using such bundles for endoscopic OCT is to visualize regions beneath organs that a rigid endoscope would not be able to reach. The separation between the cores which is typically a few μm keeps the light from the cores from mixing together, at least substantially, so that each core conducts essentially one picture element of the resulting image. The fibres in the bundle are made of durable silica or plastics and can tolerate tight bends without breaking [8]. Therefore feeding the bundle down an artery with tight bends will still allow OCT images to be formed without any fibres (pixels) breaking during surgical procedure.

As previously stated in conventional OCT systems, a single focused beam is scanned across the object to create the three-dimensional image. This technique though is not suitable for imaging with a fibre bundle as each fibre in the bundle forms a discrete imaging channel rather than defining a continuous space. Therefore the beam must be scanned in discrete steps across the input end of the bundle. Stepping or continuous scanning must be made according to the separation of the

fibres and according to the bundle dimensions in such way that the light will be confined in one fibre at a time.

7.1.1 Properties of coherent fibre optic imaging bundles

Since the imaging bundle is fundamental to the operation of the OCT system to be researched its properties were also investigated and are presented in this chapter. The fibres that are currently used in a conventional OCT system are single mode fibres as the signal conforms to a single spatial mode which is transmitted through the fibre at almost uniform speed. The fibres that are used in a coherent fibre bundle are usually multimode fibres but the bundles used in this study are very close to single mode operation. The signal input into a multimode fibre will be divided over many modes and each of them travels at a slightly different speed due to dispersion. This would create ghost artefacts into the OCT image as several overlapping copies of the signal would arrive at different times. This phenomenon though could be eliminated if longer lengths of fibre bundles in order of 1m and above are chosen as *Tuqiang Xie et. al.*, described in 2005 [10].

Another consideration when using fibre bundles for OCT system is the crosstalk of light between neighbouring fibres causing image distortions. As the fibre cores in a bundle are so closely spaced light coupling between the cores can also occur. Guided modes in fibres also have exponentially decaying evanescent tails outside of the cores, thus the mode in each fibre is not completely confined to the core and extends outside of it. So if the fibres in the bundle are spaced closely to each other the mode tail of one fibre can well overlap with an adjacent fibre. As a result the mode of one core can leak into nearby core causing ghost images to appear in an OCT. Additionally crosstalk signals could also coherently interfere producing a much larger distortion to coherent light.

Two types of fibre imaging bundle (supplied by *Schott Fiber Optics Inc.*) were used in this work. Initially, a wound bundle, 1.83 m in length and made up of 300 X

300 fibres, was employed. The bundle comprises many hundred 'multifibres' wound on a mandrel. The multifibres are groups of 5 X 5 individual fibres assembled on a 10 µm centre spacing with an 8µm core in a square-packed arrangement. Figure 7.1 illustrates the packaging arrangement. The ends of the bundle are fused to produce a rigid section enclosed in a ferrule of 3cm long, while the centre portion remains flexible. Bundles are purchased as a component of selected length with both ends polished to a high-quality optical finish.

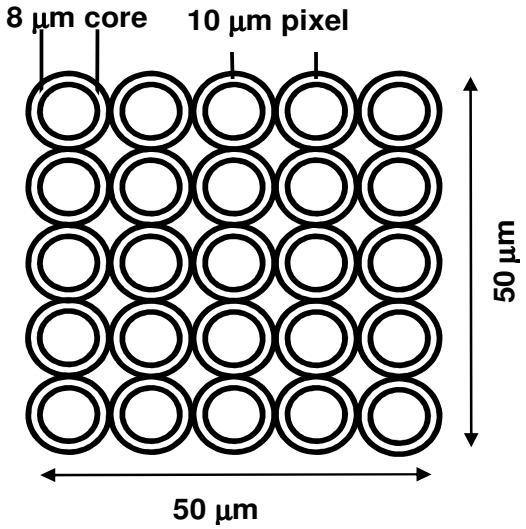

Figure 7.1: Packaging arrangement of wound bundle

The packaging arrangement of the wound bundle was also imaged with a CCD camera. The light from an SLD operating at 830nm was collimated and partially focused with an aspheric lens onto one end of the bundle as depicted in figure 7.2. The light that was transmitted through the bundle and the light exiting the bundle was collected by a second aspheric lens and the image was projected onto a 12-bit digital camera (LaVision) with a 640 by 480 pixel array and a variable integration time. An image of the packaging arrangement of the wound bundle can be seen in figure 7.3.

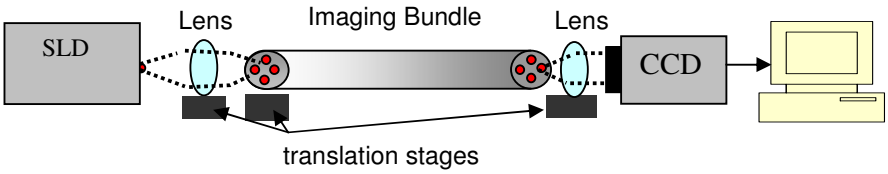

Figure 7.2: Imaging the packaging arrangement of the wound bundle.

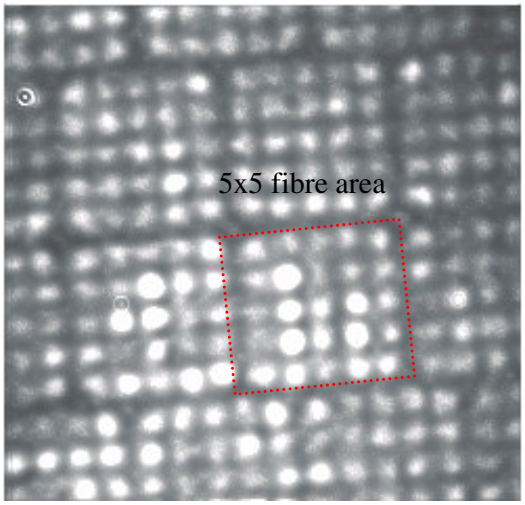

Figure 7.3: Packaging arrangement of wound bundle illuminated by an SLD and projected onto a CCD camera (640x480 pixells)

Image (a) in figure 7.4 shows a wound bundle.

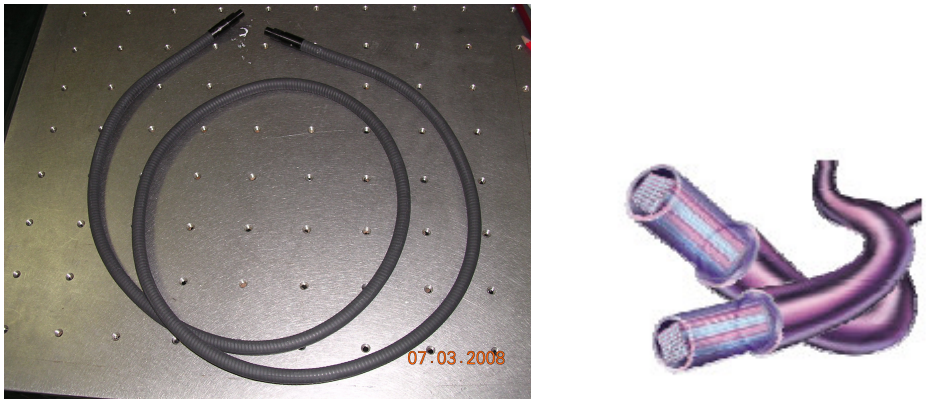

a) b)

Figure 7.4: a) Wound bundle as viewed by a digital camera (1600x1200pixels) b) schematic of the bundle as given by the manufacturer [11]

Subsequently, leached bundles were also investigated. These are manufactured by acid-leaching away the secondary cladding material from the central region of a drawn multifibre rod, leaving rigid sections at each end for mounting the bundle. These bundles have the advantage of an extremely regular, hexagonal arrangement of the component fibres and are more flexible than wound bundles (figure 7.5). They have smaller outer diameters but are generally available in shorter lengths up to a couple of meters. For most OCT applications, this would not be a problem. These bundles have 8μm cores and are assembled in 8μm spacing. It was found that leached fibre bundles are more appropriate for OCT applications due to their regular arrangement of fibres and low cross coupling between the fibres at 1300nm and 1550nm wavelengths. The packaging arrangement of this bundle was also imaged onto a 12 bit digital camera as seen in figure 7.6

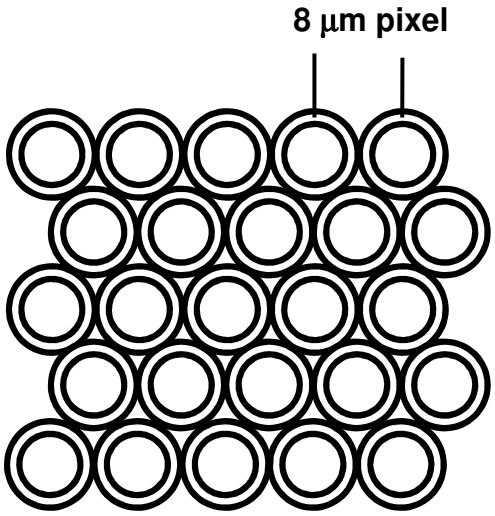

Figure 7.5: Packaging arrangement of leached bundle

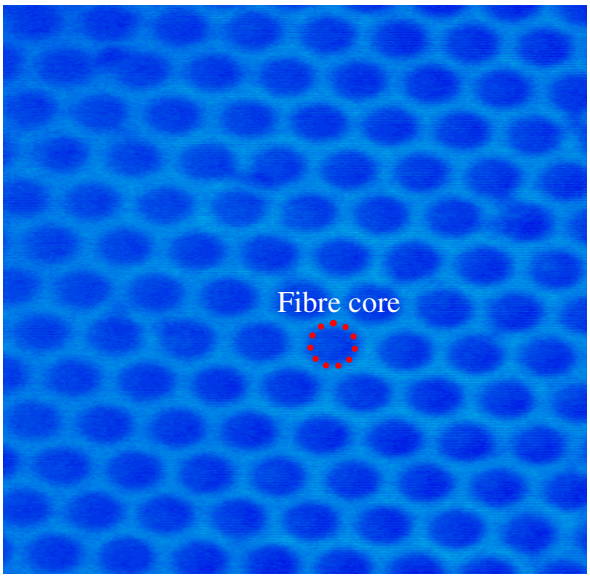

Figure 7.6: Packaging arrangement of leached bundle illuminated by an SLD and projected onto a CCD camera (640x480 pixels)

Image (a) in figure 7.7 shows a leached bundle.

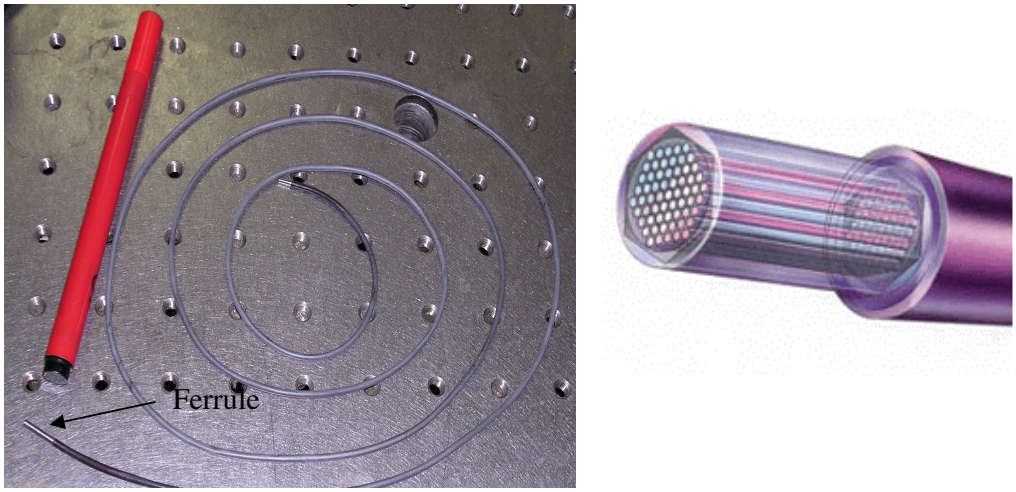

a) b)

Figure 7.7: Leached bundle as viewed by a digital camera (1600x1200 pixels) b) schematic of the bundle as given by the manufacturer [11]

A study of bundle properties at various wavelengths is included in the project. It is important for OCT applications that light should not leak from one fibre to another within the bundle itself. It was attempted to investigate this, by coupling light into a single fibre and observing the output on a camera. At 800 nm, intra-bundle cross-talk appears to be negligible. However, at 1300 and 1550 nm (both wavelengths widely used in OCT), visual examination on an IR sensitive screen suggests that light leakage from fibres within the bundle is more significant for the wound bundle.

Bundle losses are also wavelength dependent. At 800 nm, the transmission is about 45% per metre. The coupling loss is due to the fact that the fibre bundles have high NA (NA=0.55) values and a mismatch is present with the external coupling optics. Careful lens design is therefore required, especially in the probe tip, to find a compromise between the conflicting requirements of efficient coupling and long Rayleigh range. Although transmission loss seems high, lengths of less than 1 metre are sufficient for many applications. The transmission at 1550 nm is lower, at about 20%. This is consistent with a higher mode-field diameter and consequent leakage from the fibres. In future systems, it would be desirable to have the choice of working at the longer wavelengths. Fibre bundles can be obtained specifically for this region, though they are not at present available as part of standard product ranges.

The relatively large fibre diameter can lead to slight multi-moding of light in each fibre at 800nm under certain launching conditions. The consequence of multi-moding in the bundle is that “ghost” images could arise due to the different path lengths corresponding to each mode. Ghosting will then occur only if some of the light couples to a higher order mode, either within the bundle or on recoupling from the probe interferometer to the bundle on the return trip. The effect has not been seen in the present work. Table 7.1 below presents the main characteristics of the bundles investigated.

Table 7. 1: Coherent imaging fibre bundles characteristics

	N.A	Length (m)	Core size (μm)	Spacing (μm)	Diameter (mm)	Flexibility	Number of fibres
Wound Bundle	0.63	1.83	8	10	12.5	poor	90,000
Leached Bundle	0.55	1.35	8	8	3.5	Very good	18,000

The use of coherent imaging bundles in Michelson interferometer based OCT system has once previously been demonstrated successfully for ex-vivo measurements [10]. However, the state of polarization of light varies considerably for light in different fibres of the bundle as this investigation reveals, which, at any one time, will result in non-optimal interference signals for many of the fibres. The set-up used to examine this phenomenon is depicted in figure 7.8. Light emanating from the SLD is collected and collimated by means of an aspheric lens. The collimated beam in turn passes through a crystal polariser which is at a fixed position selecting linear polarisation. The collimated beam after it passes through the crystal polariser is focussed by a second aspheric lens onto one fibre of the leached fibre bundle which is positioned onto a mechanical translation stage. The mechanical stage in turn moves in discrete steps of 8μm selecting each fibre in succession. The beam of light that exits each fibre from the fibre bundle is collected, collimated and focused by another pair of aspheric lenses onto a photodetector. Between the pair of lenses and the detector a polariser is placed that is rotated in 10 degrees increments. As stated above there are a number of reasons why leached bundles are more suitable for this application and for this experiment only the leached bundle was tested. Figure 7.9 illustrates the position of the fibres that were selected and illuminated from an area of the bundle.

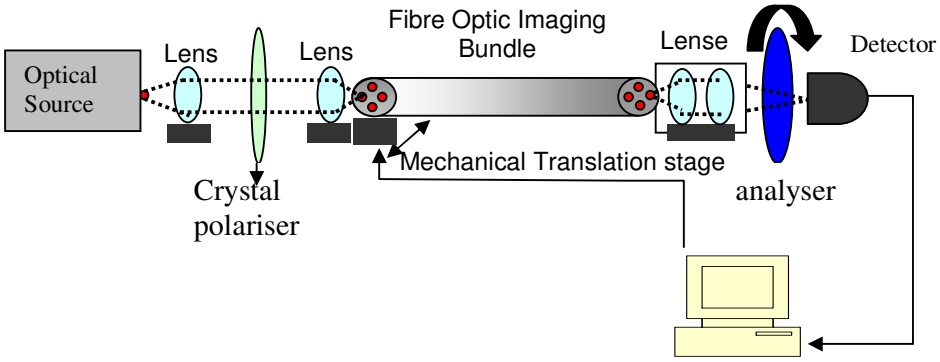

Figure 7.8 : Fibre bundle polarisation test set-up.

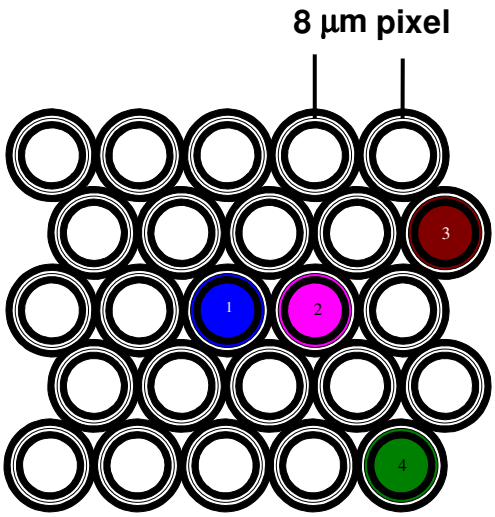

Figure 7.9: Position of the fibres being illuminated, 1-4 individual fibres of the leached bundle.

As can be observed from figure 7.10 the state of polarization of light varies considerably for light in different fibres of the bundle. It can also be noticed that the polarisation of light for neighbouring fibres e.g. fibre 1 and fibre 2 is not substantially different but for fibres like e.g. 3 and 4, which are further away from the first fibre, they have different state of polarisation from fibre 1 and fibre 2.

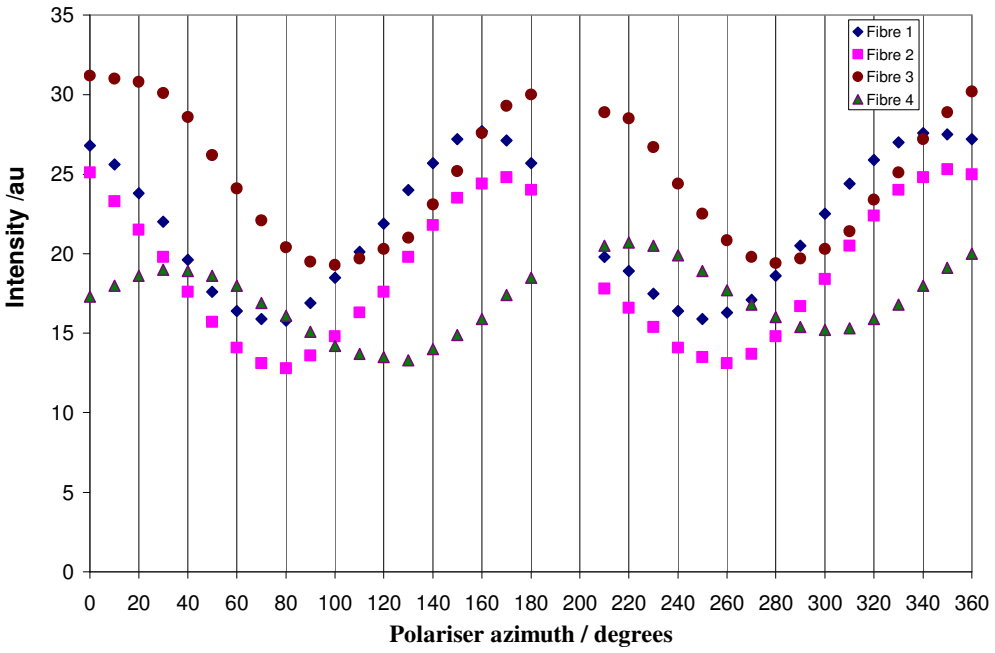

Figure 7.10: Plot of intensity variation in the output from four individual fibres of the bundle, as a polariser is rotated at the output, showing that the state of polarization differs between fibres, Fibres 1-4:individual fibres from an area of the leached bundle

The test was repeated illuminating random fibres within the bundle; the result is shown in figure 7.11. As can be seen, for neighbouring fibres the polarisation doesn't vary enormously but as you move away from the starting fibre, the polarisation state varies quite considerably. It is not easy to see how the polarization of light in each individual fibre can be manipulated. For a Michelson configuration OCT with a single fibre this issue is addressed by incorporating polarisation controllers in the sample arm. For a bundle based OCT system though this is not viable as the bundle contains thousands of fibres and this is not possible to access them individually. Therefore the Fizeau configuration for bundle based OCT systems is more attractive as the bundle does not form part of either interferometer and the instrument is "downlead" insensitive.

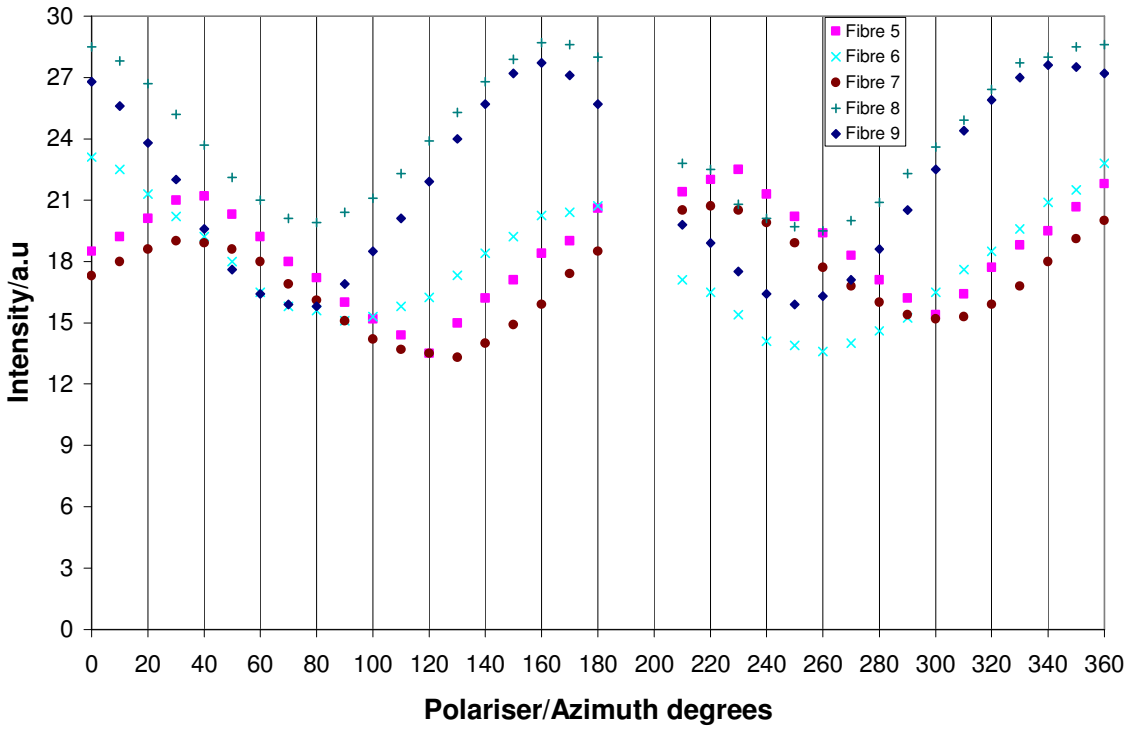

Figure 7.11: Plot of intensity variation in the output from random individual fibres of the bundle, as a polariser is rotated at the output, showing that the state of polarization differs between fibres, fibres 5-9: random individual fibres selected from the leached bundle.

7.2 Implementation

An OCT system based on a Fizeau sensing interferometer and a Michelson balancing/processing interferometer incorporating a coherent fibre imaging bundle will be described in this section. The fibres of the bundle are accessed sequentially by a beam focused onto the input face of the bundle, allowing 2D or 3D images to be acquired using point detection. A Fizeau interferometer configuration is used, in which light from the distal end of a fibre in the bundle (forming the reference arm) mixes with light reflected by the sample itself (forming the sample arm). The use of coherent imaging bundles for OCT beam delivery allows mechanical scanning to be removed from the sample arm, resulting in a passive probe. Such a configuration can form a compact, robust and "downlead insensitive" OCT system. The depth scanning

mechanism is confined within the processing interferometer, external to the sample probe.

Previously an OCT probe incorporating an imaging fibre bundle, in which all fibres of the bundle were illuminated simultaneously, with a CCD camera used for image capture, was demonstrated by *Ford et. al* [12]. The present work describes an alternative methodology, in which each fibre is illuminated in turn, using scanning components at the input to the bundle to address the individual fibres. This system enables point detectors to be used instead of a camera, allowing high-bandwidth noise filtering techniques to be applied to the detector output.

The experimental arrangement for the OCT system is described below and is illustrated in figure 7.13. It is a bundle-based analogue of the single-point version. For this configuration another SLD source was identified and purchased from *Superlumdiodes* (*Superlum broadlighter D830).* This source was extremely sensitive to backreflections and optical feedback could damage the SLD, thus this source was also purchased with an inbuilt optical isolator in order run it safely at full power.

Light emanating from the SLD is fibre coupled into a single mode fibre and outputs 12mW of power at 830nm. The coherence length of this source was 9.86μm. One end of a single mode fibre patch cord is attached to the SLD and the other end is mounted onto a micro translation stage. Light exiting the fibre is collimated, using an aspheric lens (*Thorlabs C570 TM-B, aperture 4mm, focal length 2.84mm, NA 0.67, broadband AR coating 600-1050nm)* ensuring diffraction limited performance. The molded glass asheres are mounted in a stainless steel lens cell. Figure7.12 depicts such a lens

Figure 7.12: Aspheric lens [13]

The collimated beam is focused onto the input face of the bundle, by means of a second aspheric lens (*Thorlabs C220 TM-B, aperture 5.5mm, focal length 11mm, NA 0.25, broadband AR coating 600-1050nm)* providing a focused beam diameter of 4.4µm. Figure 7.14 illustrates that the major part of the light (90%-intensity measurement) is coupled into one fibre of the bundle as viewed by a camera at the output end.

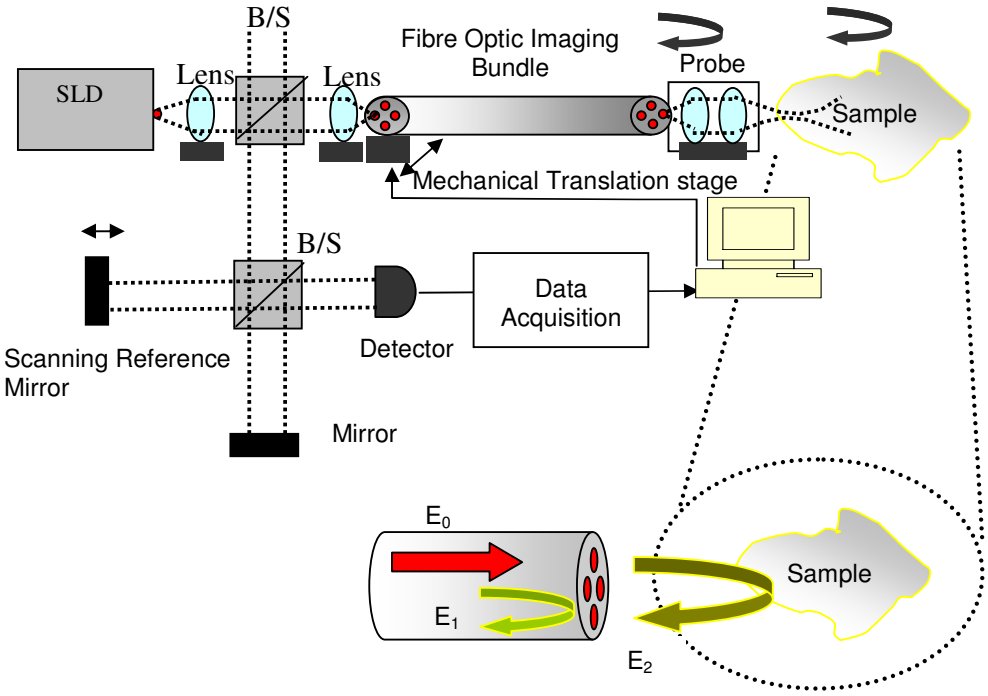

Figure 7.13: Fibre bundle based OCT system, B/S: beamsplitter, E_0, E_1, E_2: Electric fields

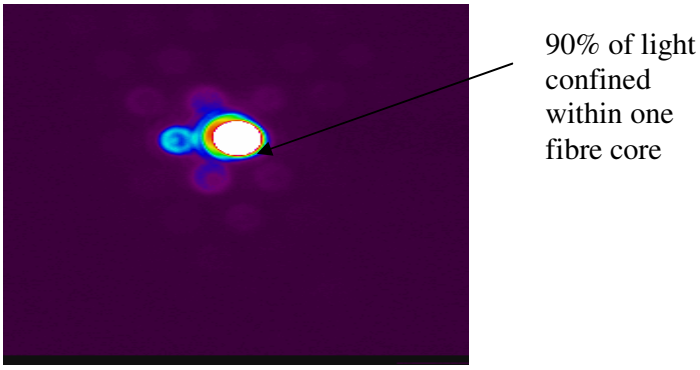

Figure 7.14: Coupling to a single fibre (640x480)

The input end of the bundle was polished at an angle of 8 degrees to avoid any back reflection to the processing interferometer. The bundle used was a leached coherent fibre optic imaging bundle with a length of 1.35m, N.A.= 0.55 and comprising 18,000 individual fibres. Light was transmitted by the bundle to a probe head comprising a pair of matched lenses positioned in a unit magnification, 4f imaging arrangement. The beam was transmitted through the bundle and focused onto the sample by the probe lenses.

If the beam waist diameter exceeds the fibre spacing, overlap gives rise to inter-fibre cross-talk in light scattered by the sample. Non-reciprocal imaging can occur, in which backscattered light transmitted to the sample by one fibre can be collected by a different fibre. Even if beam waists are well separated at best focus, cross-talk will arise outside the Rayleigh range as the beams diverge. Since the path length in the Fizeau interferometer varies depending on which pair of neighbouring fibres are involved, spurious sets of interference fringes can arise at the detector. The consequences again are the appearance of 'ghost' features, causing blurring of interfaces in the OCT image and degradation of both depth (z) and x–y resolution

Prior to aspherics lenses, achromat lenses were used which resulted in a significant improvement when compared to microscope objectives, although their ability to minimize aberrations is known to decrease for off-axis object points. Aspherics performed better still. By choosing an appropriate aperture diameter for our system, focusing quality with aspherics confined about 90% of the incident power to a single fibre, with about 1–2% in each of the neighbouring fibres. Thus lens systems introduced to the OCT system comprised of appropriate aspherics lenses (*Thorlabs C230 TM-B, focal length 4.5, NA 0.55 & Thorlabs C260 TM-B focal length 15.29mm, NA 0.16,)*. Both these aspheric lenses were antireflection coated from 600nm to 1050nm. The sample beam is focused with a beam diameter of about 8.2μm and a Rayleigh range of about 251μm. The system of lenses comprising the probe head are shown in figure 7.15. The aspherics lenses were mounted into an RMS thread block and the block was attached onto a five axis manual translation stage to allow for best alignment.

A bulk-optic processing interferometer is preferred to avoid reintroducing polarization problems and to minimize dispersion. To address each fibre in the bundle

in succession, the bundle was mounted onto a computer controlled mechanical translation stage (Phyisk Intstrumente M-110.1DG), which was scanned across the focused input beam.

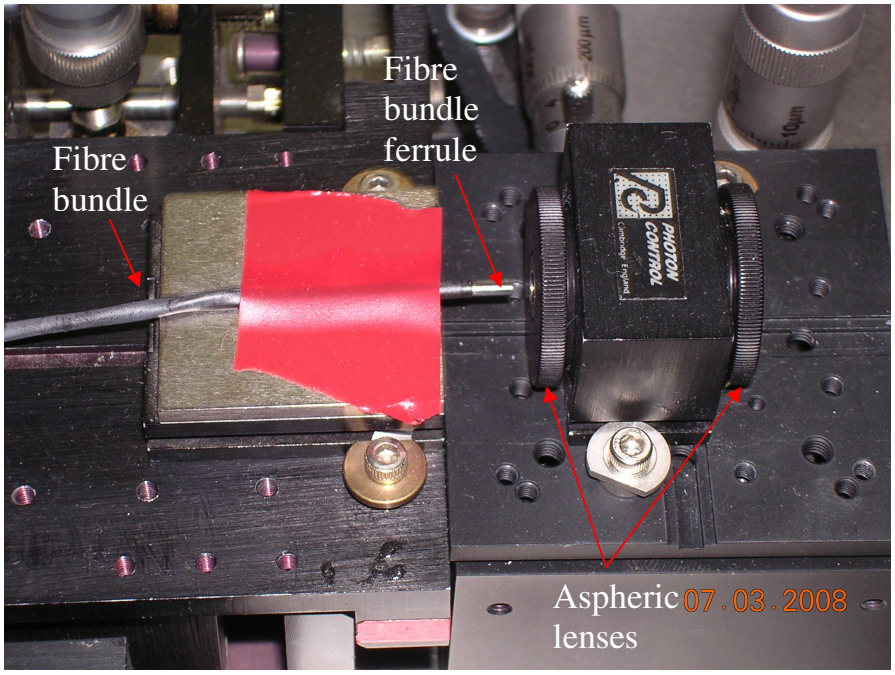

Figure 7.15 : Aspheric lenses at the probe head

Figure 7.16 depicts the system set-up.

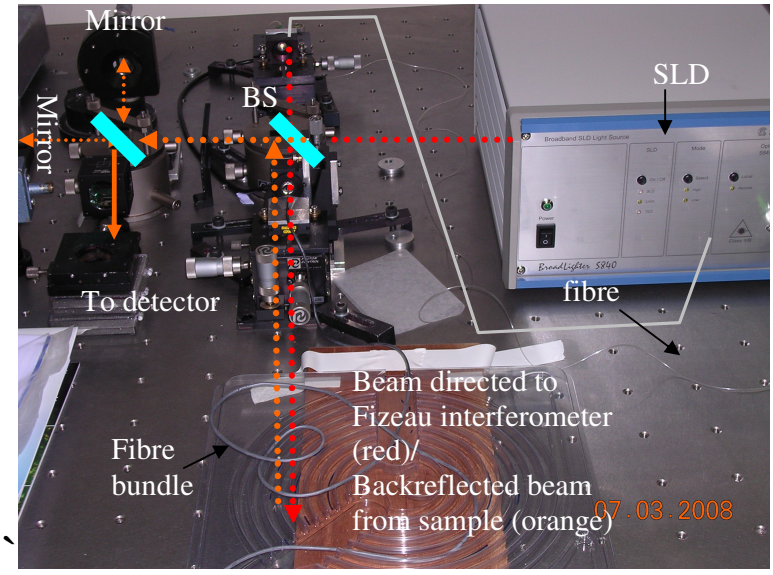

Figure 7.16: System set-up, BS: beamsplitter

7.3 Experimental Results

The two beams from the Michelson interferometer recombine at the InGaAs photodetector which has peak sensitivity at 820nm and is digitised using a 200,000 samples/ sec, 16-bit A/D card housed within a PC. The voltage range on the DAQ card was readjusted manually in order to achieve maximum range sensitivity and accuracy of the acquired OCT signal.

With the stage in the receiving interferomter scanning at 1 mm/sec, the frequency of the OCT fringes acquired by the photodetector was about 2 kHz. The DC background was first removed by passing this signal through an analogue high-pass filter with a cut off of a few Hz. A gain in the range 100-1000 was then applied, to obtain a signal in the appropriate voltage range for digitisation. Following amplification, the signal was rectified, which is achieved by taking the absolute values of the voltage. The envelope width of about 10μm is unchanged by rectification. Application of a low-pass filter, following rectification, removes the carrier fringes leaving only the envelope. Care must clearly be taken over the filter functions chosen, to minimise distortion or attenuation of the envelope signal. In our system, second-order Butterworth filters were found to give the best performance. A similar procedure as described in Chapter 6 is followed.

An A-scan was obtained when a single fibre in the bundle was illuminated and a mirror was used as a sample producing a coherence function with a FWHM value of 10 μm in air which closely agrees with theoretical estimated value of 9.86μm. The A-scan image of the system with a mirror as a sample is illustrated in figure 7.17. Figure 7.17 also depicts the high pass filtered signal and the low pass filtered/rectified signal obtained from the sample mirror. Using the same procedure as in chapter 6 the SNR obtained from a mirror surface in the sample arm after filtering was measured to be 60dB.

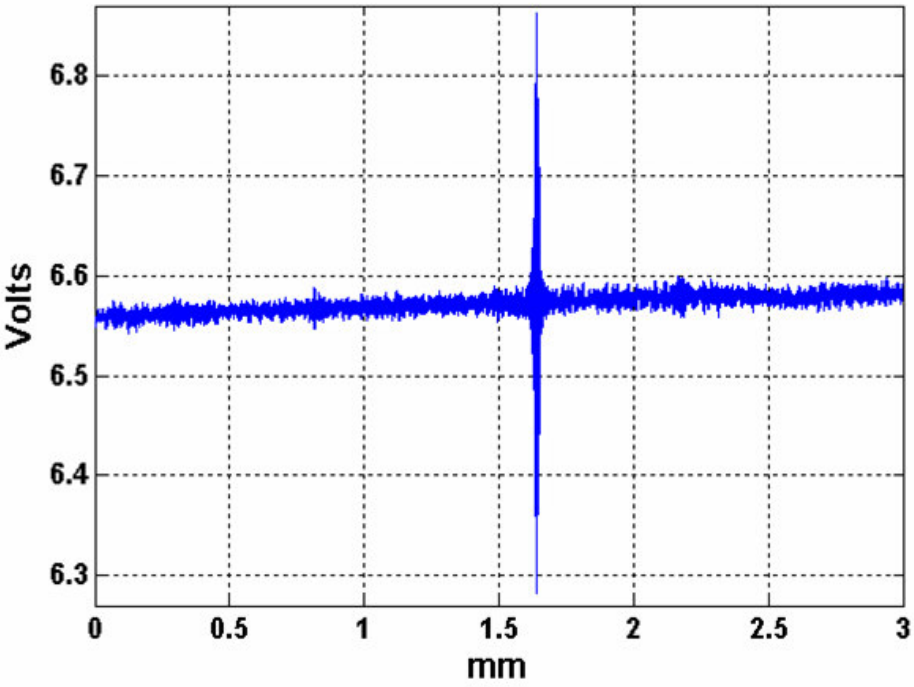
Volts
6.8
6.7
6.6
6.5
6.4
6.3
0
0.5
1
1.5
2
2.5
3
mm

a)

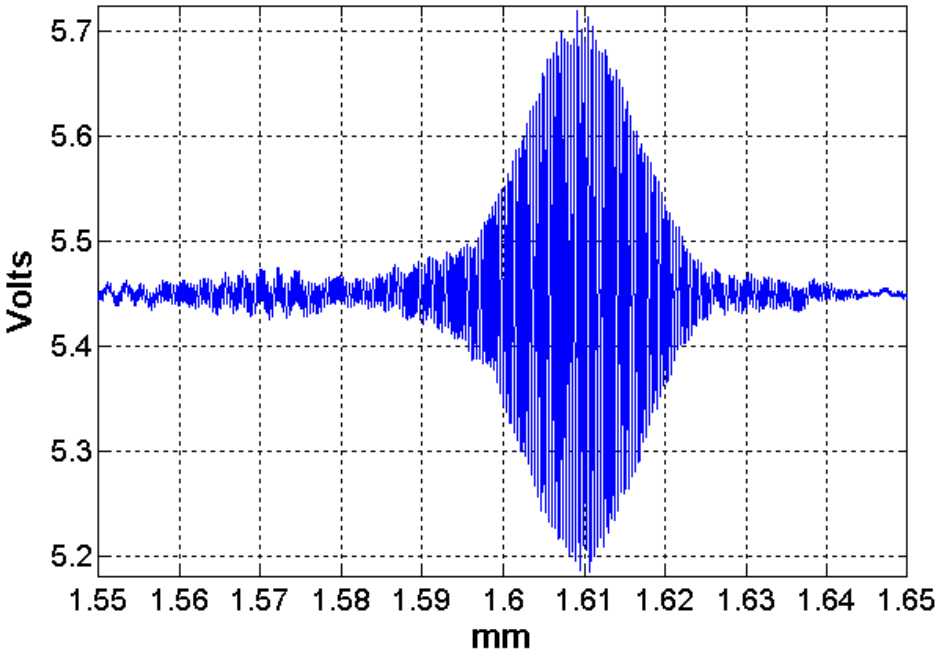
Volts
5.7
5.6
5.5
5.4
5.3
5.2
1.55
1.56
1.57
1.58
1.59
1.6
1.61
1.62
1.63
1.64
1.65
mm

b)

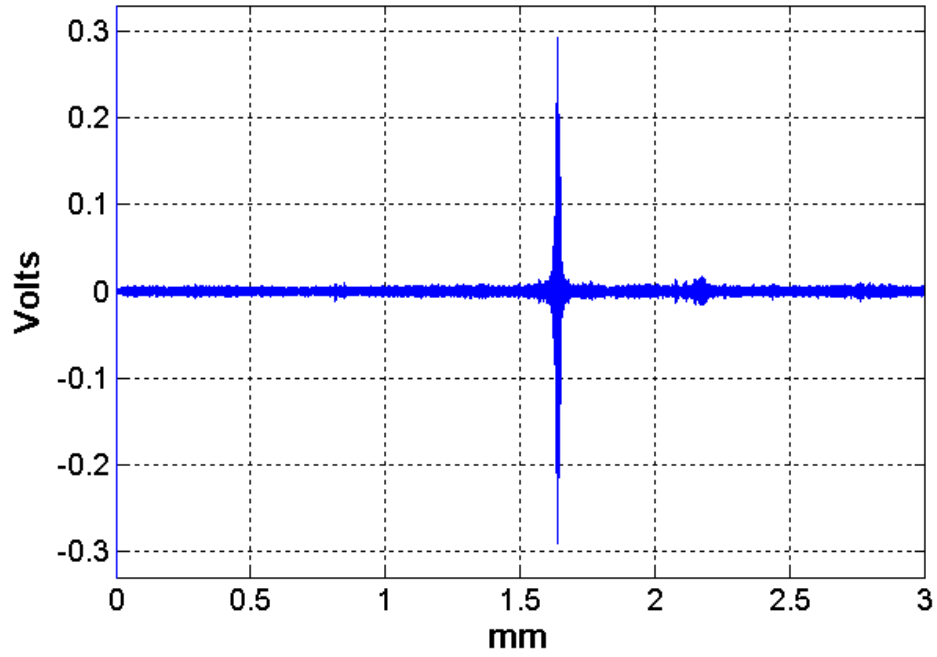

c)

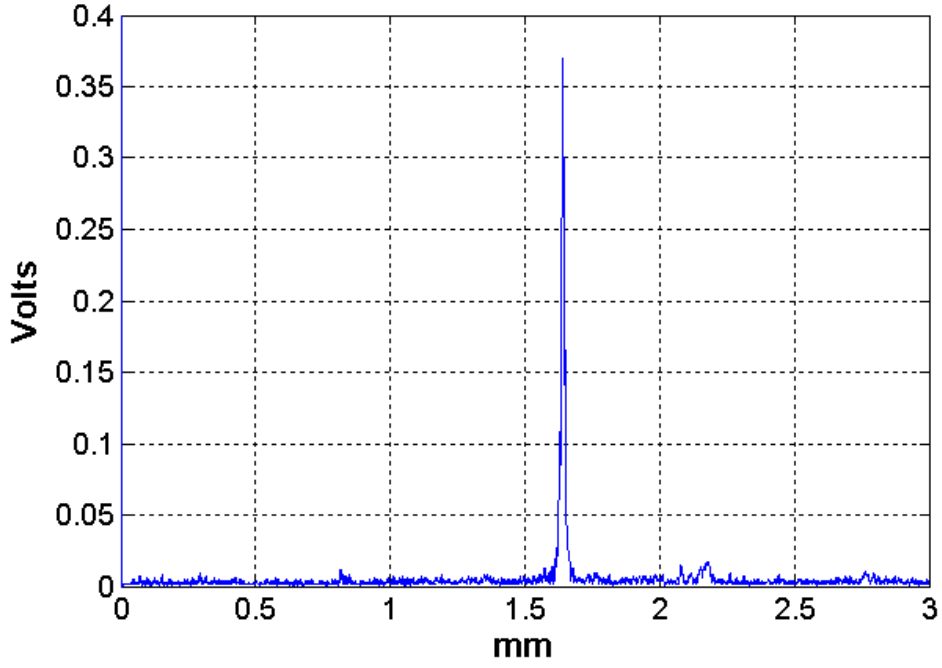

d)

Figure 7.17: a) Unfiltered OCT signal obtained from a mirror sample b)zoomed version of a. c) High pass filtered signal d)Low pass/rectified signal

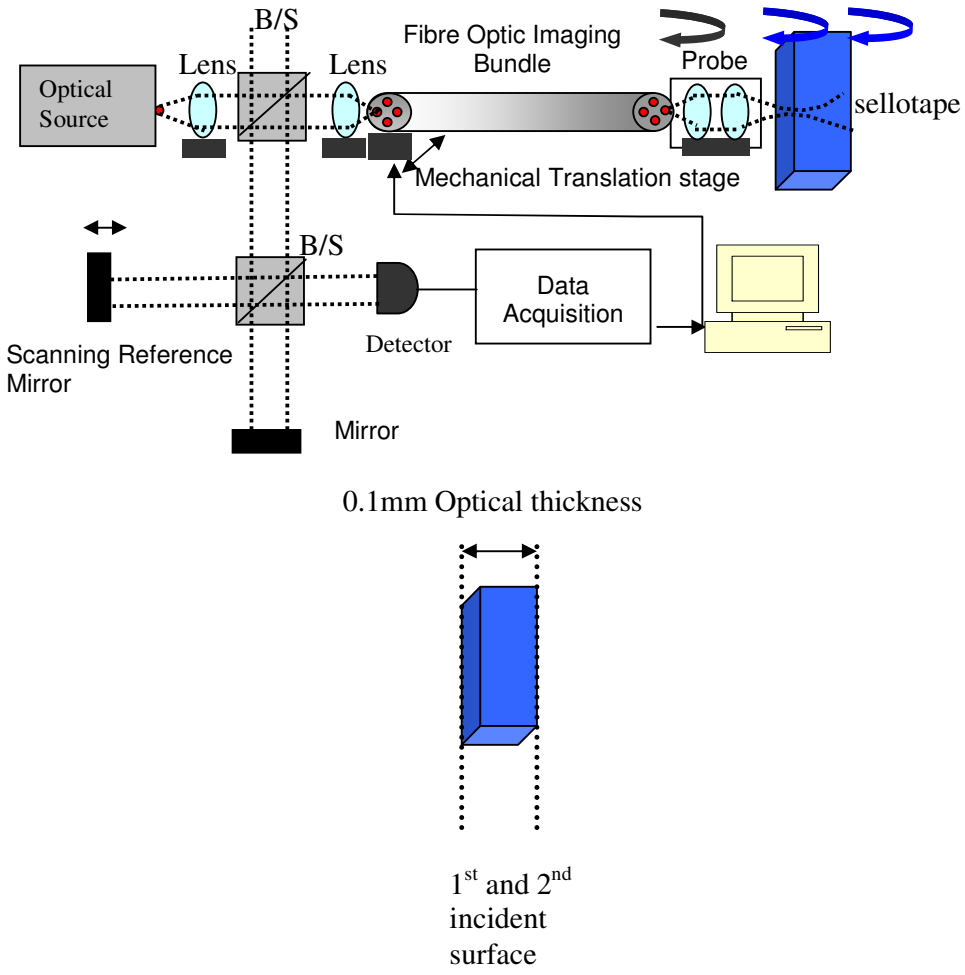

Figure 7.18: Configuration set-up with sellotape as a sample, B/S:beamsplitter

A sample of sellotape was also used as laboratory sample. The sellotape was placed at the focus point of the probe and an A-scan image was produced. The configuration set-up is shown in figure 7.18. The A-scan image produced is shown in figure 7.19 revealing the top surface and the bottom surface of the sellotape 0.1mm apart (optical thickness). The first peak which corresponds to the top surface of the sellotape had higher amplitude than the second as expected.

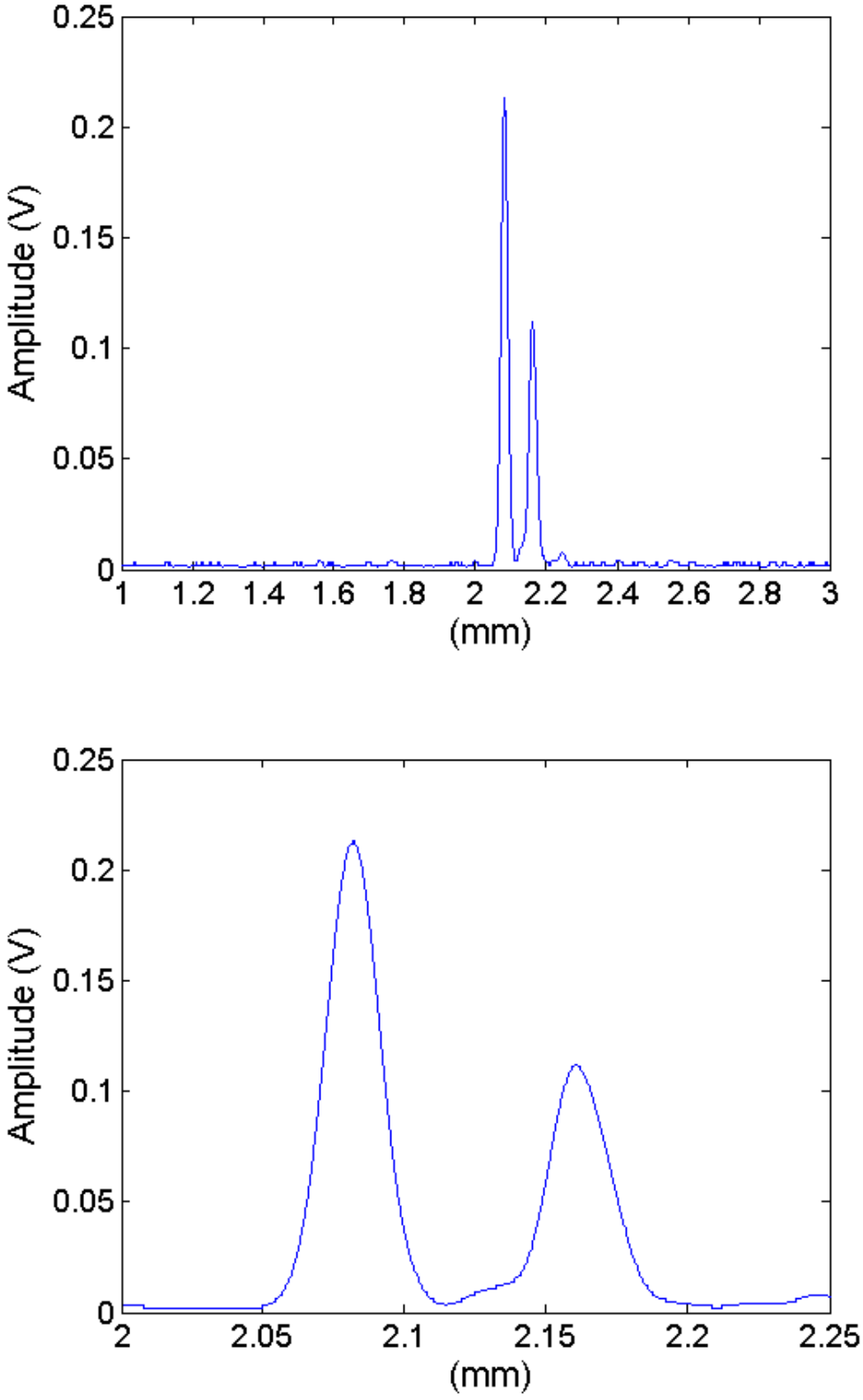

Figure 7.19: A-scan image from sellotape sample when one fibre is illuminated (filter/rectified signal).

Furthermore as for the single point Fizeau interferometer based OCT system a brown dry onion was used as a sample. The whole onion was placed onto a mount and was placed at the focused point of the sample beam. The onion is a biological sample as water and other minerals that absorb light are also found in human samples. The multilayer structure of the thin dry brown layers of the onion can be seen in figure 7.20. The optical thicknesses of the onion layers are in the same range ~45μm as previously measured in chapter 6.

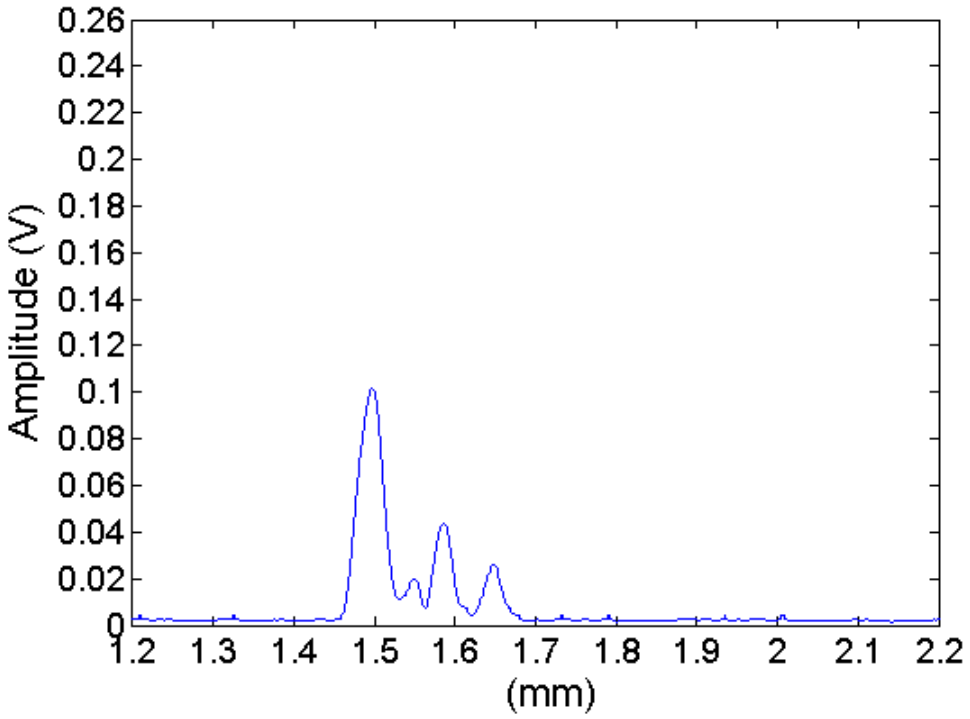

Figure 7.20: A-scan image of a brown dry onion skin (filtered/rectified signal).

For a 2D image several fibres of the bundle must be scanned acquiring multiple A-scan refractive index profiles. Figure 7.21 shows images of 3 individual fibres being illuminated in succession in 8μm steps (x direction).

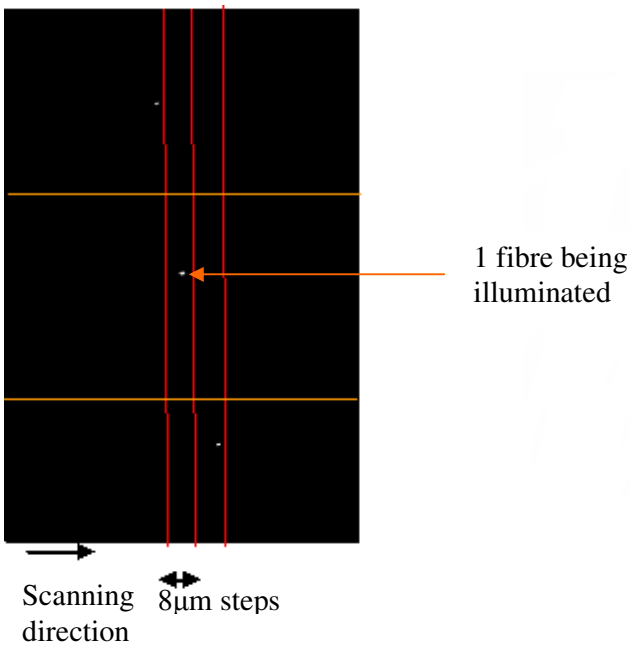

Figure 7.21 : Three consecutive images, from three fibres illuminated in sequence, by scanning of the input beam across the face of the bundle

The first ever captured and reported two-dimensional image for an OCT configuration as shown in figure 7.18 is exhibited. The sample that was imaged was composed from two pieces of plastic projector slides stacked together as shown in figure 7.22. A-scan images were taken at each step position to construct an image of 0.16mm (transverse) x1mm (depth) with a pixel size of 8µm.

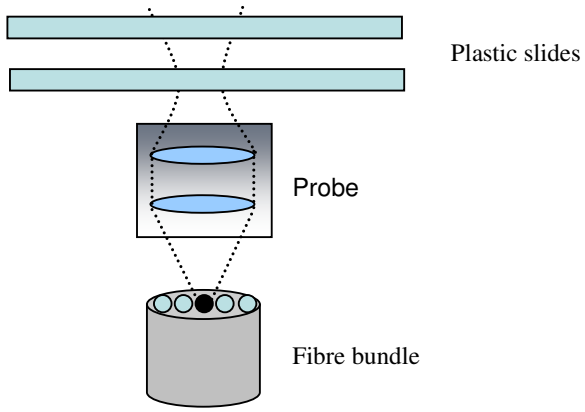

Figure 7.22: Arrangement of the fibre bundle, probe and a sample of two plastic projector slides.

The image produced is shown in figure 7.23. Twenty individual fibres were scanned linearly across the bundle. The image produced after processing clearly depicts the four layers of the sample. The upper and lower surfaces of the plastic slides are clearly visible with an overall thickness of 0.15 ± 0.007 mm for both slides. The air gap between them was found to be 0.47 ± 0.007 mm

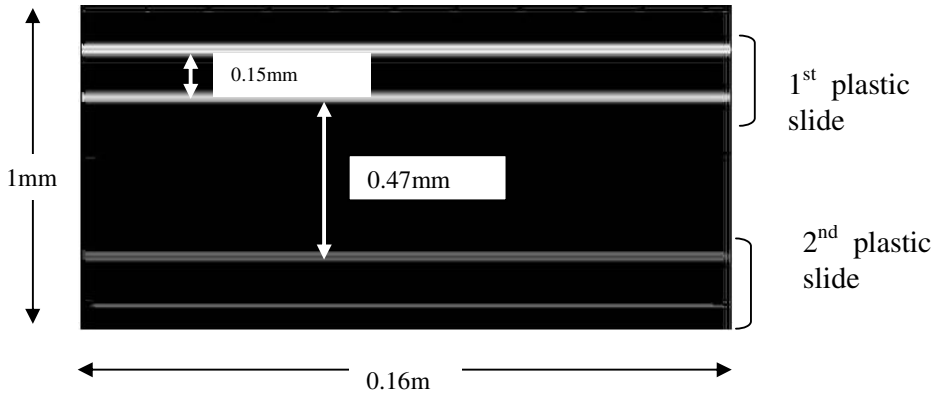

Figure 7.23: First reported 2D image from a sample composed of two layers of plastic projector slides captured from a Fizeau interferometer based OCT incorporating a coherent imaging bundle

The environmental downlead insensitivity of the system was also tested, as the fibre bundle was twisted and heated with a hair dryer during measurement and the signal visibility remained unaffected. The LabView™ program, as for the previous configuration in Chapter 6, calculated the SNR as ~60dB from 30 scans by taking an average value of the peak amplitude and an average of the standard deviation from the noise floor.

Furthermore, in order to minimize polarisation fading, the optics in the beam path, e.g. beamsplitters, were purchased to transmit both polarisations equally, so that the randomly polarised signal is conveyed with minimal fluctuations as the polarization varies.

7.4 Discussion

This chapter has outlined the implementation procedures and challenges faced in constructing a time domain Fizeau interferometer based OCT system incorporating a coherent fibre optic imaging bundle. This is the first reported system with such a configuration producing several A-scan images and the first reported 2D image from a laboratory sample. The current art would be beneficial for endoscopic operation as downlead sensitivity is maintained and a compact, robust endoscope tip is formed without the need of any scanning mechanical parts incorporated into it.

Although the current system is constructed in the time-domain it would also be possible to operate the system as a Fourier-domain instrument thus eliminating the depth scanning mechanism and increasing the speed of operation [13]. The Fourier domain systems would exhibit increased scanning speed thus eliminating any artefacts that could arise during endoscopy by the movement of the sample. The approach in constructing such a system would be to fix the path-length in the processing interferometer and to disperse the output signal onto a spectrometer. This inevitably leads to a relatively large DC background, and it might appear preferable to dispense with the processing interferometer altogether. However, the path-length inherent to the Fizeau interferometer is generally too large to allow Fourier-domain operation in this mode, unless an external reflector is used to generate the reference reflection as also described in Chapter 6. Another possible solution would be the implementation of a swept source [14] providing the advantages that were discussed in chapter 5.

One more complexity that could be encountered during endoscopy with a bundle based OCT system is that the magnification of features may change as a function of distance from the focusing lens at the end of the bundle. Thus it may be tricky to determine the size of a feature from a sample. This is due to the fact that its size may depend on the distance of the probe to the features being imaged. Since feature size of a scanned area could have diagnostic value it would be preferable to eliminate this issue. One solution is to calibrate the system using a known sample.

Since the current technology provides information about the distance to surfaces and features of the sample, this helps in gauging the distance to features and consequently to the scale. On the other hand, the focusing lens system on a bundle based OCT system can be constructed to image the end of the fibre bundle telecentrically into the sample thus making the image almost scale-invariant with range from the lens. The telecentric system of lenses could be formed with two converging lenses arranged as in a Keplerian telescope.

Another approach in forming a Fizeau based interferometer incorporating a fibre bundle would be to place a glass window or microscope cover slip on top of the sample to provide the reference reflection. If this reflecting surface (glass window, microscope cover slip) is positioned to be in contact with the sample this could lead to an additional advantage of the system as there is no need for a processing interferometer if a swept source is also incorporated. This is true as any motions of the sample could be partially compensated because the phase fluctuation caused by motions of the sample will be cancelled by the common motion of the reference surface. Optical coatings can then be applied to the reference reflecting surface to control the magnitude of the reflection in order to produce the desirable ratio between reference and sample signal. Such a coating could be for example titanium dioxide as also mentioned in Chapter 5.

References

1. Huang D, Swanson E. A., Lin C. P., Schuman J. S, Stinson W. G., Chang W., Hee M. R., Flotte T., Gregory K., Pualifito C. A., Fujimoto J. G, *Optical coherence tomography,* Science, Vol. 254, 1991, pp1178-1181

2. Izatt J A, Kulkarni M D, Wang H-W, Kobayashi K and Sivak M V Jr.**,** *Optical coherence tomography and microscopy in gastrointestinal tissues*, IEEE Journal of Selected topics in quantum electronics, Vol. 2, 1996, pp 1017-28.

3. Li X., Chudoba C., Ko T., Pitris C., Fujimoto J. G., *Imaging needle for optical coherence tomography*, Optics Letters, Vol. 25, 2000, pp1520-1522.

4. Tran P. H.**,** Mukai D. S.**,** Brenner M.**,** Chen Z., *In vivo endoscopic optical coherence tomography by use of a rotational microelectromechanical system probe,* Optics Letters, Vol. 29, Issue 11, 2004, pp.1236-1238**.**

5. Herz P., Chen Y., Aguirre A., Fujimoto J.G., Mashimo M., Schmitt J., A, Koski A., Goodnow J., Petersen C.,*Ultrahigh resolution optical biopsy with endoscopic optical coherence tomography,* Optics Express, Vol. 12, Issue 15, 2004, pp.3532-3542**.**

6. Xie T., Xie H., Fedder G. K., Pan Y., *Endoscopic Optical Coherence tomography with a modified microelectromechanical systems mirror for detection of bladder Cancers,* Applied Optics, Vol. 42, Issue 31, 2003, pp.6422-6426.

7. Lau W. Y., Leow C. K., Li A. K. C., *History of Endoscopic and Laparoscopic Surgery,* World journal of surgery, Vol. 21, No. 4, 1997, pp444-453

8. Juskaitis R., Wilson T., Watson T. F., *Real-Time white light reflection confocal microscopy using a fibre optic bundle,* Scanning, Vol. 19, 1997, pp15-19.

9. Yelin D., Rizvi I., White W. M., Motz J.T., Hasan T., Bouma B. E., Tearney G. J., *Three dimensional miniature endoscopy,* Nature, Vol. 446, 2006, pp765-770.

10. Xie T., Mukai D., Guo S., Brenner M., Chen Z., *Fiber-optic-bundle-based optical coherence tomography,* Optics Letters, Vol. 30, No. 14, 2005, pp1803-1805.

11. http://www.schott.com [14/11/2005]

12. Ford H. D., Tatam R. P., *Fibre imaging bundles for full field optical coherence tomography,* Measurement science and technology, Vol. 18, 2007, pp2949-2957.

13. http://www.thorlabs.com [21/04/2007]

14. Wojtkowski M., Srinivasan V., Ko T., Fujimoto J.G., Kowalczyk A., Duker J., *Ultrahigh-resolution, high-speed, Fourier domain optical coherence tomography and methods for dispersion compensation*, Optics Express, Vol. 12, Issue 11, 2004,pp2404-2422

15. Vergnole S., Lamouche G., Dufour M., Gauthier B.,*Common path swept-source OCT interferometer with artifact removal,* Proceedings of SPIE, Vol. 6847, 2008.

Chapter 8

CONCLUSIONS AND FUTURE WORK

8.1 Introduction

OCT is now an established imaging technology enabling the visualization of tissue microstructure in situ and in real time [1, 2] with resolutions in the 1-10 μm [3] range at depths of 1-2mm [4]. Clinical OCT systems that use superluminescent diodes (SLDs) enable imaging with 8-15μm axial resolution. As stated in previous chapters for higher axial resolutions other sources could be used like Cr^{4+}forsterite laser [5], Ti:Sapphire laser [6], swept sources [7] etc that offer much higher bandwidths. Previous studies have demonstrated that changes in tissue architectural morphology associated with neoplasia can be identified in their early development with an OCT imaging system [8-10]. With state of the art OCT imaging equipment individual cells within the epithelial layer and the sub-mucosa layers can be imaged and any

cancerous changes identified. Many epithelial cancers are preceded by pre-malignant changes, such as dysplasia [11]. Different parts of the human body show different morphological characteristics for dysplasia or carcinoma in situ tissue [11]. In the bronchial region for example carcinoma in situ increases the epithelium layer thickness from 50μm to 120μm [11].

Epithelial cancers of the gastrointestinal tract, reproductive tract, and the respiratory tract comprise the majority of cancers encountered in internal medicine [11]. Conventional screening methods often rely on the gross morphological characteristics of tissues. Biopsy and histopathology is the standard for the diagnosis of dysplasia or carcinoma, but can suffer from sampling errors and is cumbersome for screening and surveillance applications. Our hypothesis is that OCT can function as a form of "optical biopsy" which can perform microstructural imaging of tissue morphology in situ without excision. This technology could assist in minimising the need of surgical operations and biopsies being performed to identify tissue morphological changes such as carcinomas.

8.2 Summary

This chapter will provide a synopsis of the work presented in this thesis. Further sections will exhibit the conclusions drawn from this research and will discuss future avenues of exploration for the current art.

Chapter 1 introduced the OCT technology as a medical imaging technique outlining its capabilities and limitations. It also described current challenges faced by the technology and how this can be assessed with current research work.

Chapter 2 discussed the various medical imaging techniques currently in use. It provided a comparison of these techniques with the OCT technology and stated the reason for the necessity of such an imaging instrument in a clinical environment.

Chapter 3 described the theory and the fundamentals behind the technology and stated the advantages provided with a Fizeau interferometer based OCT system in comparison to the standard Michelson interferometer based OCT. This chapter also described the mathematical analysis of the SNR for the system researched.

Chapter 4 discussed the applications of the OCT technology and provided a historical review from the invention of the technology to up to date advancements.

Chapter 5 provided an instrumentation review for OCT systems, highlighted the most important aspects such as scanning speeds, methods of scanning and sources. It also stated the parameters that affect the performance of the current technology and examined the current configurations used for endoscopic operations.

Chapter 6 described and analysed the challenges during construction of a time domain Fizeau interferometer based OCT. It also detailed the experimental procedures followed for the SNR experimental analysis, optical source characterisation and lens design. It demonstrated various A-scan images for biological and non-biological samples. The system constructed achieved an experimental SNR of ~80dB being unaffected by temperature fluctuations and fibre bending thus verifying its potential use for endoscopic operations.

Chapter 7 also detailed the experimental work carried out on an OCT instrument based on a Fizeau sensing interferometer and a balancing/processing Michelson interferometer incorporating a coherent fibre optic imaging bundle. The properties of the bundles used were described and experimentally verified. The first reported A-scan images and 2D images using this technology were reported in this chapter.

8.3 Conclusions

One drawback of the current OCT technology based on a fibre Michelson interferometer is that it is susceptible to signal fading. Twisting, bending, or stretching

fibres can induce birefringence into the fibres so that the polarization of the signal is altered during propagation through the fibre. Since separate reference and sample arms are used in a Michelson interferometer, the polarizations introduced into both signals may not be the same. If the sample and reference signal have orthogonal polarizations that would result in a complete signal loss. Hence as the fibre in the sample is to be moved during an endoscopic operation the polarization of the sample signal may change causing variations in the magnitude of the interference signal called polarization fading. Although this issue could be addressed by incorporating polarisation state controller to the sample arm this increases the complexity and the cost of the instrument. There are other factors within the OCT technology that may change the state of polarisation of light within the sample arm such as scattering of tissue and tissue birefringence. The uncertainty though of polarisation fading due to optical fibres being twisted or stretched as chapter 5 explained is to give the greatest decrease in signal.

However, by using a common path interferometer like the Fizeau interferometer as proposed in this work, any random polarization changes introduced by the fibre will be common to the reference and sample signals and therefore the interference between the two is preserved without the need of polarisation state controllers. Due to benefits offered by the Fizeau interferometer a time-domain OCT based on such configuration was investigated and constructed in the laboratory. The system constructed had a transverse resolution of 23μm in air and a Rayleigh range of 540μm. The axial resolution was 18.8μm, sufficient enough to image epithelial tissue. With the stage scanning at 1 mm/s., the frequency of the OCT fringes acquired by the photodetector was about 1.3 kHz. The DC background was first removed by passing this signal through an analogue high-pass filter with a cut off of a few Hz. A gain in the range 100-1000 was then applied, to obtain a signal in the appropriate voltage range for digitisation. Following amplification, the signal was rectified, which is achieved by taking the absolute values of the carrier fringes.

The coherence envelope of the source was obtained using a mirror as a sample and recorded an SNR of ~80dB. The sensitivity of the system was assessed using Cargille oils of extremely well calibrated refractive index (1.42-1.55), deposited on a glass microscope slide of 1 mm thickness. This test was carried out to artificially

simulate the light reflections to be seen from human tissue. Differences in RI (refractive index) between regions within a biological sample tend to be in the second or third decimal place. The results from the oil measurements suggest that the SNR obtained from our system is sufficient for good-quality imaging from samples with this level of RI variation and for ex-vivo human skin samples Although the Michelson based OCT system report a higher SNR (~100dB/mirror sample), in an endoscopic operation the movement and stretching of fibres will affect the interferometric signal thus producing a lower SNR than a Fizeau based system. Therefore to achieve a comparison of the SNR for the two systems requires them to be configured and operated in a surgical setting.

Another issue addressed by this work is the 2D or 3D imaging capabilities or limitations of current reported OCT endoscopes. Current ex-vivo OCT systems construct 2D images by delivering a focused beam of a few microns to the sample and acquiring multiple sets of data as this beam is scanned across the area of interest. This is frequently achieved by using a small moving mirror to scan the beam rapidly across the sample. However for in-vivo deployment it is understood that dimension is a limiting factor as everything must be miniaturised. Previous endoscope OCT configurations as detailed in chapter 5 used movable parts such as microelectromechanical systems (MEMS) micromotors, (MEMS) mirrors, rotary fiber joints or linear motors. The construction of such scanning systems for use inside the body is a tedious task, as electrical power must be delivered to the endoscope tip to drive the scanner and the whole system must be miniaturised to fit inside an endoscope. Since miniaturisation is necessary the mirror size and numerical aperture are limited by the endoscope size thus the lateral resolution of the system is subsequently restricted. One more limitation when using (MEMS) based probes is the sweep distances obtainable could be limited due to the confined spaces of the endoscopic probe. These limitations were addressed by the current work with the incorporation of a coherent fibre optic imaging bundle to an OCT system forming a compact and robust probe without the need of mechanical scanning parts at the probe tip and electricity to drive them.

Mechanical scanning is now required only in the part of the system external to the body, reducing the complexity of the probe. Light from the source was used to

illuminate each fibre in rapid succession effectively treating the bundle as a multiplexing element. The two bundles examined in this work were provided by *Schott Inc.*

Bundle properties at various wavelengths were presented in this work. At 800 nm, intra-bundle cross-talk appears to be negligible as this work explained. However, at 1300 and 1550 nm (both wavelengths widely used in OCT), visual examination on an IR sensitive screen suggests that light leakage from fibres within the bundle is more significant.

Bundle losses are also wavelength dependent. At 800 nm, the transmission is about 45% per metre. The high coupling loss observed in this work is due to the fact that the fibre bundles have high NA (NA=0.55) values and a mismatch is present with the external coupling optics. Although this seems high, lengths of less than 1 metre are sufficient for many applications. The transmission at 1550 nm is lower, at about 20%. This is consistent with a higher mode-field diameter and consequent leakage from the fibres. In future systems, it would be desirable to have the choice of working at the longer wavelengths. Fibre bundles can be obtained specifically for this region, though they are not at present available as part of standard product ranges.

This work also addressed the polarisation properties of the fibre bundles. As was exhibited in chapter 7, the state of polarization of light varies considerably for light in different fibres of the bundle which, at any one time, will result in non-optimal interference signals for many of the fibres. However it was not easy to see how the polarization of light in each individual fibre can be manipulated. As this investigation revealed the Fizeau interferometer configuration for an OCT system would be a more suitable approach when coherent fibre optic imaging bundles are to be incorporated.

This work presented the first reported system with such a configuration. Several A-scan images were generated and the first reported 2D image from a lab sample was exhibited. The current art would be beneficial for endoscopic operation as downlead sensitivity is maintained and a compact, robust endoscope tip is formed without the need of any scanning mechanical parts incorporated into it.

8.4 Future Work

In this section practical improvements to the current fibre bundle based OCT system are to be presented followed by some more general ideas and thoughts arising from this research work.

Fibre bundle scanning mechanisms: In this work the bundle was scanned in the X direction at a low speed to prove the working principle accessing only 20 fibres. A future improvement would be the investigation of the mechanisms required to address the whole area of the bundle at high speed. One solution to that would be the incorporation of an ultra long range tip/tilt mirror (S-334.2SL) provided by PI (Physik Instrumente). This unit is capable of scanning the focused beam onto the input end of the fibre bundle at a few tens of hertz (50Hz-60Hz) with high accuracy in both X and Y directions. Another advantage of this unit is that both the scanning axes are fixed to a common pivot. The S-334 is equipped with two pairs of piezo drives operating as a unit in push/pull mode. The S-334 also provides sub-microradian resolution if operated in closed-loop mode (servo loop control-position sensor). For the unit to run in a closed loop mode it is equipped with a high resolution full bridge strain gauge sensor calibrated specifically for this unit. This unit offers absolute position control and high linearity, typically under ±0.25% over the entire travel range.

One more available solution to address the whole area of the bundle is to use a pair of galvanometer scanners that will offer higher scanning speeds of the beam onto the input end of the bundle than the piezo driven mirror. The drawback of the galvanometer scanners is that the scanning axes are not fixed to a common pivot thus alignment between the two pairs is required. Moreover they exhibit a reduced life time when compared with the piezo driven tip/tilt mirror (billions of cycles are possible for piezo driven mirrors).

Possible scanning routines of the input beam to the bundle should be further investigated as well.

Fibre bundle end coating: Optical coatings can also be applied to the reference reflecting surface to control the magnitude of the reflection in order to produce the desirable ratio between reference and sample signal. Such a coating could be titanium dioxide.

Swept source: Accommodation of a frequency scanning light source (i.e. Swept Source) into the already described system could firstly lead to the elimination of the depth scanning mechanism. Secondly it will offer increased depth scanning speed performance and superior axial resolution. With this source the information from each wavelength will be separated in time, by rapidly sweeping narrowband light from a laser across a broad spectral range. The spectral components will not be encoded by spatial separation, but they will be encoded in time. The spectrum will either be filtered or generated in single successive frequency steps and reconstructed before Fourier-transformation. One more advantage offered by the incorporation of such a source is the proven high SNR as described in the instrumentation review chapter. The drawbacks that could be faced are the nonlinearities in the wavelength, especially at high scanning frequencies and the broadening of the linewidth at high frequencies.

Miniaturisation: Further investigations are required to obtain its true potential in endoscopic surgery. Such investigations should be targeted at miniaturising the components (e.g lenses at probe tip) in order to construct a compact robust and clinically safe endoscope.

General: Another approach to the configuration described would be to place a glass window or microscope cover slip on top of the sample to provide the reference reflection. If the glass window or microscope cover slip is positioned to be in contact with the sample this could lead to an additional advantage of the system. This is true as any motions of the sample could be partially compensated because the phase fluctuation caused by motions of the sample will be cancelled by the common motion of the reference surface. The cover slip can only be used for bench ex-vivo experiments but the glass window can also be used in an in-vivo operation.

References

1. Huang D, Swanson E. A., Lin C. P., Schuman J. S, Stinson W. G., Chang W., Hee W. Drexler, U. Morgner, F. X. Kärtner, C. Pitris, S. A. Boppart, X. D. Li, E. P. Ippen, and J. G. Fujimoto. *In vivo ultrahigh-resolution optical coherence tomography*, Optics Letters, Vol. 24, Issue 17, pp1221-1223

2. W. Drexler, U. Morgner, R.K. Ghanta, F.X. Kaertner, J.S. Schuman, J.G. Fujimoto, *Ultrahigh resolution ophthalmic optical coherence tomography*, Nature Medicine, Vol. 7, 2001, pp502-507.

3. M. R., Flotte T., Gregory K., Pualifito C. A., Fujimoto J. G, *Optical coherence tomography,* Science, Vol. 254, 1991, pp1178-1181

4. B. W. Colston Jr., M. J. Everett, L. B. Da Silva, *Imaging of hard and soft tissue structure in the oral cavity by optical coherence tomography*, Applied Optics, Vol 37, 1998, pp3582-3585

5. B. Povazay, K. Bizheva, A. Unterhuber, B. Hermann, H. Sattmann, A.F. Fercher, W. Drexler, A. Apolonski, W.J. Wadsworth, J.C. Knight, P.S.J. Russell, M. Vetterlein,E. Scherzer, *Submicrometer axial resolution optical coherence tomography,* Optics Letters, Vol. 27, 2002, pp1800-1802

6. A. Unterhuber, B. Povazay, B. Hermann, H. Sattmann, W. Drexler, V. Yakovlev, G. Tempea, C. Schubert, E.M. Anger, P.K. Ahnelt, M. Stur, J.E. Morgan, A. Cowey, G. Jung, T. Le, and A. Stingl, *Compact, low-cost Ti:Al_2O_3 laser for in vivo ultrahigh-resolution optical coherence tomography*, Optics Letters, Vol. 28, 2003,pp 905-907.

7. J. Su, J. Zhang, L.Yu , G. Colt, M. Brenner, Z. Chen, *Real-time swept source optical coherence tomography imaging of the human airway using a microelectromechanical system endoscope and digital signal processor*, Journal of Biomedical Optics, 2008.

8. J.G. Fujimoto, C. Pitris, S.A. Boppart, and M.E. Brezinski, *Optical coherence tomography: an emerging technology for biomedical imaging and optical biopsy*, Neoplasia, Vol. 2, 2000, pp. 9-25 .

9. P.R. Pfau, M.V. Sivak, A. Chak, M. Kinnard, R.C.K. Wong, G.A. Isenberg, J.A. Izatt, A. Rollins, and V. Westphal, *Criteria for the diagnosis of dysplasia by endoscopic optical coherence tomography*, Gastrointest. Endosc. Vol.58, Issue 2, 1993, pp 196-202.

10. M. Brezinski, G. Tearney, B. Bouma, J. Izatt, M. Hee, E. Swanson, J. Southern, and J. Fujimoto, *Optical coherence tomography for optical biopsy: properties and demonstration of vascular pathology*, Circulation 93, 1996, pp.1206-13 .

11. Rallan D., Harland C. C., Blackwell Publishing Ltd, *Clinical and Experimental Dermatology*,Vol.29,2004,pp453–459.

Appendix A

LABVIEW™ PROGRAM

The operation of program developed was outlined in chapter 6. Figure A.1 illustrates a general flow chart. Figure A.2 depicts the graphical user interface and figure A.3 part of low level program.

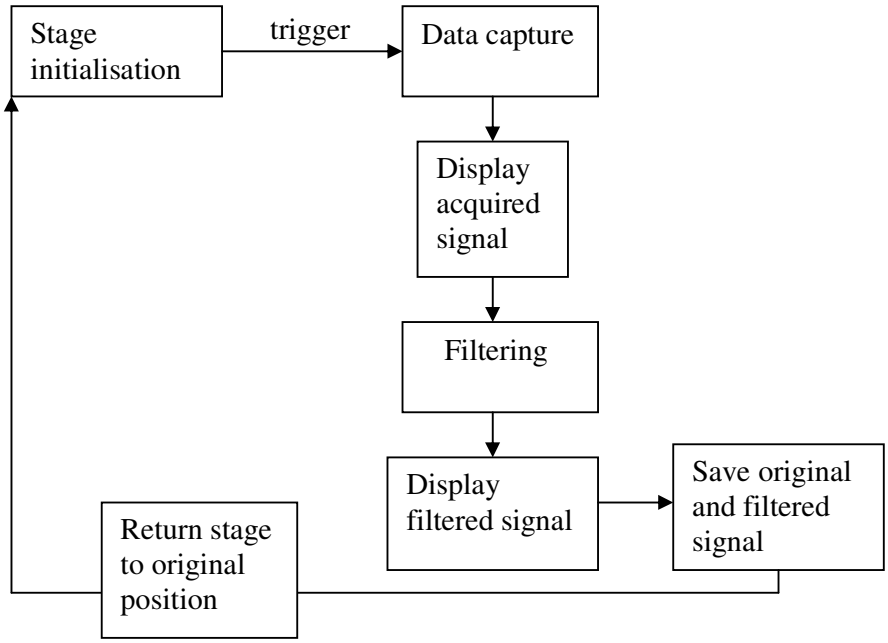

Figure A. 1: General flow chart of LabView ™ program developed

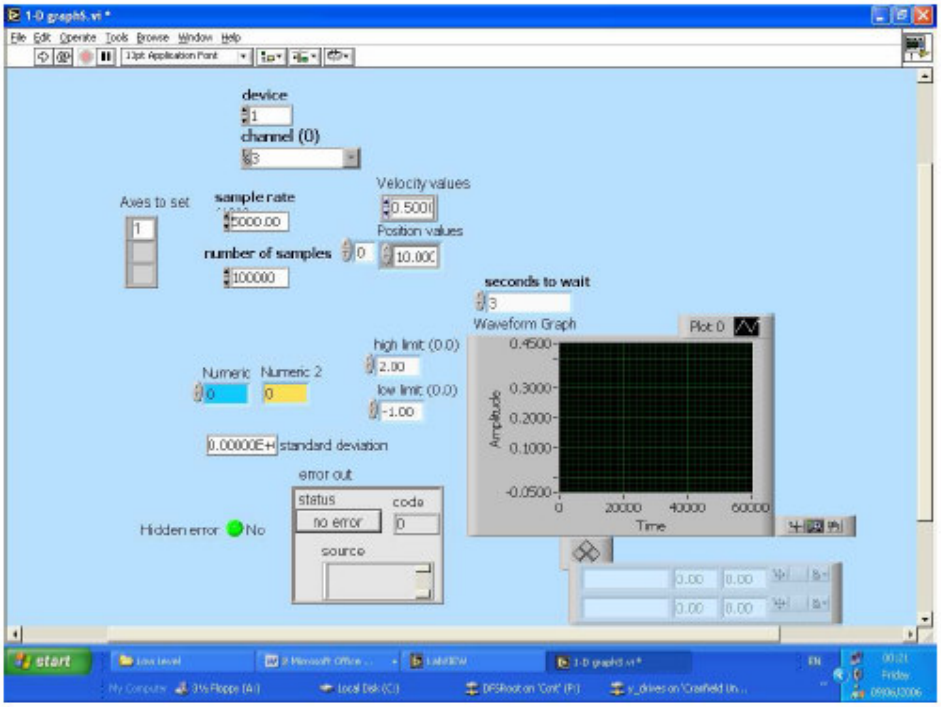

Figure A. 2: Graphical user interface

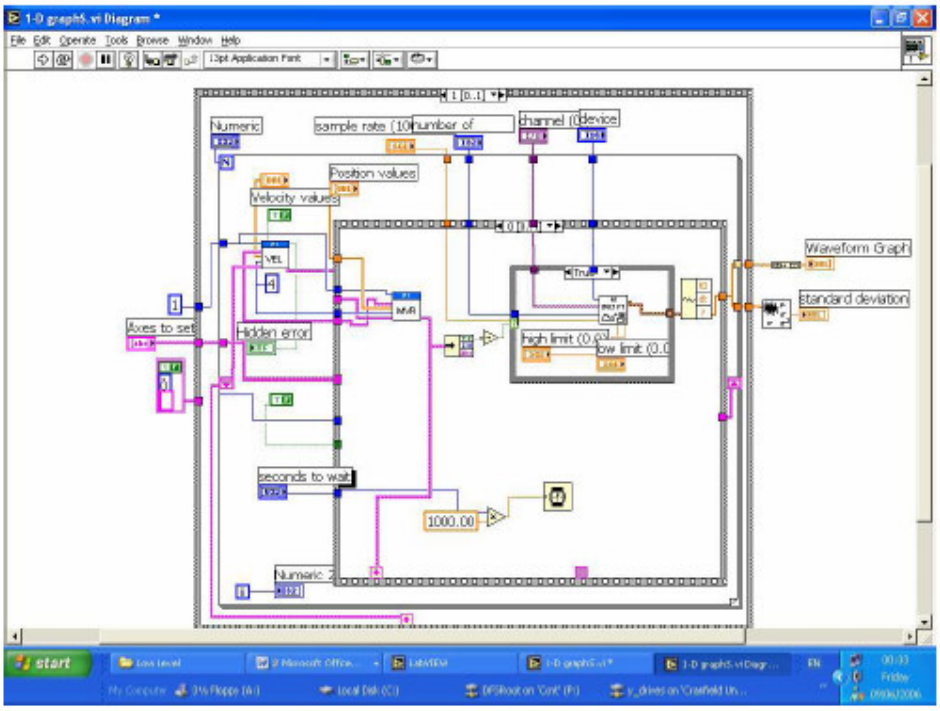

Figure A. 3: Low level LabView™ programming window

Appendix B

LIST OF APPARATUS DATASHEETS

- **Optical Sources [10/06/2008]:**

1. http://www.covega.com/Products/pdfs/SLD%201005%20Rev%20C.pdf
2. http://www.superlumdiodes.com/pdf/d830hp.pdf

- **Micro-positioning Translation stages[10/06/2008]:**

1. http://www.physikinstrumente.com/en/pdf/M110_Datasheet.pdf (motorised stage)
2. http://www.thorlabs.com/NewGroupPage9.cfm?ObjectGroup_ID=1041 (manual stage)
3. http://www.physikinstrumente.com/en/pdf/C843_Datasheet.pdf (stage controller, PCI card)

- **Optics (lenses, beamsplitters, collimators) [10/06/2008]:**

1. http://www.thorlabs.com/NewGroupPage11.cfm?ObjectGroup_ID=2126 (lenses)
2. http://www.thorlabs.com/NewGroupPage9.cfm?ObjectGroup_ID=139 (mirrors)
3. http://www.thorlabs.com/NewGroupPage9.cfm?ObjectGroup_ID=915(cube beamsplitters)
4. http://www.thorlabs.com/NewGroupPage9.cfm?ObjectGroup_ID=754(plate beamsplitters)
5. http://www.ozoptics.com/ALLNEW_PDF/DTS0060.pdf (collimator) [10/06/2008]

- **Data Acquisition Card [10/06/2008]:**

1. http://www.ni.com/pdf/products/us/20044546301101dlr.pdf

- **Detectors [10/06/2008]:**

1. http://jp.hamamatsu.com/resources/products/ssd/pdf/g837081_etc_kird1064e04.pdf

Appendix C

PUBLICATIONS & CONFERENCE PRESENTATIONS

1. Sarantavgas G., Ford H. D., Tatam R. P., Imaging fibre bundles for Fizeau based OCT. (Clinical technologies and systems, Coherence domain optical methods and optical coherence tomography in biomedicine, Catheter/Endoscopic OCT), *Photonics West, BiOS '08*, Published in conference proceedings of the SPIE, Volume 6847, pp. 68470C-68470C-11, San Jose, California, USA, 2008.(peer-reviewed)

2. Sarantavgas G., Ford H. D., Tatam R. P., Fizeau-based OCT using coherent fibre imaging bundles, Cranfield Multistrand Conference, *CMC 2008*, Cranfield, UK, 2008.

3. Ford H. D., Sarantavgas G., Tatam R. P., Full Field OCT using imaging fibre bundles. *International Workshop on Digital Holographic Reconstruction and Optical Tomography for Engineering Applications.* Published in conference proceedings, Loughborough, UK, 2007. (peer-reviewed)

4. Sarantavgas G., Ford H. D., Tatam R. P., Fibre imaging bundles for Fizeau-based optical coherence tomography, (Advanced imaging and microscopy), *Photonex '07*, Coventry, UK, 2007.

5. Sarantavgas G., Ford H. D., Tatam R. P., Fizeau-based optical coherence tomography using a fibre imaging bundle. (Photonics and imaging in biology and medicine), *Photon '06*, Manchester, UK, 2006.

6. Sarantavgas G., Ford H. D., Tatam R. P., Investigation of fibre imaging bundles for Fizeau-based optical coherence tomography, **to be Submitted**, *Journal of Measurement Science and Technology*.

Cross-referenced:

This research was also referenced in patent: *USPTO 20080007733*–Volumetric endoscopic coherence microscopy using a coherent fibre bundle.

Funding:

In April 2008 this research has received an additional funding from EPSRC for further development.

http://gow.epsrc.ac.uk/ViewGrant.aspx?GrantRef=EP/F034679/1 [10/07/2008]